



Aalborg University

Chemical Engineering Department

Project:

“Geopolymer synthesis and characterization using Raman spectroscopy, FT-IR, DSC, XRD and compressive strength test”

Supervisor:

Erik Gydesen Søgaard

Students:

Guillermo Chaquina

Kristóf Gazda

Group number:

K10k-1-F15

Esbjerg, Denmark, 09 of June 2016

0. Abstract

A feasibility study on using different techniques (Raman spectroscopy, FT-IR, DSC, XRD and compressive strength test) in order to characterize geopolymers has been done to understand how to better employ fly ash as a supplementary material in the production of concrete. Fly ash, Class F, was polymerized using potassium hydroxide as an activator and potassium silicate solution; the samples were done with a KOH concentration of 4 M and 6M, and changing the liquid and solids ratio between 0,4; 0,5; 0,6 and 0,7. Preprocessing was used on the raw spectra obtained using Raman spectroscopy. IR spectroscopy was used as a complementary technique for Raman spectroscopy. The DSC analysis was performed using nitrogen atmosphere, with a heating rate of 20 °C/min between 25 °C and 550 °C. The phases of geopolymer and cement materials were studied with XRD. Compressive strength was done on 25 mm diameter and 50 mm height samples using the instructions of ASTM C39/C39M.

Table of Contents

0. Abstract.....	2
Introduction.....	5
1. Literature overview	7
1.1. State the problem: “why fly ash as a complement for cement and why to characterize it?”	7
1.2. Why is it important	7
1.2.1. Global coal production and consumption	9
1.2.2. Coal combustion power plants.....	10
1.2.3. Global fly ash trends	11
1.2.4. Fly ash utilization.....	11
2. Geopolymerization and fly ash	13
2.1. Geopolymers and their properties	13
2.2. Geopolymerization stages	13
a. Destruction and coagulation:	14
b. Coagulation and condensation:	14
c. Condensation and crystallization:	15
2.3. Geopolymers applications.....	16
2.4. Fly ash.....	17
2.5. Alkali activator and silicate.....	19
3. Raman spectroscopy and IR.....	21
3.1. Raman and IR background.....	21
3.2. Smoothing:.....	24
3.2.1. Normalization:	25
3.2.2. Mean centering:.....	26
3.2.3. SNV or Baseline correction:	27
3.3. Literature review for Raman	27
3.4. Literature review for IR	30
3.5. Experiments and results	35
3.5.1. Raman spectroscopy	35
3.5.2. FT-IR.....	47
4. DSC.....	54
4.1. DSC theory.....	54
4.2. What has been done	58
4.3. Results and analysis	62
5. XRD.....	67

5.1.	Theoretical background.....	67
5.2.	Literature review	70
5.3.	Experiments and results	73
6.	Compressive strength.....	78
6.1.	Theoretical background.....	78
6.2.	What has been done before	79
6.3.	Experiments and analysis.....	80
7.	Conclusions	85
8.	Recommendations.....	86
9.	Bibliography	87
10.	Appendix.....	91
	MATLAB codes.....	98
1.	Transform the SPC files into matrixes:.....	98
2.	Preprocessing Savgol method:	99
3.	Preprocessing alsbasecorr method:	100
4.	Generation of Raman spectra sample code:	101

Introduction

One of the most important phases during wells production is when it is time to abandon the well. This happens when the gas and oil extracted is not economically viable anymore to continue with the operation of the respective well. In order to make sure there is no leaking of oil into the surrounding environment, Portland cement is used but because of the rush doing this work and because it is not easily controlled, errors have arisen in the past that have cost millions of dollars to the oil industry in order to fix the mistakes.

The demand to look for more versatile materials that can also reduce the cost in the oil industry is ever increasing. Especially with the recent low oil prices after 2015, lower operation costs have a very high priority. One of the main candidates for the job is called Fly ash or bottom ash. This is a byproduct that comes from the combustion of coal in power plants and different companies like Esbjerg Power Station operated by DONG is a local source of fly ash.

Geopolymers are materials created with the mixture of three materials like the fly ash with an activator (KOH or NaOH) and a solution of silicate in order to create a gel that will harden following a similar reaction as Portland cement. One of the main differences between Portland cement and fly ash is the first one already has a high concentration of aluminum-silicate and its own natural activators, so it is generally just mixed with water. On the other hand, fly ash needs the presence of the activator in order to initiate the polymerization.

Raman spectroscopy and infrared are two of the top most used analysis to obtain spectra that will have bands indicating the fingerprint of diverse types of materials. The main differences between them is that Raman does not require the destruction of the sample before measuring and the second is the sampling can be done in situ, meaning it does not require a laboratory environment like in the case of the IR.

Curing refers to the stage of the polymerization between the initial mixing and certain amount of time later when new bonding have been created in the material and it has acquired the new desired characteristics, like hardness for example. One way to monitor the curing is using spectroscopy, which measures the bands shift when new bonds are disappearing or forming during the polymerization.

In general, it is important to try to have an understanding of material and a correct characterization of the fly ash is necessary in order to work properly with it. There are two big classes of fly ash, which have different chemical composition and their behavior can be completely different. Some experiments that are recommended to study the properties of the fly ash are Raman and FT-IR for spectroscopy, DSC, XRD for the composition of the materials and compressive strength for mechanical properties.

The main objective for the thesis was to study the possibility of using the fly ash as an alternative or at least a supplementary material for creating cementing components that could be employed for plug and abandonment operations in the oil and gas industry. Raman spectroscopy and molecular simulation were also employed in order to try to find a correlation between the degree of cure and the spectra obtained using this technique, as previously tried in other works.

To reach the objectives a set of tasks were preselected and are shown next:

- Obtain knowledge regarding the regular cementing techniques used for the regular material, Portland cement.
- Investigate what has been done so far regarding the fly ash and how the different techniques explain its behavior like Raman spectroscopy and FT-IR.
- Develop an understanding of fly ash and modify the regular procedure for the mixture to include it as a substitute or supplement.
- Carry out experiments and simulations regarding the fly ash. Analysis using some of the theory earned in previous projects and comparison of results were done afterwards.

This thesis project is organized in 7 chapters. Chapter 1 for “Literature Overview” gives a short explanation of the current use and importance of Portland cement around the world and in Denmark, as well as an introduction to the fly ash as the focus of study and its general properties that makes it a good material for cementing processes. The main objective and the different sub-objectives followed during the development of the study are in this chapter.

Chapter 2 focuses on the chemistry behind the Geopolymers, the fly ash, the importance of the activators like sodium and potassium hydroxide, the use of water glass or silicate solution, the different phases that appear during the curing process and the Geopolymers properties.

Chapter 3 is the spectroscopy section and it summarizes the theory behind Raman and FT-IR, the latest literature that was studied and its used with the analysis of the experiments results that were obtained.

From Chapter 4 to 6, a similar order was followed as the spectroscopy section: the theory, literature and analysis of the experiments done using DSC, XRD and compressive strength were included, each type of experiment in one chapter.

Finally, Chapter 7 and Chapter 8 includes the conclusions for all the experiments performed, as well as recommendations for future studies later, like improvements or new approaches to take.

1. Literature overview

1.1.State the problem: “why fly ash as a complement for cement and why to characterize it?”

Cement is used as the main material for different operations like plug and abandonment of wells in the oil industry and geopolymers have shown to have similar mechanical properties, which mean they could be a good addition for the cementing process.

Fly ash has been used for many years already as a supplementary material for cement, however there is no clear consensus on the optimal mixing design to achieve the best properties for cement (both mechanically and chemically) because the reaction is too complex in order to properly study it in detail.

1.2. Why is it important

One of the main reasons for suggesting the use of fly ashes is that by 2010 the production of Portland cement contributed to around 5% of global CO₂ emissions, because the manufacturing of one ton of Portland cement releases one ton of CO₂ into the atmosphere [1]. Figure 1 shows the world production of cement by 2014 [2]:

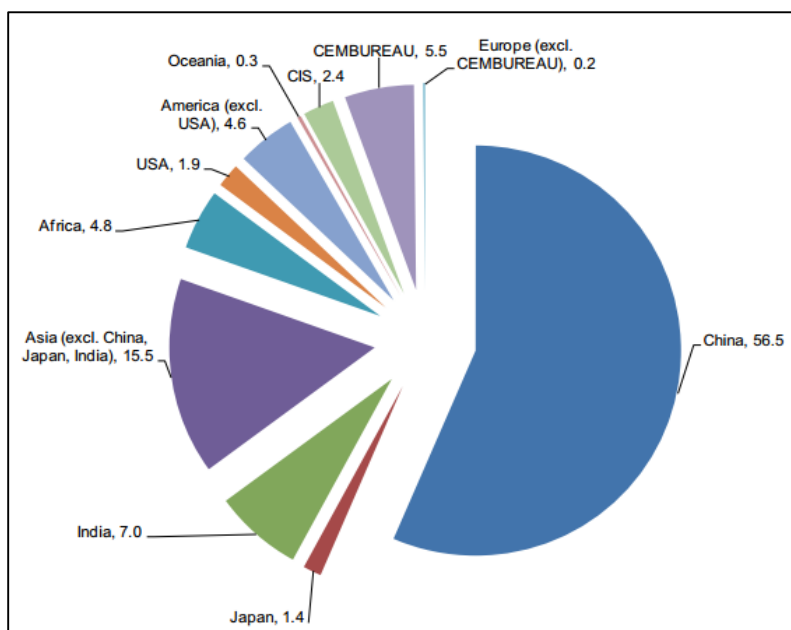


Figure 1. World production of cement by 2014, data done by CEMBUREAU [2]

All of these countries that produce cement - for either local use or exporting to other countries - could contribute to lowering global CO₂ emissions by switching to the use of geopolymers instead of Portland cement or use fly ash and Portland cement mixtures. This would mean that the CO₂ emissions could be halted or substantially decreased from these types of sources.

On Figure 2, the production of cement (in million tons) in Europe can be seen decreasing over the years and Figure 3 shows that the consumption has increased in Denmark, as well as most of the European countries. This means there is a chance that in order to get the cement needed Denmark will have to import it internationally and that can carry more cost.

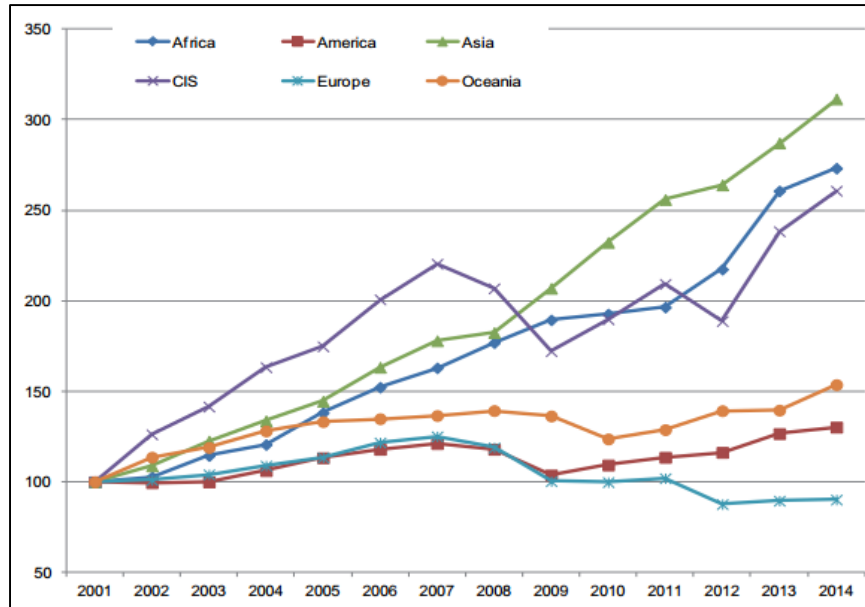


Figure 2. Cement production rate by region until 2014 [2]

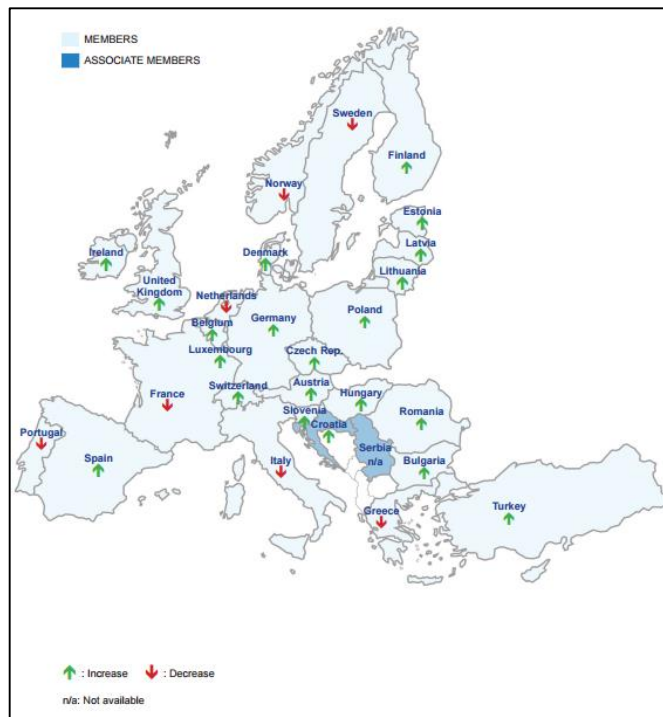


Figure 3. Consumption of cement in Europe between 2013 and 2014 [2].

1.2.1. Global coal production and consumption

Humanity has been using coal as a source of energy since prehistoric times. It should not come as a surprise that even today, a substantial amount of electricity and heat generated comes from the burning of coal at power plants. Recent data from British Petroleum's Statistical Review on World Energy [3] shows that the use of coal today is far from vanishing. Figure 4 visualizes World coal production and consumption from 1989 to 2014. It can be seen that the Asia Pacific region (containing India and China) had a big boom of coal in the early 2000's and have effectively doubled their coal mining and usage since then. Regarding Europe coal usage has been steadily decreasing since 2008 and the EU-s plan is to decrease the member states' fossil fuel dependence by a substantial amount by 2020. In particular, Denmark has vowed to fully convert the country's energy usage (electricity, heating, industry and transport) to be supplied by renewable sources by 2050 [4].

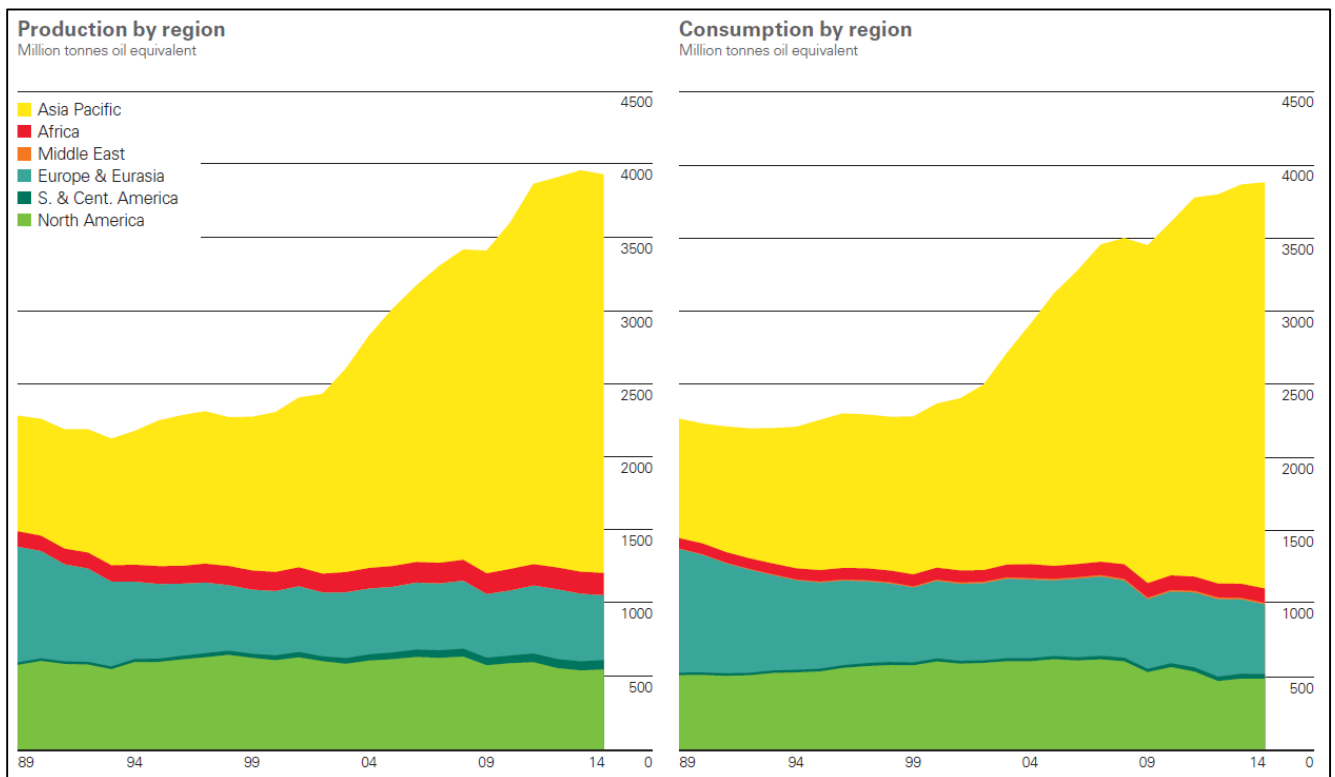


Figure 4. Global coal production and consumption by region [3]

1.2.2. Coal combustion power plants

The coal arrives to the power plant by various modes of transportation that are available to the power plant (by river barges or freight trains). The arriving coal is usually in lumps, so the first step in the process is to transport it to steel mills where the large clumps are pulverized into very fine particulate matter. This is advantageous because the surface area and thus the efficiency the coal will burn with increases considerably. After milling the powdered coal is blown into the combustion chamber (or furnace). The burning releases a lot of heat and creates high temperatures inside the furnace (as high as 2000 °C). This heat is transferred to the incoming cool water inside the coils located in the furnace, which flows to the boiler and generates high pressure steam. This steam is taken to the steam-turbine where its mechanical energy is transferred to the generator which produces the electricity. The generated electricity is then transferred to the grid through a transformer and it's on its way for public use. The steam is condensed, cooled further and recirculated back to the boiler, forming a closed loop. Figure 5 shows a rough schematic of a coal fired power plant.

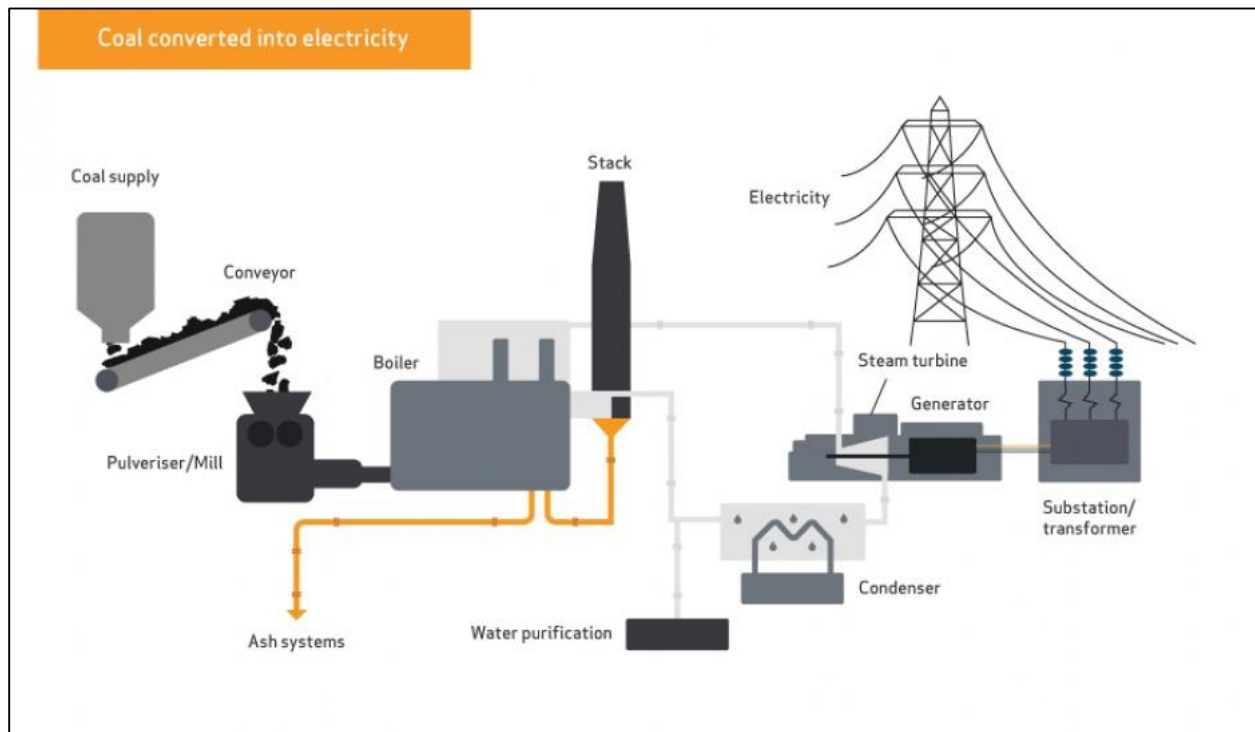


Figure 5. Schematic of coal fired power plant [5]

1.2.3. Global fly ash trends

As we have seen, fly ash is a byproduct of the combustion process in coal-fired power plants. Due to the varying nature of the source material and depending upon the combustion process, it is safe to say that fly ash is one of the most abundant and complex materials that originate from anthropogenic sources [6].

What is referred to as fly ash is usually generated in two forms, coarse bottom ash and fine fly ash. The former represents 5-15wt.%, while the latter can be 85-95 wt.% from the total amount of bottom ash generated.

1.2.4. Fly ash utilization

Because fly ash is a combustion products, usually is treated as a waste, but recently its use has been included in different markets like the ones listed next [7]:

- Concrete productions

This is the main point of interest and is discussed in detail in later chapters.

- Waste stabilization

Big amounts of dangerous metals like Pb, Cd, Cr and Zn are present in different processes like electric arc furnaces, but stabilization techniques have been develop in order to reuse this materials and one of this technologies is for the production of Geopolymers. This type of polymers have been found to possess similar encapsulation properties like cement and that is why they are a good option to stabilize these wastes [8].

- Mine reclamation

Coal mines reach a point where they need to be abandoned because the materials that can be extracted have already been exhausted or because the cost in maintaining them is too big. However, fly ash dumps are one of the products that is present this type of mines has been estimated a waste of over 2 million acres. This represents a big amount of products that can be reuse and that is the reason for some mines to start again [9].

- Aggregate substitute for construction materials

Fly ash has been crushed and added to concrete samples, making the final products over 20% lighter and 20% stronger when compared to the original materials, it shrinks less once it is dry and it possess a high durability. Studies have found tops a decrease of 20% in cement used for creating brick maintaining the required compressive strength resistance [10].

- Soil amelioration

Dolomite is often used to bring down the pH of acidic soils, however dolomite is not environmentally friendly. Coal fly ash however would be great in this regard. According to Yao et al. [6] “the physicochemical properties of coal fly ash including silt and clay-sized particles, lowbulk density, higherwater-holding capacity, favorable pH, and source of essential plant nutrients, etc.,make it a potential amendment for soils”.

Several other uses are known for fly ash, a summarizing figure can be seen in Figure 6.

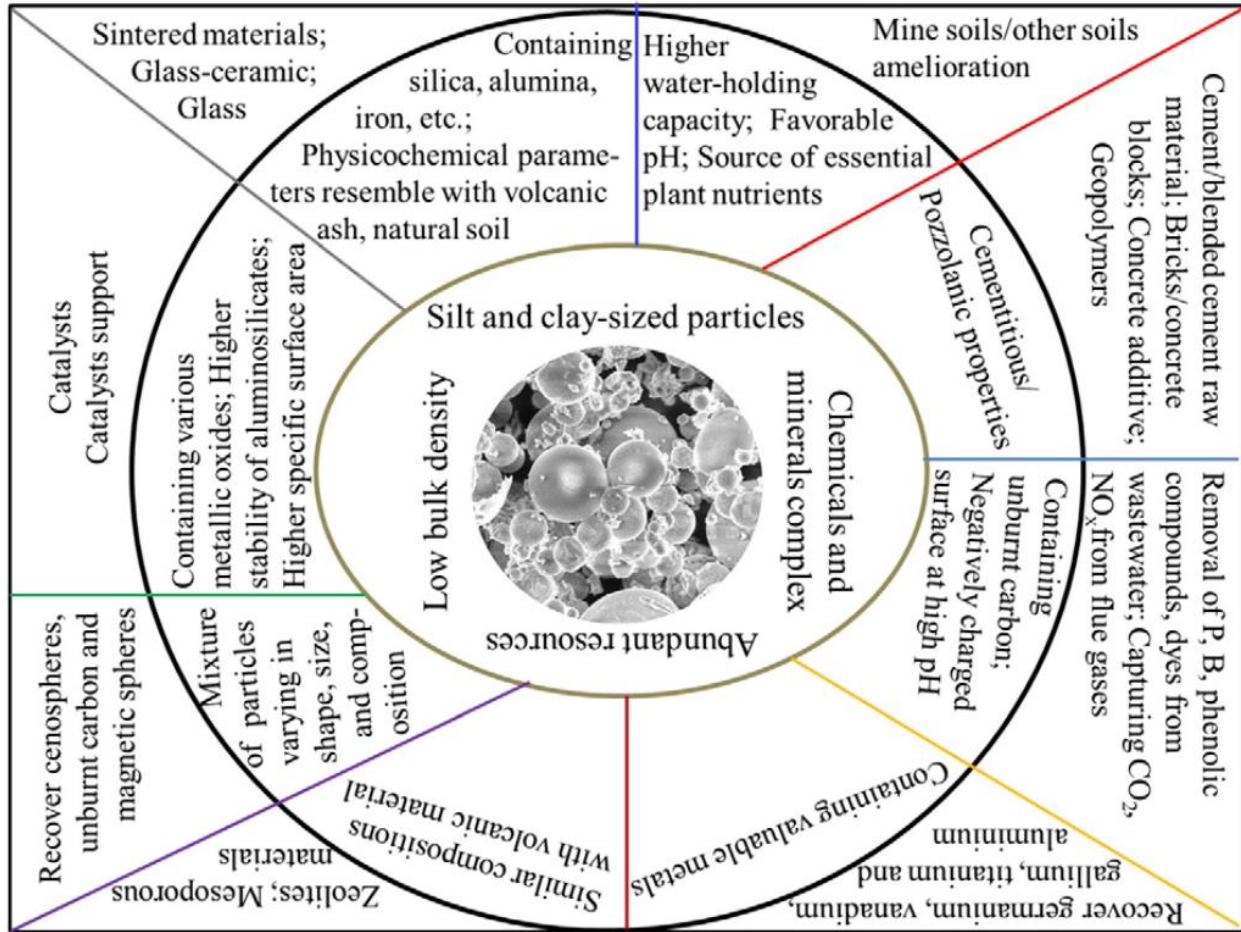


Figure 6. Various applications of fly ash [6]

2. Geopolymerization and fly ash

2.1. Geopolymers and their properties

Geopolymers are solid aluminosilicates that are synthesized using an activator (generally alkali hydroxide or alkali silicate) and a binder or precursor that is usually in solid state [11].

2.2. Geopolymerization stages

The main characteristic that defines the chemical and physical properties of cements and similar materials are defined by the C-S-H gel or hydrated calcium silicate gel, which is the main product of the hydration of Portland Cement [12].

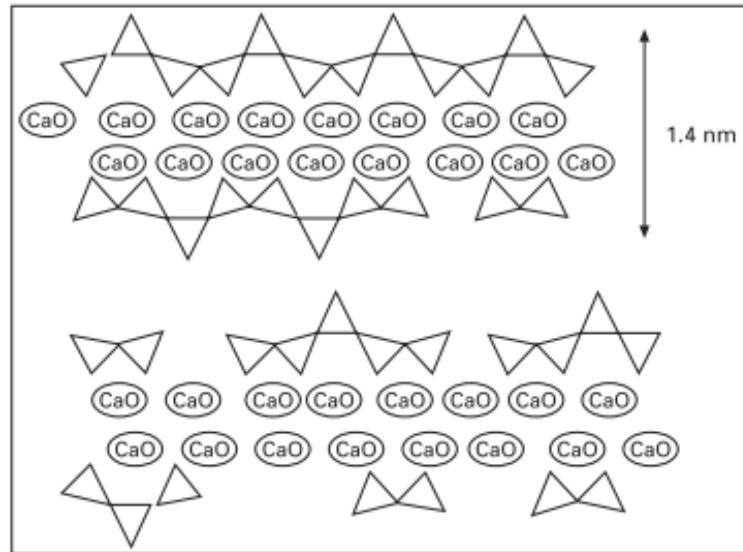


Figure 7. Theoretical structure of the calcium silicate gel.

The theorized process for silica acid polymerization focuses on three parts, like a regular polymerization[13]:

- Polymerization of the monomer and the formation of the particles.
- Growth of the particle or extension of the monomer.
- Bonding on the particle forming chains, networks and the expected gel.

Summarizing the basis of this polymerization is that the monomers of the silica acids or $\text{Si}(\text{OH})_4$ will create dimers, cyclical molecules and larger molecules containing siloxane bridges, Si-O-Si, and the final product will depend on the pH of the solution [13].

If the pH of the solution is below 7 or if it is between 7 and 10 in the presence of salts, the molecules will aggregate and create particles [11]. However, if there are no salts present when the pH is between 7 and 10, the particles will grow in size and their number will be decreasing until

they form a sol gel. Since the salts are not present they cannot act as flocculation agents at higher pH [13].

Experiments have shown an “increase in the molecular weight of the silica which is part of the condensation of silanol”[11] as shown in Figure 8:

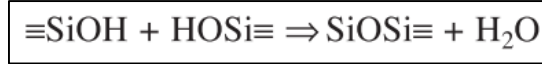


Figure 8. Condensation of silanol groups [11].

a. Destruction and coagulation:

In the first step the bonds between Me-O, Si-O-Si, Al-O-Al and Al-O-Si are broken, and the rupture is started by the OH⁻ ions that can be seen represented in Figure 9:

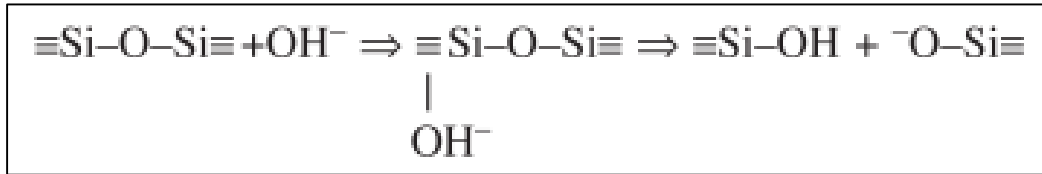


Figure 9. Rupture of the Si-O-Si bonds

b. Coagulation and condensation:

After the molecules are dispersed, accumulation will be promoted and they will form coagulated structures where poly-condensation will occur. This condensation of silica acid will increase at high pH values as explained before and hydroxylated complex will form Si(OH)₄, which will lead to the formation of new Si-O-Si bonds and form dimers [11]:

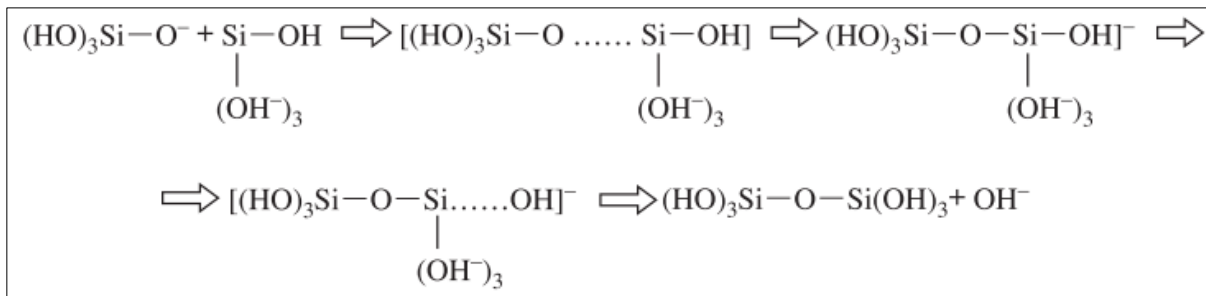


Figure 10. Formation of new Si-O-Si bonds[11]

The main difference from the previous stage is that in the first one the alkaline metal will generate the destruction but on the second and last stage it is a structural component. During the second stage aluminate will be substituted for silicate tetrahedral [13].

c. Condensation and crystallization:

Once the oligomers are formed, they will form crystalline structures or they will create amorphous polymers that will also undergo crystallization and create the same crystalline structures [14]. The general process for making geopolymers is resumed on Figure 11, and it is important to note that even though the represented process looks linear, these reactions are occurring at the same time [11]:

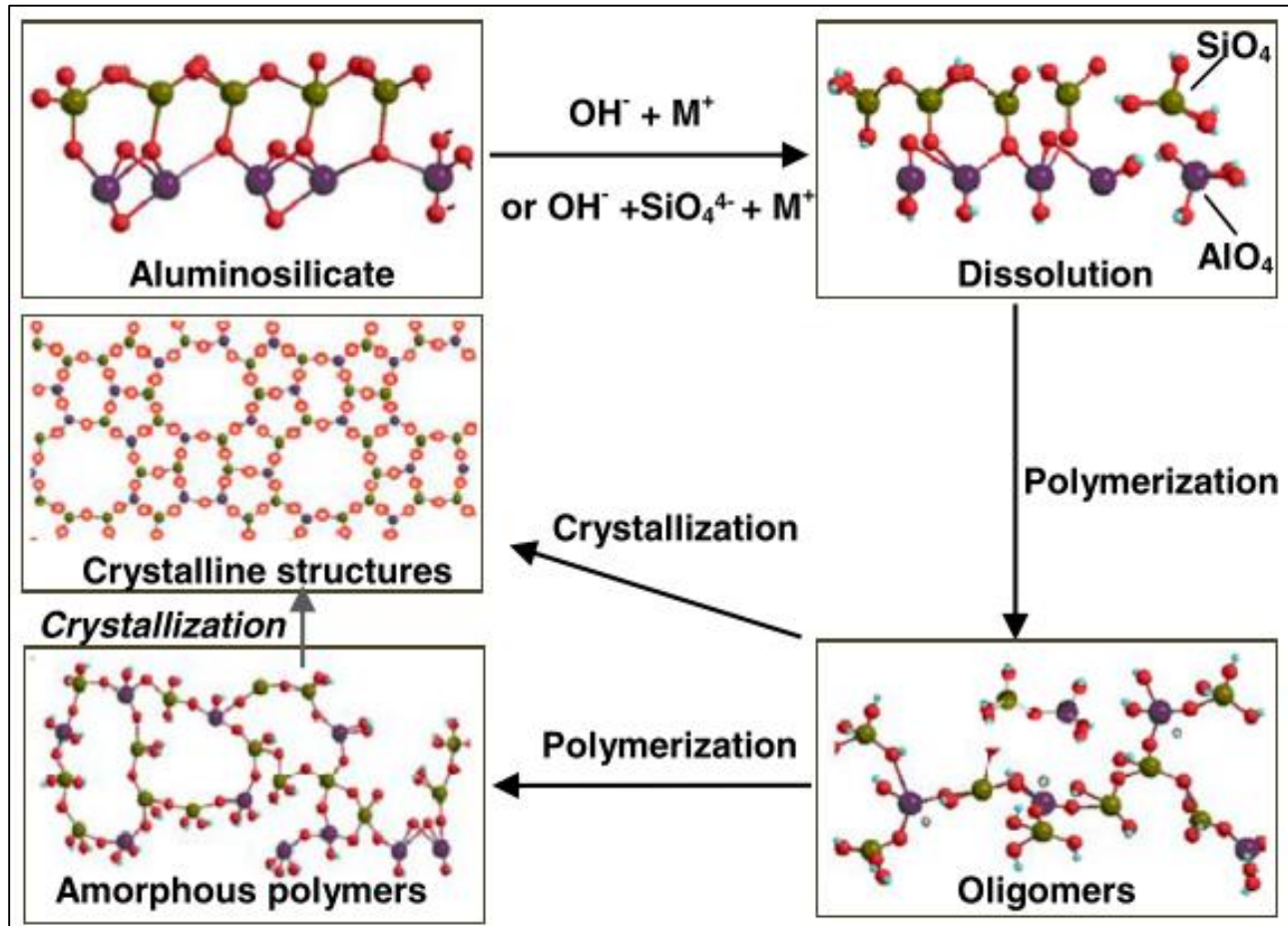


Figure 11. Geopolymer synthesis process [14]

The mechanism showed is simple, only showing how the material is transformed from a solid aluminosilicate material into a synthetic alkali aluminosilicate. After the gel is formed, the system will continue to rearrange and the number of connections between the molecules will also increase creating the 3 dimensional network that is associated with geopolymers [15].

2.3. Geopolymers applications

As explained before, the fly ash could be used as a substitute or complement products during cementing operations in plug and abandonment in oil industries, however it also has many other applications, some of them were mentioned by [16] and they are shown in the next table.

Table 1. The use of geopolymers with different Si:Al ratios

Si:Al ratio	Applications
1	Manufacture of bricks Manufacture of ceramics Can be used in the fire protection field
2	Concretes and cements that have a lower Encapsulation that can be used for radioactive materials and toxic wastes.
3	Fire glass composites that can be used for fire protection Equipment used for foundry Creation of material with heat resistance between 200 and 1000 degrees Celsius. Use in aeronautical process that employ titanium.
More than 3	Sealants materials from 200 to 600 degrees Celsius Materials for SPF aluminum in the aeronautic field.
Between 20 and 35	Create fiber materials that are fire and heat resistant.

It can also be found in the literature, that low calcium fly ash geopolymers have strength properties similar to Portland cement and in some of the tests it even showed even better performance [16].

2.4. Fly ash

This material comes from the remnants after the furnace of coals in combustions, which are divided into clays, sand and other organic material. Fly ash composition can vary by large margins because there is no guarantee of the amount of impurities in the coal before it is combusted and also because both the quenching and the combustion processes [11].

The most used fly ash is known as Class F and they are low in calcium, as defined by the standard ASTM C618, while the fly ash higher in calcium content is known as Class C. These are not widespread in cementing applications because the setting time is very low, so the hardening of the cement will happen quite fast, in a matter of minutes in extreme cases[11]. A visual difference in color can be observed on Figure 12 from the two types of fly ashes:

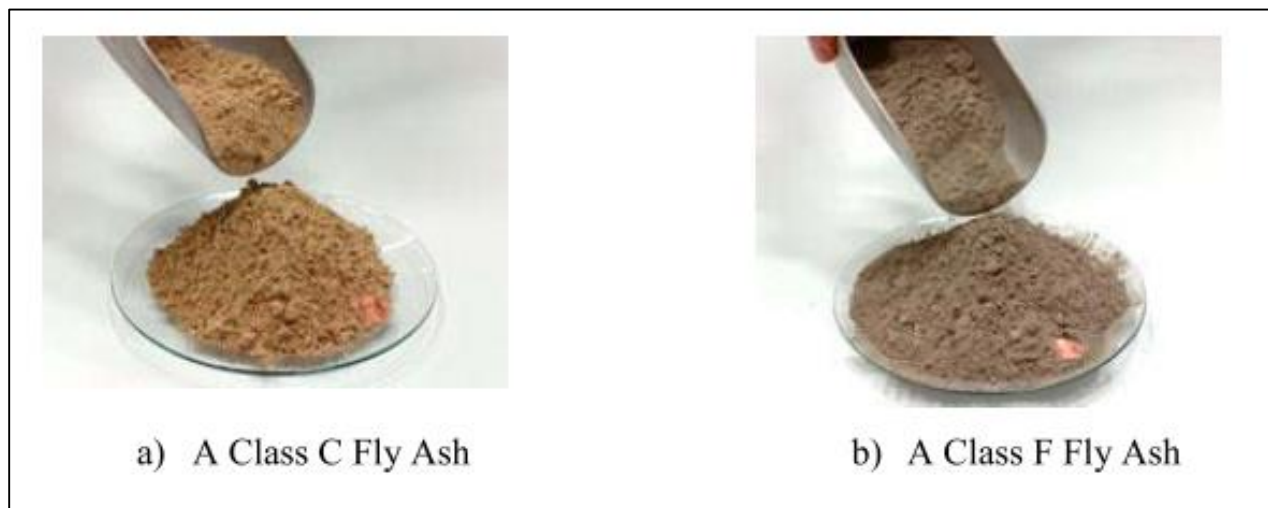


Figure 12. Samples of fly ash Class C and Class F [1]

Figure 13 shows different types of fly ash according to the composition of the oxides. were tested for compressive strength after doing alkaline activation on them, but because the data were taken from different sources the results are separated not by numbers but with levels: low, medium and high [11].

ASTM C618 which is titled “Standard Specification for Coal Fly Ash and Raw or Calcined Natural Pozzolan for Use as Mineral Admixture in Portland Cement Concrete” [17], defines that Class F fly ash has pozzolanic properties and are derived from anthracite and bituminous coals. On the other hand Class C fly ash has both pozzolanic and cementous properties and they are derived from sub-bituminous and lignitic coals.

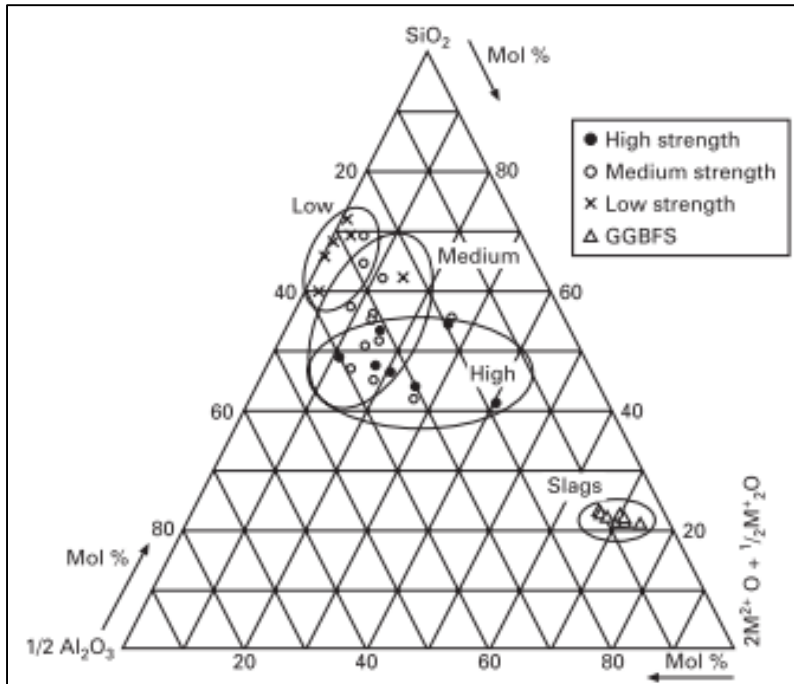


Figure 13. Ternary diagram for fly ashes and the strength of some types depending on the compositions [11]

From the figure it can be seen that the fly ashes with lower quantities of M^{2+}O and M^{+2}O (also known as network modifying cations) will produce the weakest products and strength will increase with the increase of those cations. On the figure, the white dots, the black dots (except the one more to the right) and the exes represent the Class F fly ash, the black dot that is more to the right below the word “High” is the Class C fly ash and the triangles are slag products. From the figure it can be extracted that increasing the amount of alumina will increase the strength the fly ash products and the fly ash with the biggest amount of SiO_2 has the lowest amount of alumina and are the weakest of all [11].

Because fly ash has been studied extensively, it has been concluded that the process for polymerization will depend on the source used for the fly ash and because of how their compositions can vary from batch to batch. In addition to this, fly ash is also affected by seasonal changes, as coal generators tend to be restricted to double shifting in summer months, increasing the LOI (loss on ignition). An increase in LOI and thus carbon content decreases the quality of the fly ash [6].

Another reason for preferring class C fly ash is that generally bigger amounts of it is needed in order to achieve similar results. According to ACI 318 the highest amount of fly ash content that can be used on concrete should be up to 25% of the cement part in order to prevent scaling when the concrete is in contact with deicing salts [17].

It is important to know that the class C fly ash is more available than class F because this last one is in such high demand, but class C fly ash properties had been less studied so in order to use this material, a complete study of it should be done before hand.

2.5. Alkali activator and silicate

The most important note would be to clarify that just adding alkali activator will not give a geopolymer [18], which is a common misconception that lot of authors like J. Provis and J. van Deventer have [11], which defines “In general, aluminosilicate binder materials activated by alkali hydroxides or silicates under high pH conditions are classified as being geopolymers”.

Figure 14 shows the dependence of the viscosity with the concentration of several alkali hydroxide activators: Lithium, sodium, potassium, rubidium and cesium hydroxide. The most used alkali solutions are sodium and potassium and it can be seen that the viscosity of NaOH change faster while the concentration increase, in comparison with KOH [11].

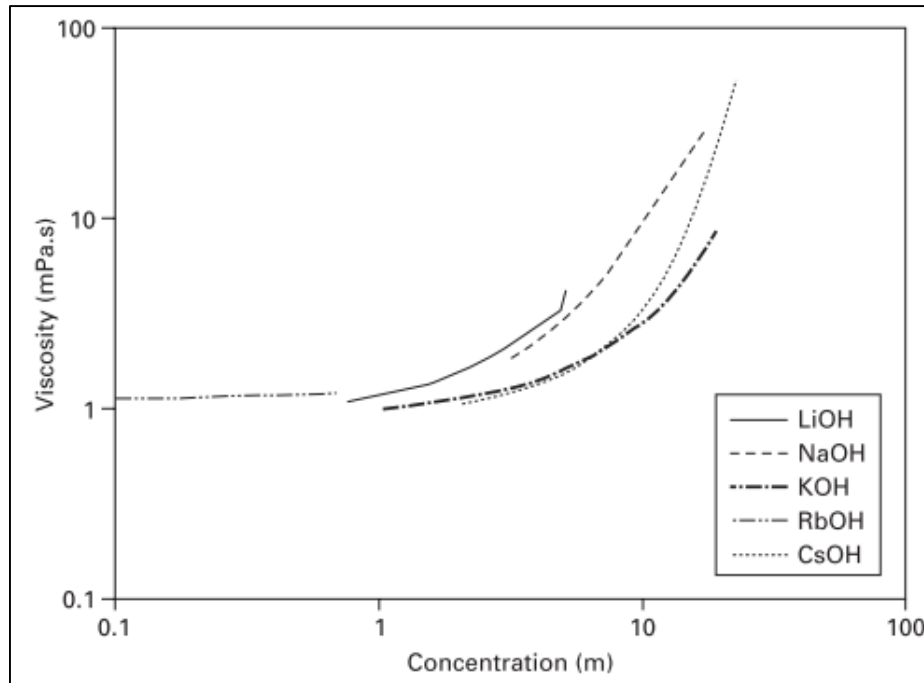


Figure 14. Viscosity of several hydroxide solutions for alkali activation [11]

One reason to choose the KOH as the activator would be in order to obtain a less viscous solution when the slurry is created when mixing with the fly ash; it is in our best interest to be able to pump easier the solution into the wells that need to be plugged and abandoned.

On Figure 15 the dissolution enthalpy for the same alkali activators from Figure 14 is shown and it can be seen that all of them are negative, which mean that they will dissolve exothermically, releasing energy [11].

One consideration before selecting the activator would be that the releasing of energy will affect the curing time of the fly ash: the more energy released, the faster the curing will proceed [11]. In this regard, the difference between the enthalpy of KOH (-60 kJ/mol) and NaOH (-40 kJ/mol) may not be so significant to affect the reaction.

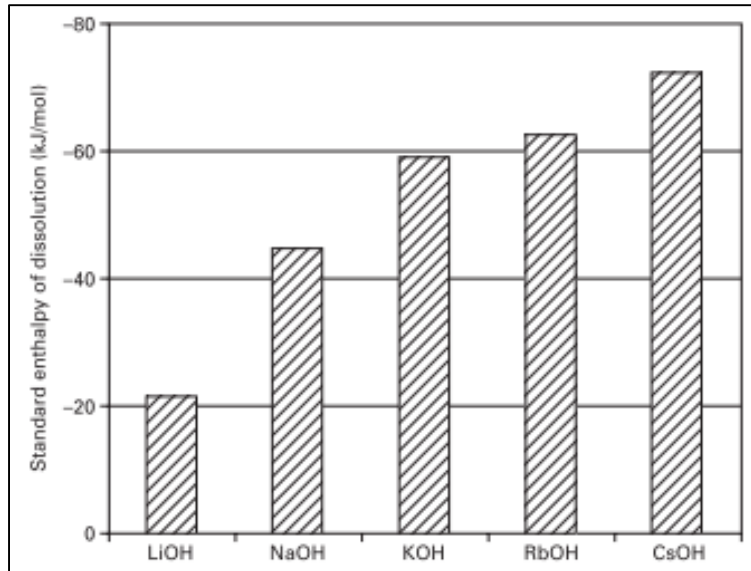


Figure 15. Enthalpies of dissolution of some metal alkali hydroxides [15]

Some studies had reveal that a combination of activators from the group alkali silicates and alkali hydroxides are ideal because during the mixing the soluble silicate and the hydroxides will make the rate of the reaction higher [16][19]. A reason for this behavior could be because the alkali hydroxides are used for dissolving Si, Al and other components in the mixture, which will make the process easier [20].

A higher degree of dissolution, meaning the ratio of hydroxide to the silicate, was observed when the fly ash was activated using sodium hydroxide when compared of potassium hydroxide. It has been observed also that the higher the concentration of hydroxide will give a harder fly ash products when applying the compressive strength test [16].

3. Raman spectroscopy and IR

3.1. Raman and IR background

In general spectroscopy is employed to measure the vibration in the molecules and the process are based either on infrared absorption or Raman scattering in order to determine different properties from materials like the physical or chemical structures. In general, all of this processes permit to measure properties unique to each material which is why is called “fingerprinting” or characteristic spectral patterns [21].

The relation between wavelength (λ), frequency (ν) and wavenumber (ω) are shown from equation 1 to equation 3:

$$\lambda = \frac{c}{\nu} \quad (1)$$

$$\nu = \frac{\Delta E}{h} \quad (2)$$

$$\omega = \frac{\nu}{c} = \frac{1}{\lambda} \quad (3)$$

From equations 1 to 3 it can be inferred that energy ΔE is proportional to the inverse of the wavelength, λ , which means that from Figure 16 the longest wavelength is on the left side and the lowest energy is on the right side.

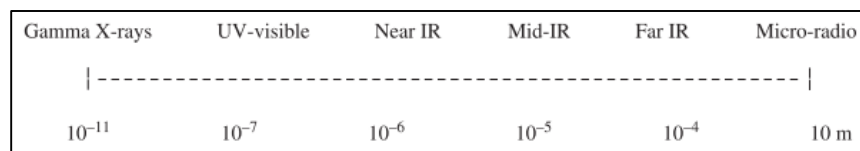


Figure 16. Electromagnetic spectrum [21]

Each of the techniques seen in the above picture are used in a specific range of the electromagnetic spectrum. All of the techniques have their pros and cons, however Raman spectroscopy was selected because it is a non-destructive method, meaning that it is not necessary to extract some material or break the main body of the sample. It is not necessary to make the measurement in laboratories with specialized equipment to get the results; and the sampling can be taken in situ which is a major advantage in field use.

Absorption process is generated when both the frequency of the inlet radiation and the vibration of the molecule are equalized, leaving the molecule in an excited state where the difference in frequency from the beam is measured and the values are reported [21]. On the other hand, with Raman the beam that is used has a single frequency, without matching the vibration of the molecule to the excited state, and after the beam hits the molecule what is measured is the inelastically scattered photons. These can be categorized as Stokes or anti-Stokes shifts of the incident photon, so in essence Raman spectroscopy measures the frequency shift of scattered photons.

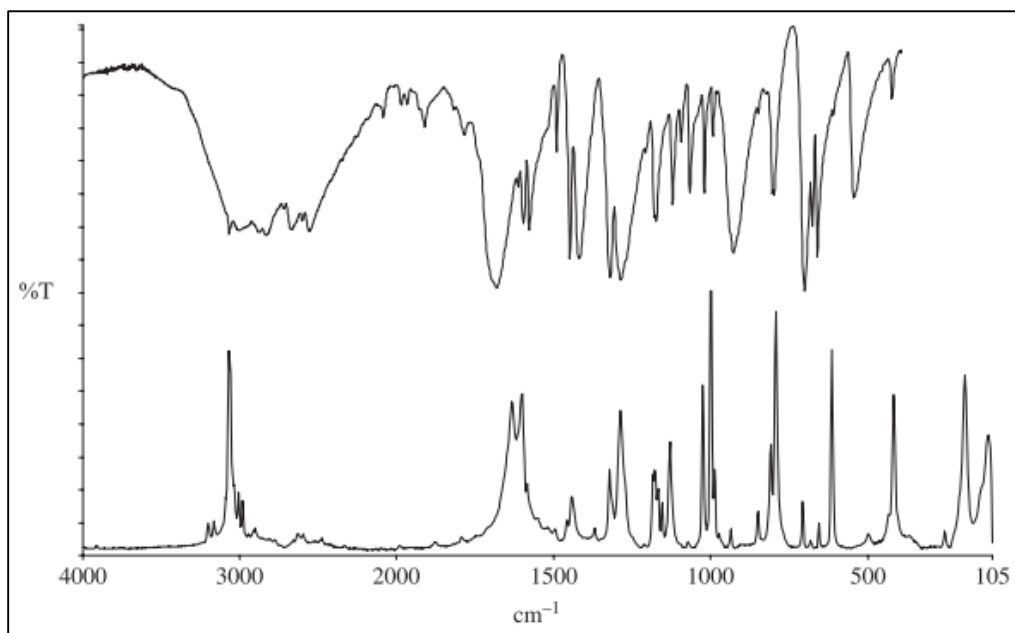


Figure 17. Benzoic acid measurements taken with Infrared and Raman Spectra. IR is on the top and Raman is on the bottom [21]

Figure 17 shows the infrared and the Raman spectra taken for the benzoic acid, top for the IR and bottom for the Raman. Even though the whole range of the spectra is taken when measuring with these methods, in general the information that the researchers are interested for the IR is between 3600 and 400 cm^{-1} , while for the Raman the range of interest is down to 200 cm^{-1} [21].

For the Raman spectra can be interpreted using previous knowledge taken over time: Between 4000 - 2500 cm^{-1} is where there is the absorption of singles bonds of the form X-H, where X is any component. For the range of 2500 - 2000 cm^{-1} is where multiple bonding is found, like -N=C=O [21]. On the range between 2000 - 1500 cm^{-1} is were double bonding take place, -C=O , -C=N and -C=C- . Below 1500 cm^{-1} groups like nitro can be found, O=N=O [21]. These are only examples of the great amount of groups and bonding that have been recorded.

Figure 18 shows an example of the different groups that can be observed using Raman between the range of 2600 and 1700 cm^{-1} :

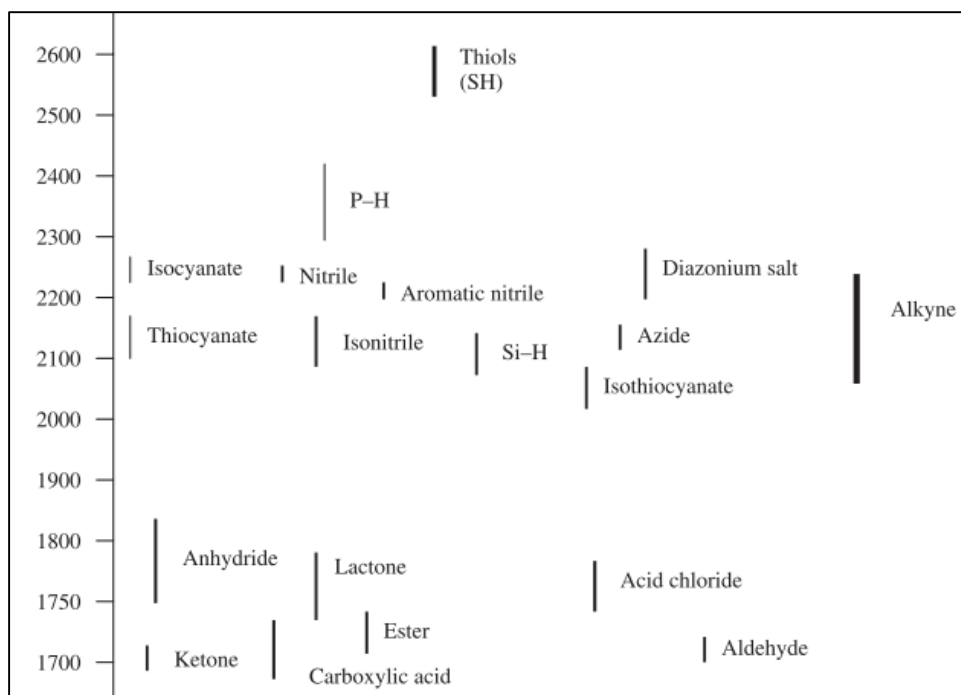


Figure 18. General peak intensities for several groups in Raman [21]

In the same way, using infrared a diverse quantity of peaks can be found in a spectra and each of those bands may represent a group or a type of bonding, which information can be found because this have been recorded before. On Figure 19 some of the characteristic wavenumbers specific to a certain chemical bond can be seen, which are found using IR spectra [22]:

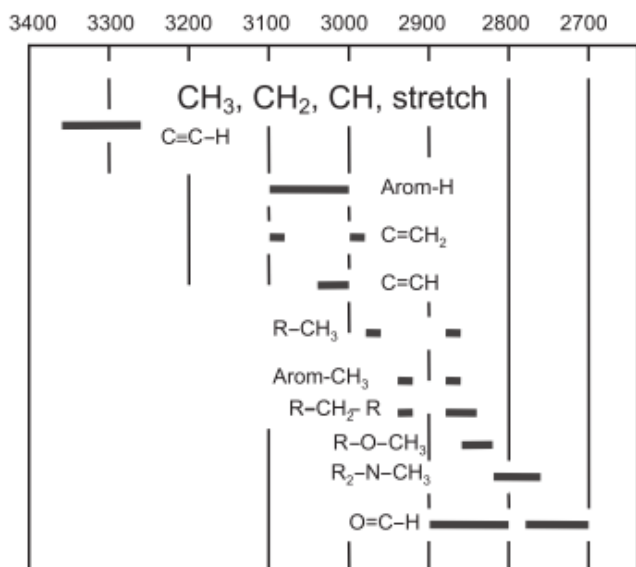


Figure 19. IR bands for CH₃, CH₂ and CH [22]

To summarize, Table 2 shows what are the advantages and disadvantages of using either Raman, infrared or near IR depending on what is needed to be measured.

Table 2. Raman, mid-IR and IR spectroscopy [22]

	Raman	Infrared	Near-IR
Ease of sample preparation	Very simple	Variable	Simple
Liquids	Very simple	Very simple	Very simple
Powders	Very simple	Simple	Simple
Polymers	Very simple*	Simple	Simple
Gases	Simple	Very simple	Simple
Fingerprinting	Excellent	Excellent	Very good
Best vibrations	Symmetric	Asymmetric	Comb/overtone
Group Frequencies	Excellent	Excellent	Fair
Aqueous solutions	Very good	Very difficult	Fair
Quantitative analysis	Good	Good	Excellent
Low frequency modes	Excellent	Difficult	No

However, it is important to remember that it is necessary to do preprocessing on Raman spectroscopy and the usual methods are known as: smoothing, averaging, mean centering and baseline correction [23]. A short explanation for each of these methods will be given next.

3.2. Smoothing:

Noise can cause some regions on the spectra to be read incorrectly so in order to clean the information, smoothing can be applied to eliminate or mitigate the noise but it should be done with care, otherwise important data can be lost in the process.

One of the most common used methods for smoothing, also the one used in this work, is called Savitsky-Golay and this method can be compare as graving each individual point and an impair number at each side of the main point selected in the moment of calculations, meaning 1, 3, 5, 7, etc., equal amount on each side [23].

Each point is assigned a weight or value, for example in a 7-point selection the center point is valued 1,0, the next points at each side of the main are 0,75, the second next to the main are 0,5 and the last on each side are 0,25. The weight of these points will be multiplied with the data and then divided by 4,0 which is the total weight, generating the average of the data [23].

Savitsky-Golay works in this way but instead of the average it uses polynomials and the weights of each point are calculated using software, which allow for more speed in the calculations. On figure 21 it can be seen the effect of smoothing in a spectrum by using 2nd and 3rd degree polynomials and changing the amount of points used on each case:

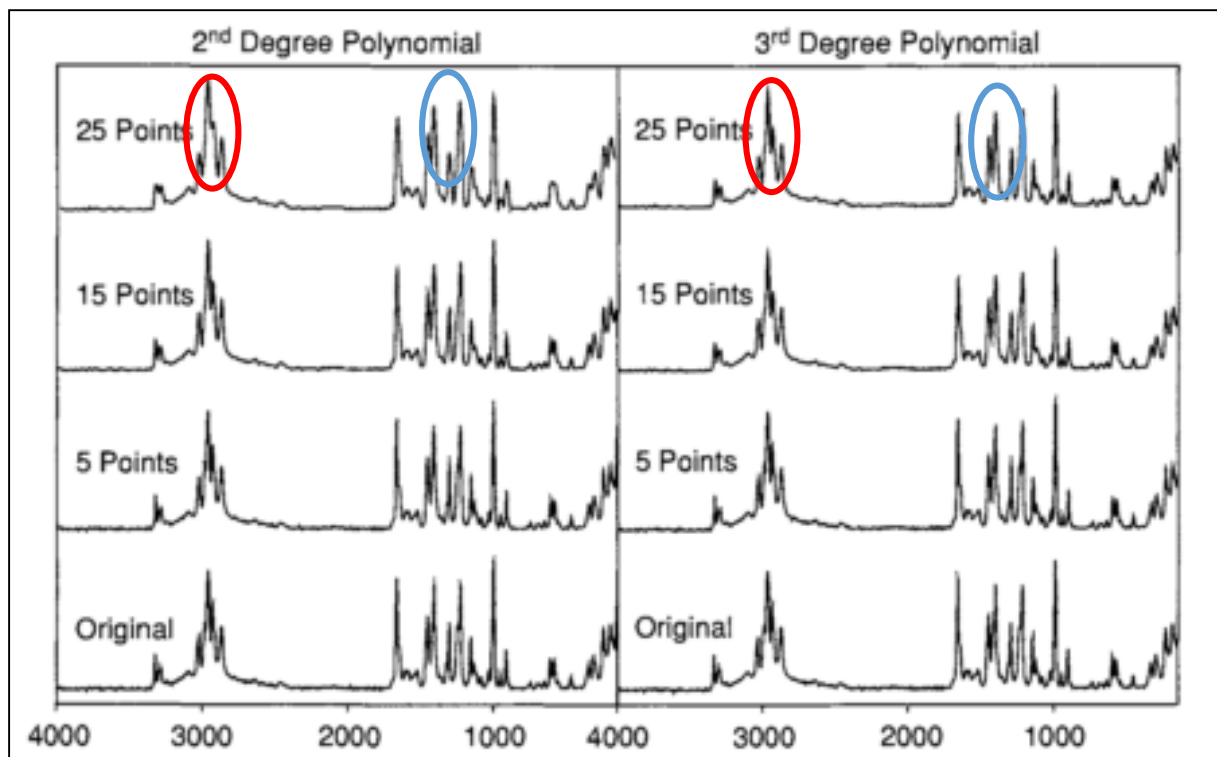


Figure 20. Effect of Savitsky-Golay smoothing [23]

From the figure it can be seen that a second and a third degree polynomial function was applied to the number of points taken from both sides of each original point were 5, 15 and 25. The effect of applying 5 points in each case can be seen to have little to no effect. The use of 15 and 25 points have significant effects like removal of the noise from the baseline and the decrease in the height of the band closer to 2000 cm^{-1} , which is observed in both sides (marked with the blue oval).

The main difference between the 2nd and 3rd order polynomial can be seen around 3000 cm^{-1} . In the center of the cluster of bands, it can be seen how the second-degree polynomial smoothest out the peak with the increasing number of points, so the bands start disappearing. However, this does not occur with the third degree (marked with the red oval), which is an example of how over smoothing can make some information get lost and how one must be careful with using Savitsky-Golay technique.

Summarizing, it was compared how the smoothing can contribute to decreasing the resolution of the spectra and at the same time the noise and the bands will get broader.

3.2.1. Normalization:

Measuring values with different scales can carry errors at the time of analyzing the data so it is necessary to make all the scales equal applying normalization. For example a set of spectra were taken for a single compound and all of them share a central frequency which used to divide the whole set, making all the frequency that are equal to the central equal to 1.0 and the remaining

ones are relative to the central frequency. For the remaining cases where it is not the same compound and a central frequency in common is not available, equation 4 can be used [23]:

$$I_{(v)} = \frac{I_{(v)}}{\sqrt{\sum I_{(v)}^2}} \quad (4)$$

Where,

$I_{(v)}$: intensity of a single frequency

In equation 4 each of the frequencies is divided by the square root of the addition of all the squares of the intensities [23]. The intensity of the frequency on the left side will represent the new value after normalizing and the intensity in the nominator is the old values before normalizing. On Figure 21, a set of 4 spectra from different mixture are shown, been the originals placed on the left side of the figure and the normalized on the right side, next to their respective raw spectrum. In order to compare correctly between this 4 different spectra, the respective weights of is taken into account and their relative intensities are calculated [23].

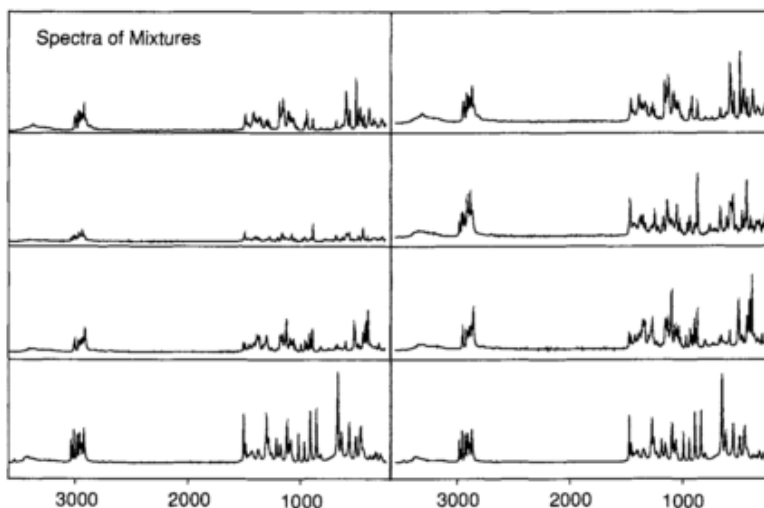


Figure 21. On the left side of the figure is the original Raman spectra of 4 compounds and on the right is the same spectra after applying normalization [23]

3.2.2. Mean centering:

These methods refer to calculating the average of all the intensities of the spectra and then subtract that value from the data, eliminating all the bias. This operation will be equal to taking the mean of the spectra and setting it to be the origin.

3.2.3. SNV or Baseline correction:

Finally, this last method (Standard Normal Variable transformation) is used to correct the baseline of the spectra when the baseline is not a flat horizontal line as shown in Figure 22. The method consists of using equation 5 to remove that slope variation on the spectra [23]:

Where,

SNV(ν): intensity of the frequency once SNV is applied

$I(\nu)$: intensity of the original frequency

n : is the number of frequencies

$\overline{I(\nu)}$: is the average intensity at each frequency.

Figure 22 shows a group of spectra before (left) and after (right) SNV has been applied, it can be seen how all the backgrounds end up alienated and the data can be compare after this step [23]:

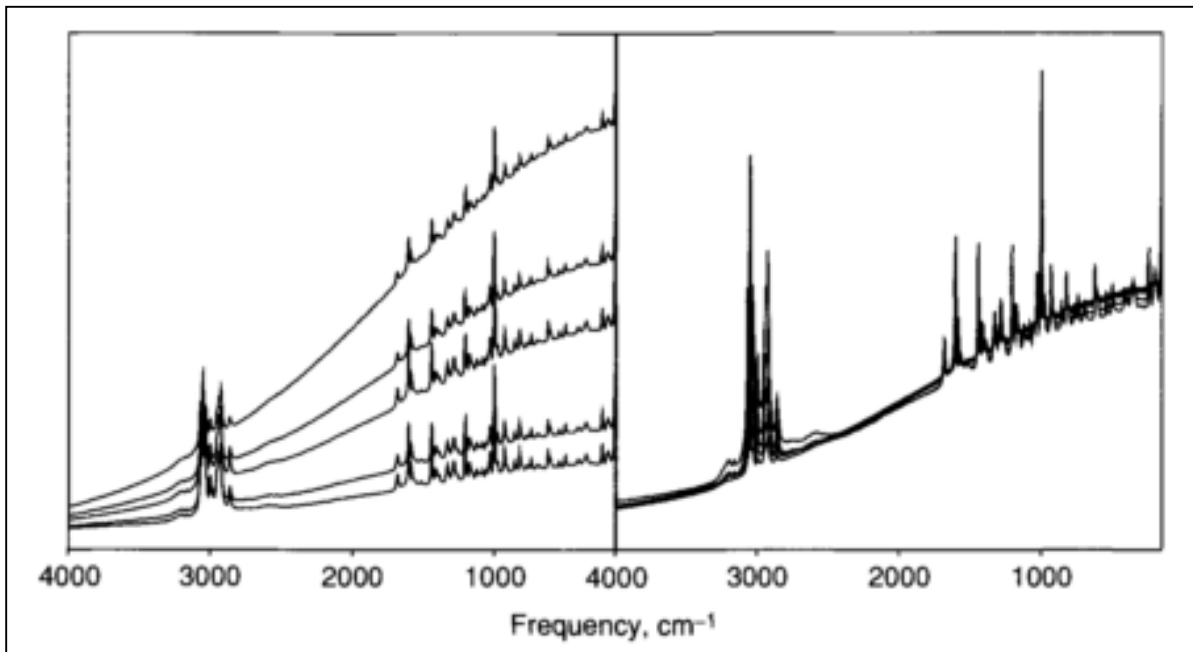


Figure 22. On the left of the figure are 4 Raman spectra of the same compound at different concentrations. On the right side the same Raman spectra after applying SNV [23]

3.3. Literature review for Raman

The first exploratory study of applying Raman spectroscopy (RS) to cementitious materials was carried out by John Bensted in the 70's [24]. Subsequently, in the 80's and 90's Conjeud and Boyer [25], Bonen [26] and other research groups [27], [28] have further expanded on using RS for cement phases. It is worth noting though that these studies were done before multi-channel

detectors and CCD-s (charge-coupled devices) became widespread in instrumentation. Since then the number of studies regarding Raman Spectroscopy have increased substantially.

Applying Raman spectroscopy is a challenging task in the case of fly ash because it exhibits a high level of fluorescence, which affect the spectra obtained, so some authors [29] had advised to use longer wavelengths (e.g. 785 nm or 1064 nm) to eliminate this problem. Using higher wavelengths result in photoluminescence, which are most likely due to rare earth elements in the fly ash. Another problem that can affect analysis is if the particles are too fine and if Portland cement is added to the mixture [29].

Using OPC (ordinary Portland cement) has anomalously high background signals, which could be attributed to a number of factors. The most likely culprits are either organic contaminants or inner particle scattering, which is caused by the grinding of the OPC.

Figure 23 shows three typical Raman shift for different types of fly ash (FA1, FA2 and FA3) performed by [29]:

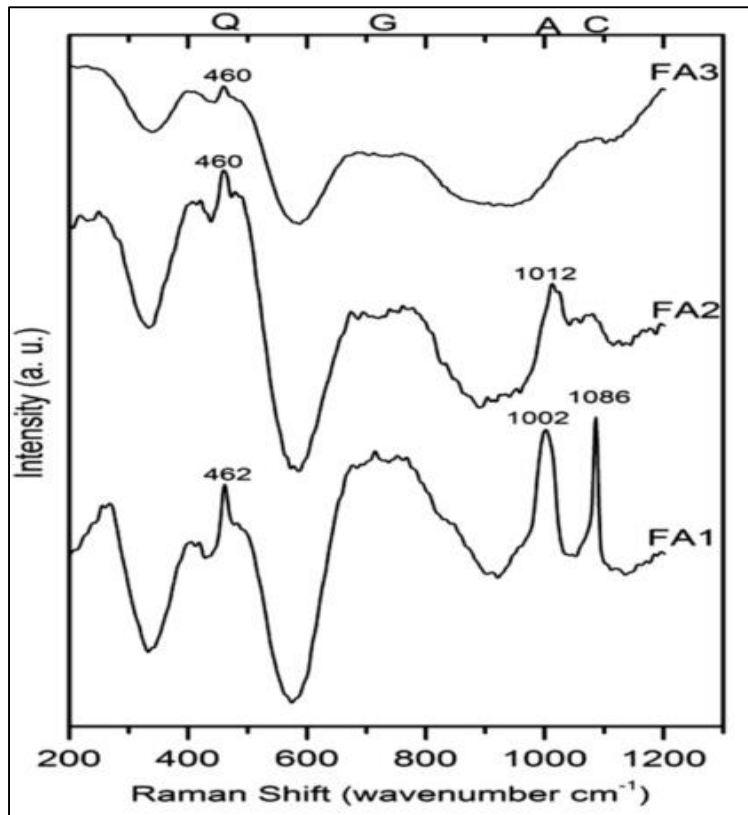


Figure 23. Raman shifts of three different samples of fly ash [29]

Not much literature is available in which Raman studies were performed on fly ash. Table 3 shows the most typical Raman shifts that could be expected in a general geopolymer, which was used to compare with the results.

Table 3. Typical Raman shifts found in a geopolimer [30]

cm ⁻¹	Raman shift							
Alumina	1381	1410			double peak			
Silicon	520							
Amorphous silica	540				broad peak			
Calcite	155	281	711	1087	not all visible			
Quartz	130	208	466		not all visible			
Gehlenite	620	656	690	910	not all visible			
Hematite	225	245	291	410	490	610	660	not all visible
CSH	650							broad peak

The table shows that in general the most typical peaks that are possible to be detected are three: alumina, silica and CSH. Using the values from the table it is possible to identify some of the peaks on Figure 24. Some characteristic peaks can be seen for the fly ash before the curing, like the quartz as a broad peak around 460 cm⁻¹ and calcite around 1087 cm⁻¹ [29].

However, because this substance is amorphous it is challenging to precisely detect more of the peaks from the clusters that are also reflected in the Table 3 with the note “not all visible” [30]. Figure 24 shows the typical Raman spectrum for Portland cement [29]:

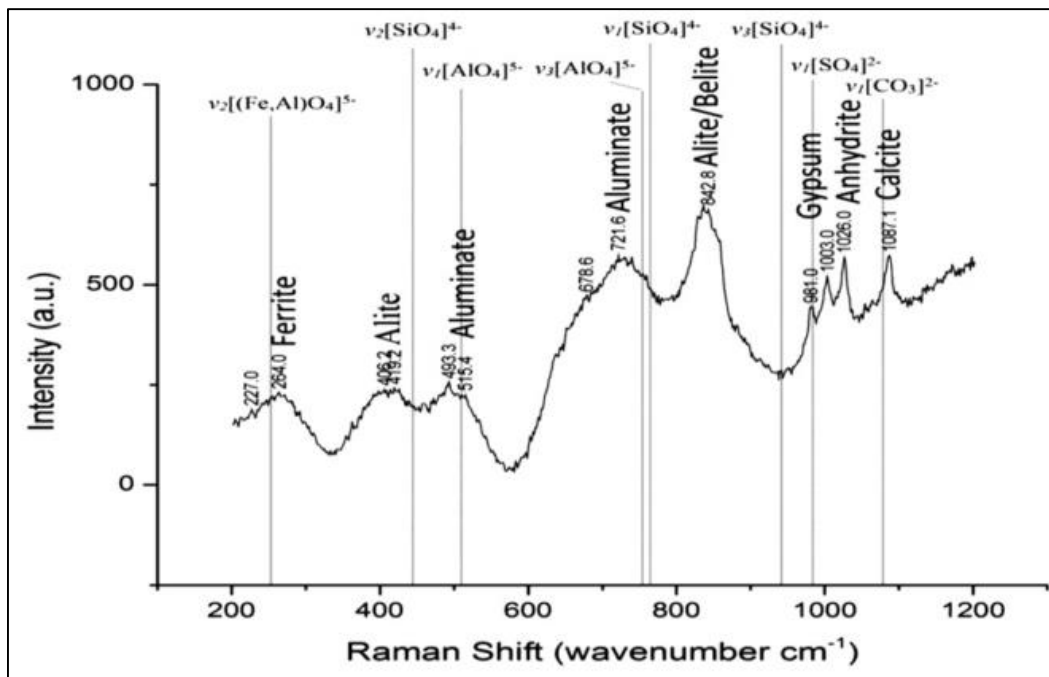


Figure 24. Raman shift for a typical Portland Cement sample [29]

Some of the typical peaks can be observed on the cement powder before mixing, like calcite (1087 cm⁻¹), ferrite (264 cm⁻¹) and aluminate (515.4 cm⁻¹) and some of them are shared with the geopolymers as shown in the table from Figure 24, e.g. calcite is also marked around 1087 cm⁻¹ [29] [30].

It is important to note that the way the peaks appear between 600 cm^{-1} and 1000 cm^{-1} shows the cement has some fluorescent properties, just like the fly ash and that is why it will be hard to identify some of the peaks that are inside the clusters [29].

On Figure 25 the Raman spectra taken from 3 samples of fly ash can be seen the after mixing. The mixtures were created to study and measure curing of the samples with respect to time.

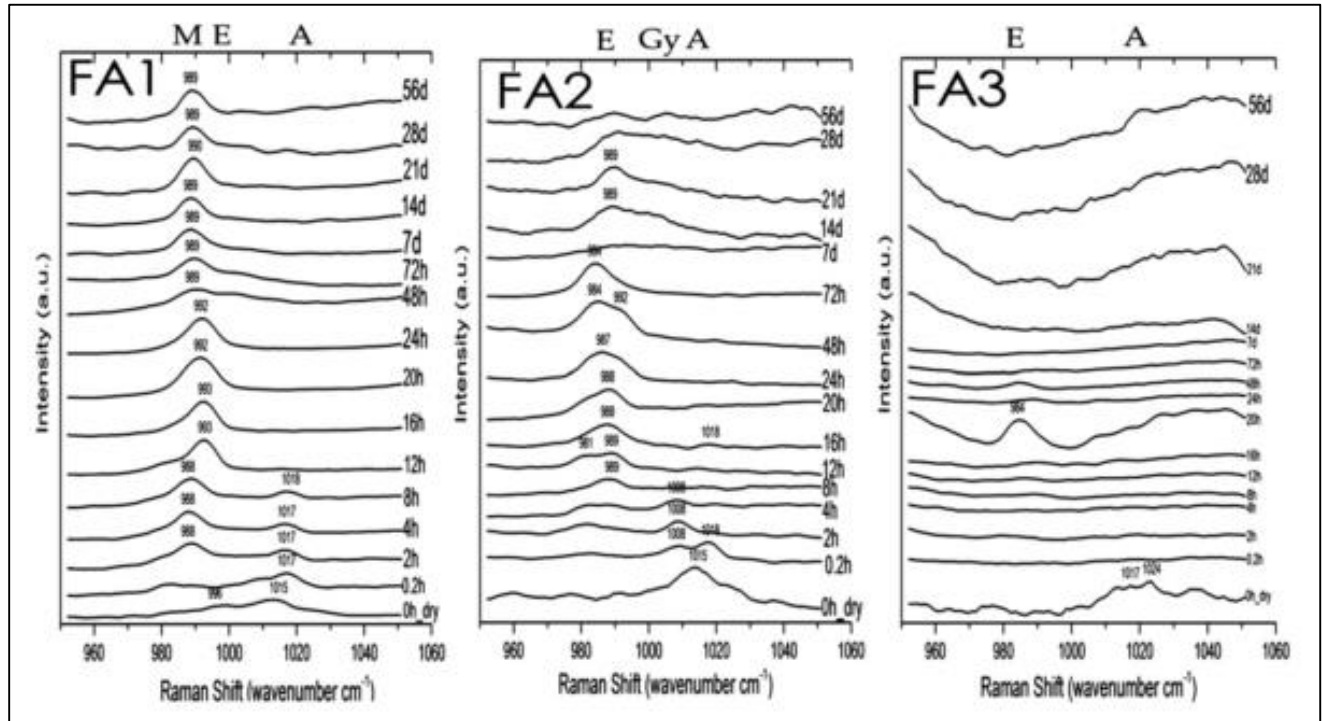


Figure 25. Raman measurements of three geopolymers based fly ashes with respect to curing time [29]

An evolution of the peaks can be observed with the curing time increasing until around 56 days at ambient temperature. The peaks around 1007 cm^{-1} is noted to be gypsum by N. Garg et al. [29] which is a mineral that is associated to calcite and its band should be located around 1087 cm^{-1} as shown in Figure 25.

Gypsum is also associated to other materials like anhydrite, chert or halite [31] and probably because of this the anhydrite band is found in geopolymer usually around 1026 cm^{-1} as shown in Figure 25, which is also close to the calcite band at 1087 cm^{-1} , as explained before.

However, one problem that was detected is the author of some of the papers like [29], [30] and many others don't show any type of data preprocessing like centering or smoothing in order to remove the noise and increase the accuracy of the results.

3.4. Literature review for IR

Just like with Raman, FT-IR can be used to measure the evolution of the curing of a geopolymer sample to compare with the pure fly ash component and taking the measurements in certain intervals. Often doing 4 weeks of total testing in order to observe the change in the intensity

of the peaks that are showing the breaking and formation of bonds, which are a product of the continuous polymerization reactions.

Figure 26 shows the FT-IR spectra for samples of a typical ash binder that were taken to determine the position of the main peaks to compare it with the fingerprints of the main molecular vibration for a typical geopolymer.

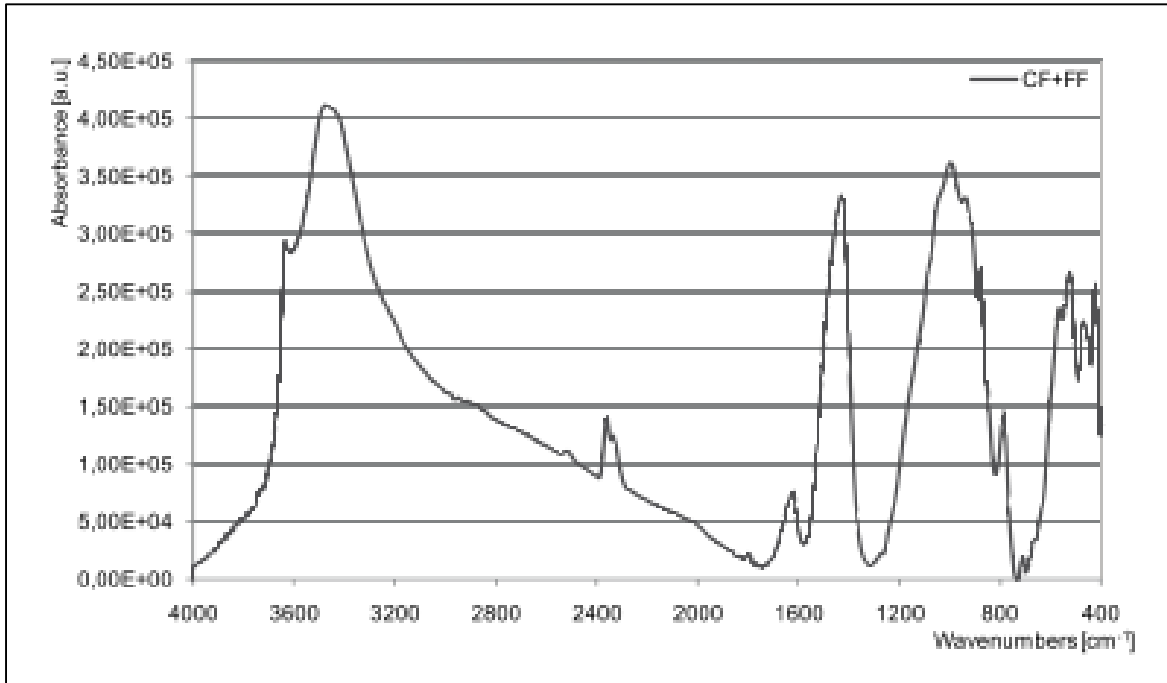


Figure 26. IR spectra for general ash binder samples [30]

On Figure 27 the FT-IR of the geopolymerization can be observed for specimen made from bottom ash. The samples were analyzed after a curing period of 7 days and 28 days.

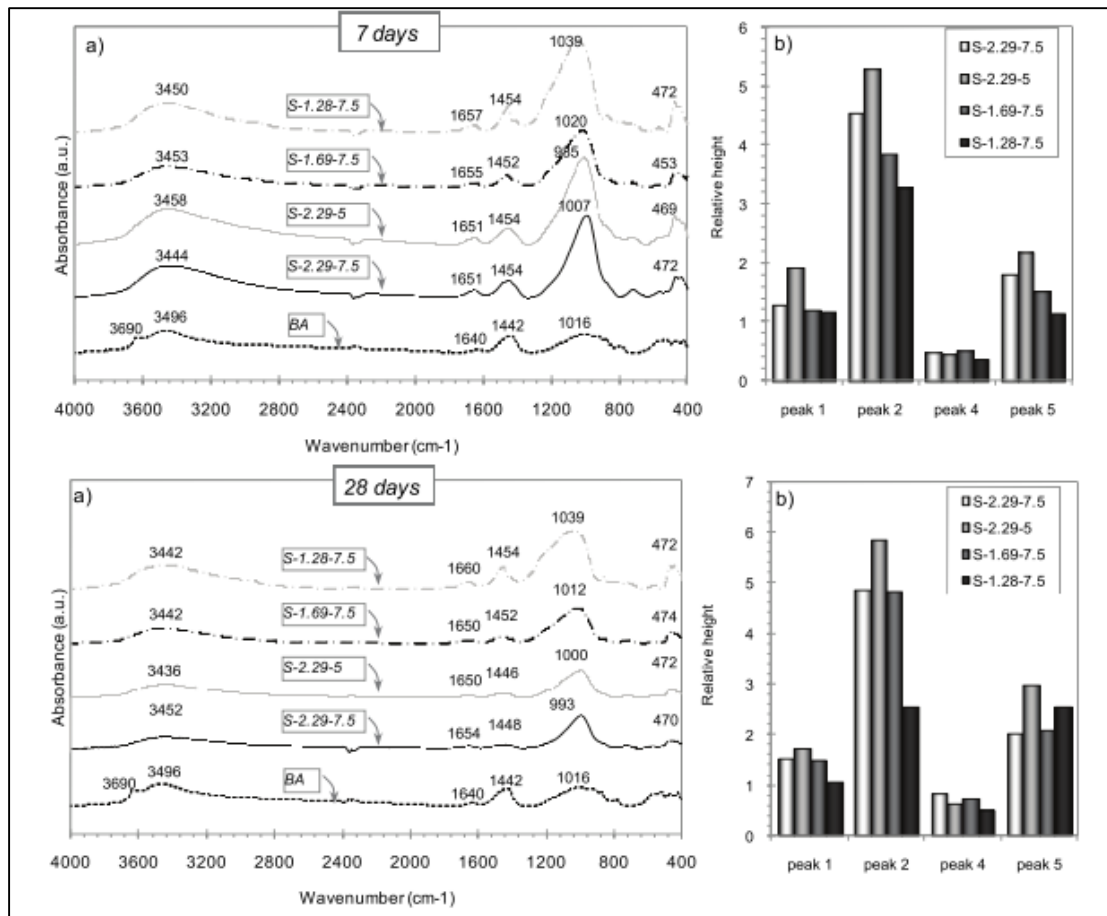


Figure 27. FT-IR taken from Bottom ash based geopolymer in curing times of 7 and 28 days [30]

From both Figure 26 and Figure 27 several peaks were identified that are characteristic of the geopolymer material. The band around 450-470 cm⁻¹ that represents the bending of Si-O-Si bonds, a band on 980-1040 cm⁻¹ that shows the stretching of bonds Si-O/Al-O, stretching of C-O-C on band 1450 cm⁻¹ that is typical in carbonate groups, among others that are represented in Table 4.

This geopolymers were created using bottom ash materials that comes from incinerators that had a particle size below 425 μm, the alkaline activators used for the reaction were sodium hydroxide between 10 and 15.5 M and sodium silicate solution with the next concentrations: 26.91% of SiO₂, 8.68% of Na₂O and 3.1 w/w% SiO₂/Na₂O.

A difference with other geopolymerization done was the use of metakaolin for adjusting to the desired ratio of Si/Al and it was obtained by doing calcination of commercial kaolin for 2 hours at 800 °C. The ratio of solids and liquids for the polymer mixture employed was 4 kg/l for most of the samples, the only exception was in the samples with higher concentration of metakaolin where the S/L ratio was 3,3 (which translates to 0,3 in L/S ratio) [30]. A detailed table with the compositions of the samples created can be observed in the appendix.

In general, it has been found out that the typical fingerprints of a geopolymer material are located between 980-1040 cm^{-1} and 450-470 cm^{-1} , similar to Table 3 which shows the main Raman shifts, in an IR spectra are shown [30]:

Table 4. Peak bonds typical in geopolymers [30]

Peak location (cm^{-1})	Type of bond
3690	O-H stretching in $\text{Ca}(\text{OH})_2$
1640-1660	Stretching of OH and H-O-H
3440-3460	Deformation of OH and H-O-H
1450	O-C-O stretching in carbonate
980-1040	Stretching of Si-O/Al-O bonds
450-470	Bending of Si-O-Si

It can be observed comparing both figures how the curing progresses. The band associated to Si-O-Al vibration around 800 cm^{-1} first appears in the slurry and later disappears progressively. It is then replaced with new bands with less intensity between 700 and 800 cm^{-1} [30] and it may represent the decomposition of some groups that contains Al. Because of the polymerization progressing the Al are added to the peak that represents the alumino silicate on the bands around 980 and 1040 cm^{-1} .

A similar study but with more curing time and using samples produced with alkaline solution and with water glass was performed during a longer period of time as shown in Figure 28.

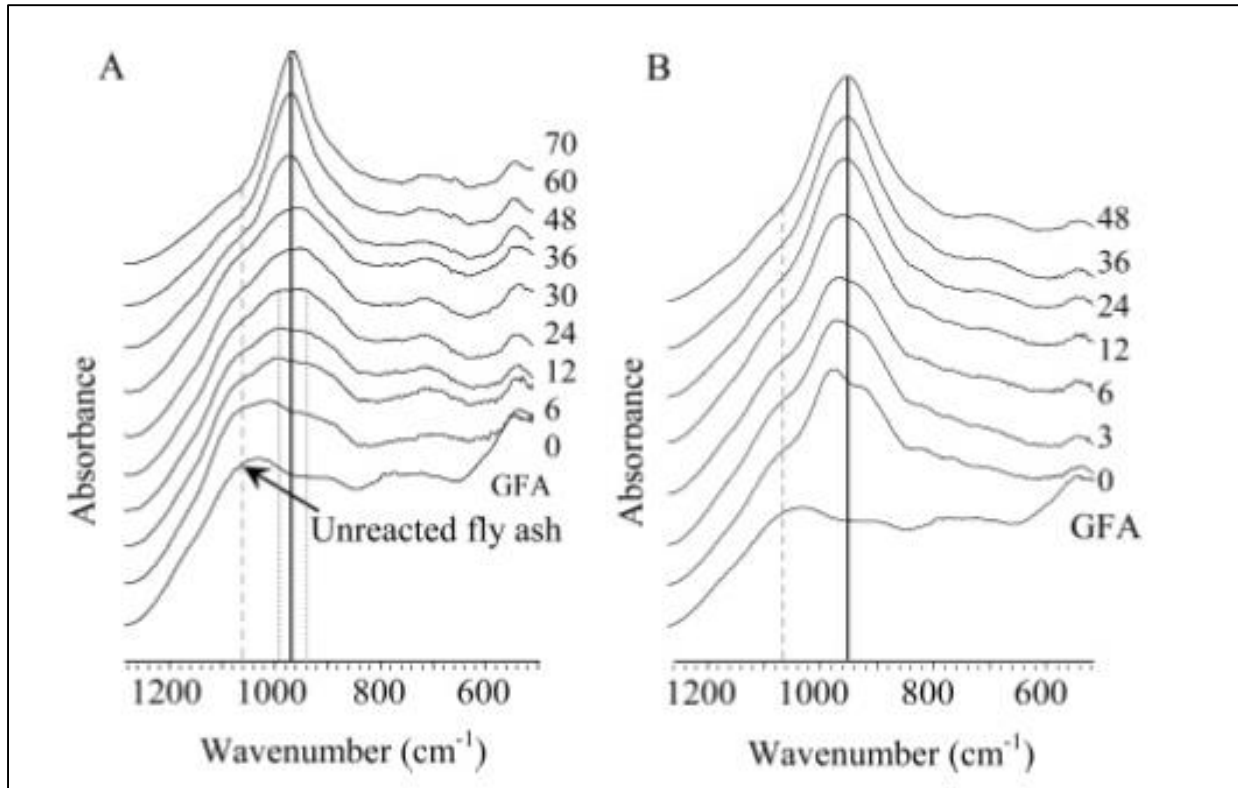


Figure 28. Fly ash geopolymer produced with alkaline solution (A) and with water glass and KOH together (B) [32]

In this experiment class F fly ash was used with sodium hydroxide and sodium silicate grade N solution as a secondary silicate in order to create the polymer. The ratio of Na/Al obtained was 0,5 and the left side of Figure 28 shows the curing development reach after 70 days of curing using NaOH as the activator. The right side of the figure is the evolution of curing during 48 days using water glass as the activator instead.

The author of [32] theorized the amorphous and glassy nature of the fly ash as the reason for the broad peaks in the spectrum obtained but he also agreed like some other researches that the main peaks for the geopolymers is found between 800 and 1200 cm^{-1} .

It was assumed the main band located in 1055 cm^{-1} to be the most important indicator of the geopolymerization and this band represents the Si-O-T stretching bond and in both figures it can be observed this peak was decreasing its intensity during the whole curing.

The main difference between the two types of experiments was that the same amount of intensity it took the alkali activated fly ash was 70 days while the water glass activated reached it in only 48 days [32], indicating a much faster reaction because of the addition of this secondary silicate.

The Si-O-T was marked as the dashed line in both figures and it was assumed to represent the unreacted fly ash from the beginning of the geopolymerization when the samples were slurries. In time the peaks should disappear because of the Al is transferred to another group and a new peak should form.

The main band shifted to a lower wavenumber around 965 cm^{-1} , forming a new band. The main reason for that is because the gel formation is rich in Al, increasing the intensity of the band during the whole curing in both experiments.

However, no preprocessing was done to the spectra for any of the FT-IR cases in order to make the plots smoother and decrease the noise, which is recommended when dealing with Raman and IR. Maybe the broad peaks that were shown in the figures for the FT-IR are a result of the lack of preprocessing which could be fixed by applying them to the data.

3.5. Experiments and results

3.5.1. Raman spectroscopy

Three types of samples were prepared to run these experiments: pure fly ash with water glass and potassium hydroxide, 50% mass of fly ash with 50% mass of Portland cement, water glass and potassium hydroxide, and finally pure Portland cement samples with water. The concentration of alkaline solution was change between 4 M and 6 M and the water glass employed was potassium silicate.

The nomenclature used to identify the samples was the next one:

0K64

Where the zero represents the number of days that passed since the mixing the reactants; this case is identified as the slurry, right at the beginning of the curing and the longest curing time reached was +28 days in some of the samples.

The K represents the alkaline solution employed, in this case it was potassium hydroxide; the other option would have been N for sodium hydroxide. The number 6 shows in what concentration the alkaline solution was and it changed between 4 for 4 M and 6 for 6 M. Finally, the last number, 4 in this case, shows the mass ratio between liquids and solids (L/D) and the next values were selected: 4 for a L/S of 0,4; 5 for a L/S of 0,5; 6 for a L/S of 0,6 and 7 for a L/S of 0,7.

For preparing the solution of potassium hydroxide, 6M, an amount of 168,76 g of KOH pellets were measured in a 0,5 L volumetric flask which was later on filled with distilled water until reaching the 0,5 L mark. The sample started heating up because of the exothermic reaction of the pellets dissolving and in order to cool the flask, a stream of water was passed around the outside of the flask. The preparation of the solution of potassium hydroxide with a concentration of 4 M was prepared in a similar way but using 112,36 g of KOH pellets in a 0,5 L volumetric flask.

In Table 5 it is shown the composition and the amount of the slurry samples that were used for the Raman experiments.

Table 5. Example of the samples prepared for the Raman experiments

Sample	Alkaline solution	Concentration of alkaline solution (M)	L/S ratio	Mass alkaline solution (g)	Mass water glass (g)	Mass of solids (g)	Mass of water (g)
0K44	KOH	4	0,4	8,77	8,76	43,76	N / A
0K47	KOH	4	0,7	8,78	8,78	25,01	N / A
0K64	KOH	6	0,4	8.77	8.76	43,75	N / A
0K67	KOH	6	0,7	8,77	8,77	25,04	N / A
0CF04	KOH	4	0,4	N / A	N / A	21,88	17,50
0CF07	KOH	4	0,7	N / A	N / A	12,52	17,49
0C04	KOH	4	0,4	N / A	N / A	43,75	17,50
0C07	KOH	4	0,7	N / A	N / A	25,03	10.01

For the samples labeled CF, that indicates it is a mixture of 50% mass of cement with 50% mass of fly ash, so if the number on the table for 0CF44 shows 21,88 g, it means that is the weight for each the fly ash and the cement used.

The Raman spectrometer used was a RamanRXn1 Analyzer that have a fixed wavelength of 785 nm and have a coverage of 100-4375 cm^{-1} . A picture of the machine can be seen in Figure 29.



Figure 29. Raman spectrometer used for analyzing cement samples

The spectrometer is connected to a probe that is used to take the measurements. The laser is transferred from the instrument through a fiber-optic cable. The sample is placed inside the black box, which also contains the Raman probe. The black box makes sure that there is no natural light inside the box, because it could disturb the Raman signal, which is very weak compared to Rayleigh scattering. The measurements are taken and stored in the software of the laptop where some features can be controlled depending of the desired method of sampling.

The procedure for preparing the samples consists in taking the amount marked in Table 5 for the fly ash and mix it by hand for at least 10 minutes with the respective amount of water glass and potassium hydroxide. Once the samples were mixed, they were stored in small plastic red cap containers and the bubbles were attempted to be removed by leaving the samples for a few minutes inside an ultrasonic mixer.

The samples were stored at ambient conditions during the periods of time they were not used for measurements. An example of some of the samples inside the containers can be observed on Figure 30:



Figure 30. Example of samples created for Raman and IR experiments

On Figure 31 the raw spectra for the sample K44 can be seen, which was taken right after synthesizing while the samples were in their slurry state and after 28 days of curing. This particular sample was done with 4 M KOH as the activator and 0,4 ratio of L/S. The reason for only taking the spectra at the start of the curing and after 28 days was that one of the cables of the Raman was damaged. The cable took a large amount of time to fix thus a new set of experiments could not be performed on time.

Nevertheless, the spectra taken still provided enough information to work with. In Figure 31 it can be observed that preprocessing is needed on both spectra in order to compare them. Tail removal on both sides (marked with red square) were deemed necessary in addition to centering and smoothing of the whole data.

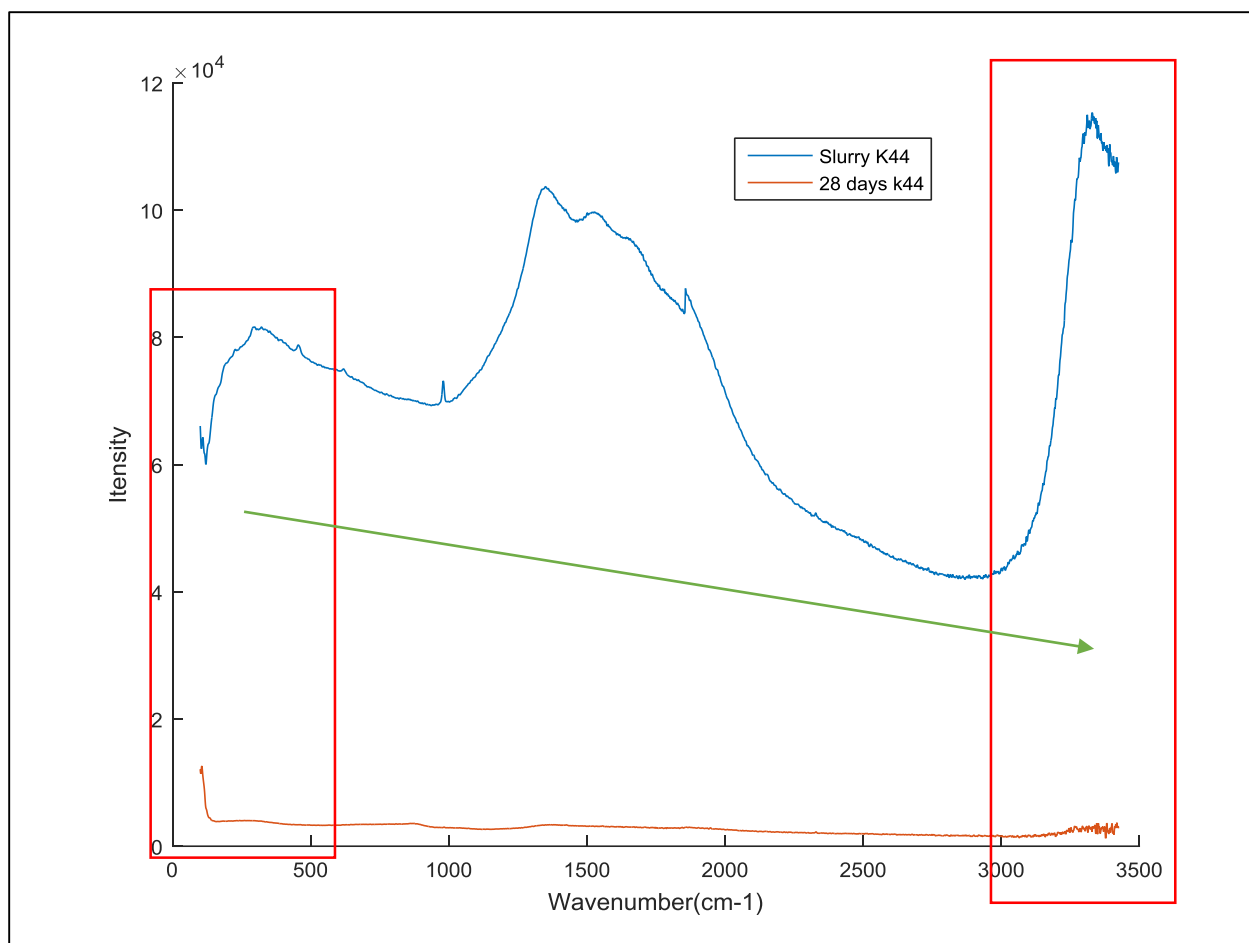


Figure 31. Raman spectrum for the slurry of K44 and the sample after 28 days of curing

After removing both tails before 400 cm^{-1} and after 3000 cm^{-1} , doing centering and baseline correction and normalization to make sure both spectra are leveled and have a relative size of peaks similar. Figure 32 shows the comparison with the raw spectra and the positive effect of processing can be seen in the resulting plot.

The baseline from the slurry sample (colored in blue) is a lot less stepped and is now in the same level than the 28 days sample. The noise is also removed by making the spectra smoother and this way a lot more peaks appeared. By normalizing the data and making sure all the peaks in both spectra have a common relative intensity, it is possible to observe how the curing takes place. The progressive appearance and disappearance of the specific peaks can be observed that govern the polymerization.

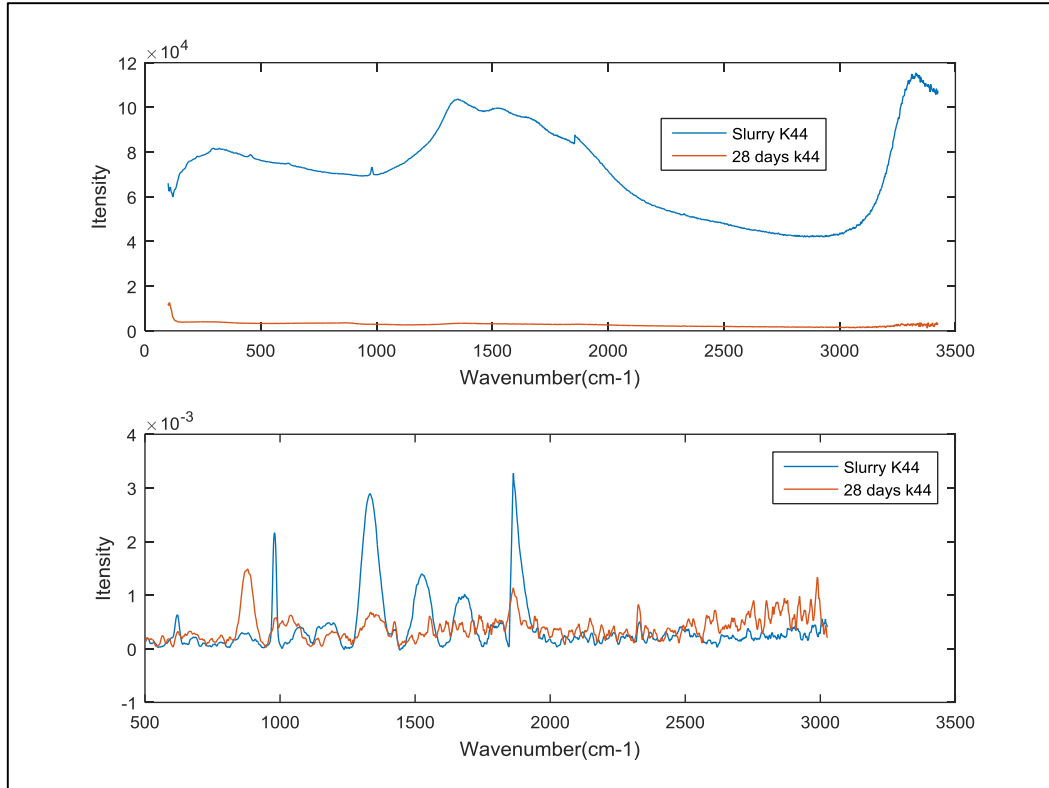


Figure 32. Sample K44 before and after preprocessing

Table 6 is a recompilation of the main peaks that are studied in cement and general geopolymer Raman experiments.

Table 6. Raman shift for cement and geopolymers pastes [33]

Chemical component	Raman Band (cm^{-1})
C_3S	834-848
C_2S	846-864
Gypsum	1007-1020
Calcium Hydroxide	1400-2000
Ettringite	987-992
Alumina	1381-1410
Silicon	520
Amorphous silica	540
Calcium silicate hydrate	650

The modified spectra are shown on Figure 33 in order to be able to observe the band shift with more detail, which are marked in different colors. It should be noted that after doing preprocessing the cluster and broad peaks that are usually seen in the literature are mostly not present. This would be an advantage that should be considered even with the risk of losing information, but this problem was not considered of importance after the figures were analyzed.

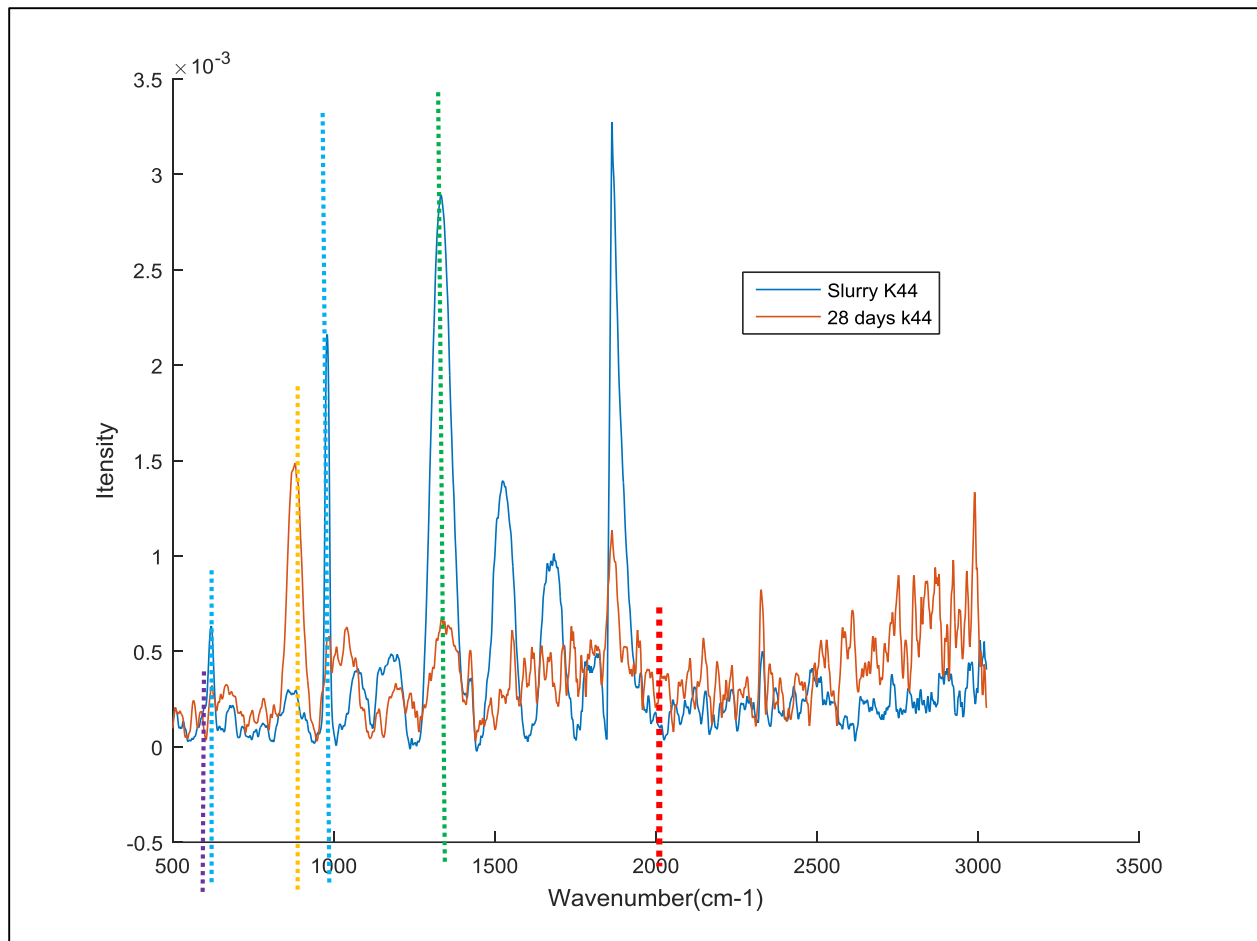


Figure 33. Raman spectra for sample K44 after the preprocessing

A great amount of the expected bands that should be shifting during the polymerization are in the figure but only some of them will be named to show how the curing takes place.

From Table 6 it can be observed that there should be a peak around 1411 cm^{-1} which represents the Alumina that is being consumed as part of the polymerization. This is reflected with the decrease of intensity from the slurry state to lower values after 28 days of curing. This band was marked with a green dashed line.

The band around 670 and 1000 cm^{-1} (colored with blue dashed lines) represent Gypsum and when these bands fade away during the polymerization a band around 988 cm^{-1} appears, which represents the production of Aft (ettringite), which was colored in yellow.

On the other hand, the band around 650 cm^{-1} represents the calcium silicate hydrates or C-S-H and this should be consumed while the curing takes places and it was marked with the purple dashed line. At the same time calcium silicate or CH should be produced in more quantity which can be verified with an increase of intensity in the 2000 cm^{-1} band, which effectively is occurring and it is marked with the red dashed line. This occurrence with CSH and CH was explained by [1].

In a similar way, other samples were treated in order to show the validity of the process to analyze the plots. Figure 34 shows the raw data for the slurry and the 28 days curing of sample K64, which identify a mixture of pure fly ash with 6M KOH and 0,4 ratio of liquid and solids.

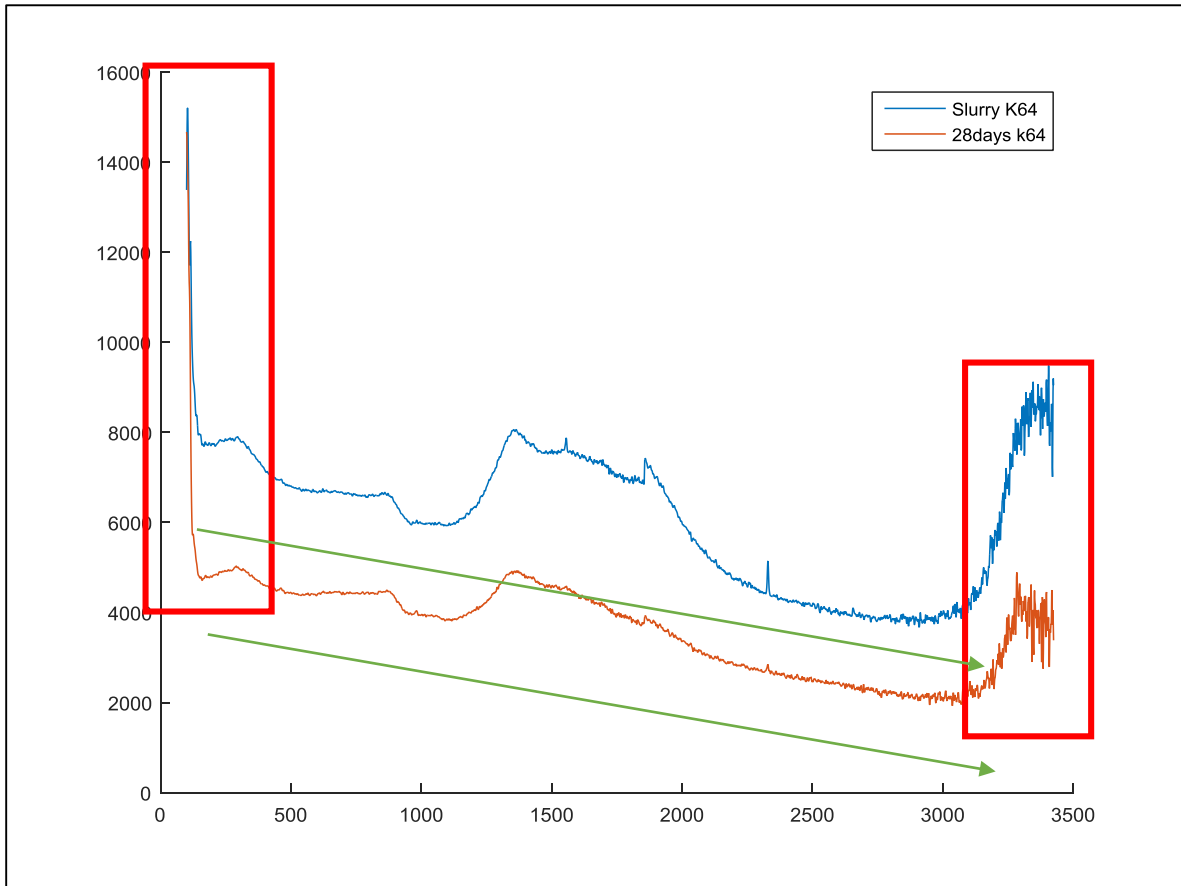


Figure 34. Raw Raman spectra for sample K64 as slurry and after 28 days

As per the case for sample K44, this new data also required preprocessing work that specially includes the elimination of the tails because of all the noise that can be observed before 500 cm⁻¹ and after 3000 cm⁻¹. There is the need one more time of perform baseline correction for both spectra because a descending slop can be observed in the figure and this was marked with a green line. The spectra need to pass though smoothing with SNV and centering also before comparing the results.

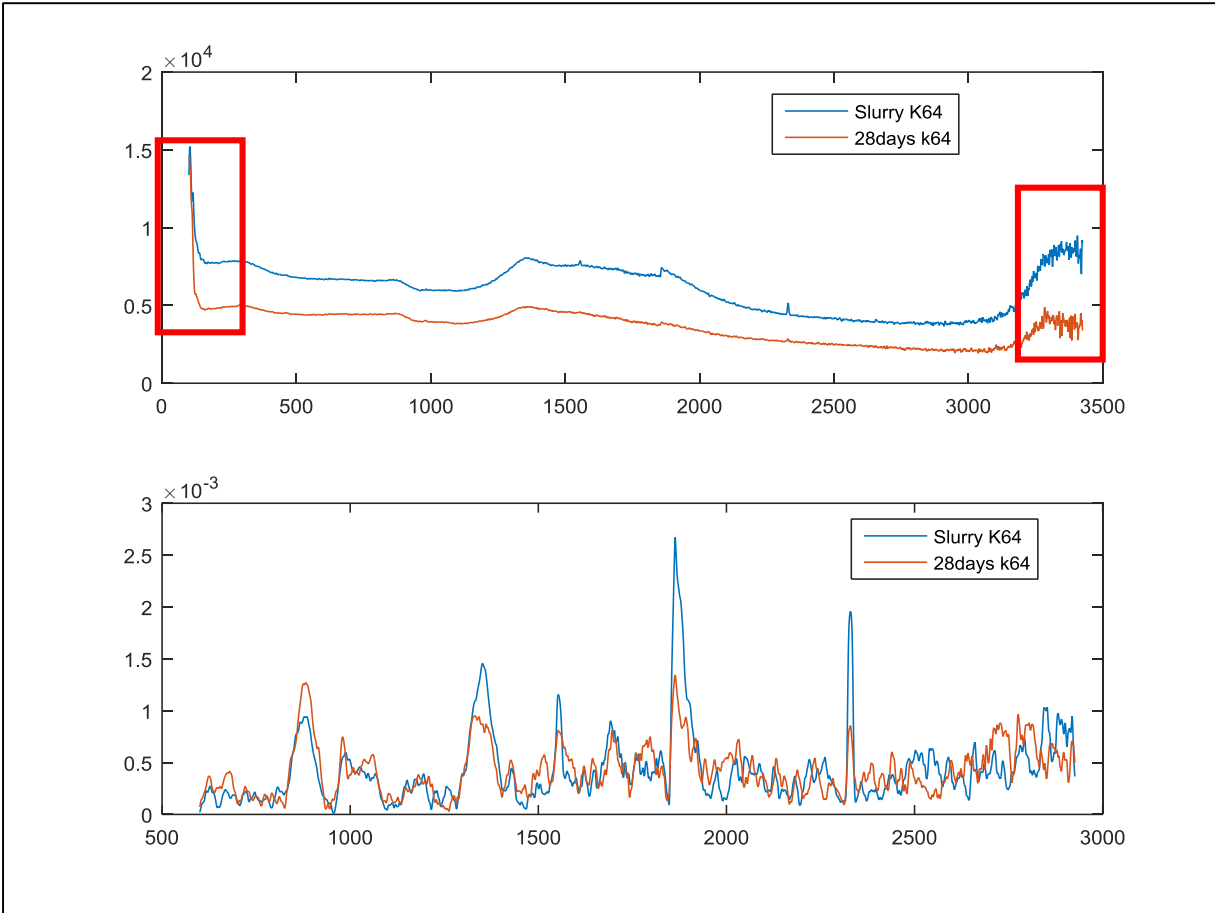


Figure 35. Raman spectra of slurry and after 28 days of K64 sample

The resulting change can be seen in Figure 35 at the bottom. Most of the peaks that were analyzed for sample K44 can also be observed in this case. The present bands were marked and table 6 was created to summarize these results enumerates the type of shift and the wavenumber at which it occurred.

Table 6 was used again to compare the band shifts that occurred with the sample K64

Chemical component	Raman Band (cm ⁻¹)
Alite C ₃ S	834-848
Belite C ₂ S	846-864
Gypsum	1007-1020
Calcium Hydroxide	1400-2000
Ettringite	987-992
Alumina	1381-1410
Silicon	520
Amorphous silica	540
Calcium silicate hydrate	650

The Alumina band around 1411 cm^{-1} is shown to decrease in intensity from the slurry state to the +28 days, indicating the consumption of alumina in the reaction. The band around 1000 cm^{-1} colored in a dashed green line shows the presence of Gypsum and the band fades during the 28 days curing. A band around 988 cm^{-1} marked with a red dashed line appears instead and again it shows the production of Ettringite, just like with the first sample.

The band around 650 cm^{-1} that shows the carbonation of C-S-H decrease during the +28 days curing and it is marked with the green dashed line. The band around 2000 cm^{-1} increasing in intensity after curing shows the formation of CH and usually is related to the carbonation of CSH; it was marked with a yellow dashed line. This occurrence with CSH and CH was explained by [1].

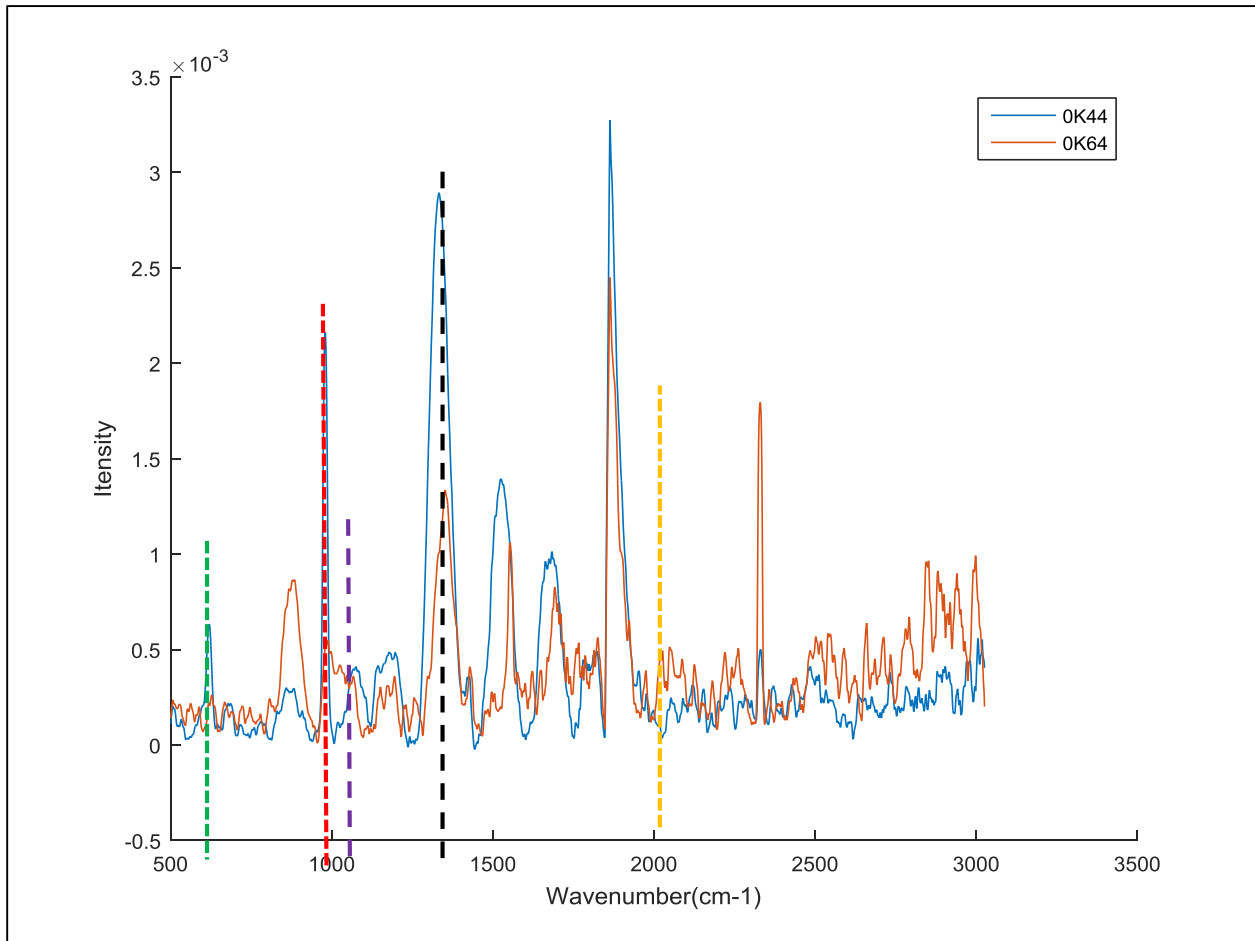


Figure 36. Comparison between slurries for samples K44 and K64.

A peak that is more clearly seen in Figure 36 can be seen at both side of the red dashed line shows the formation of calcite, which happens with the disappearance of the peak at the left and the increase of a broad peak at the right side of the red line. Table 7 shows the typical bands that are found in the geopolymers:

Table 7. Typical bands for the fly ash based geopolymers.

Chemical component	Raman Band (cm ⁻¹)
C3S	834-848
C2S	846-864
Gypsum	1007-1020
Calcium Hydroxide	1400-2000
Ettringite	987-992
Alumina	1381-1410
Silicon	520
Amorphous silica	540
Calcium silicate hydrate	650

A comparison of the spectra after 28 days of curing for cement samples with a liquid and solid ratio of 0,4 and 0,7 and they were represented on Figure 37.

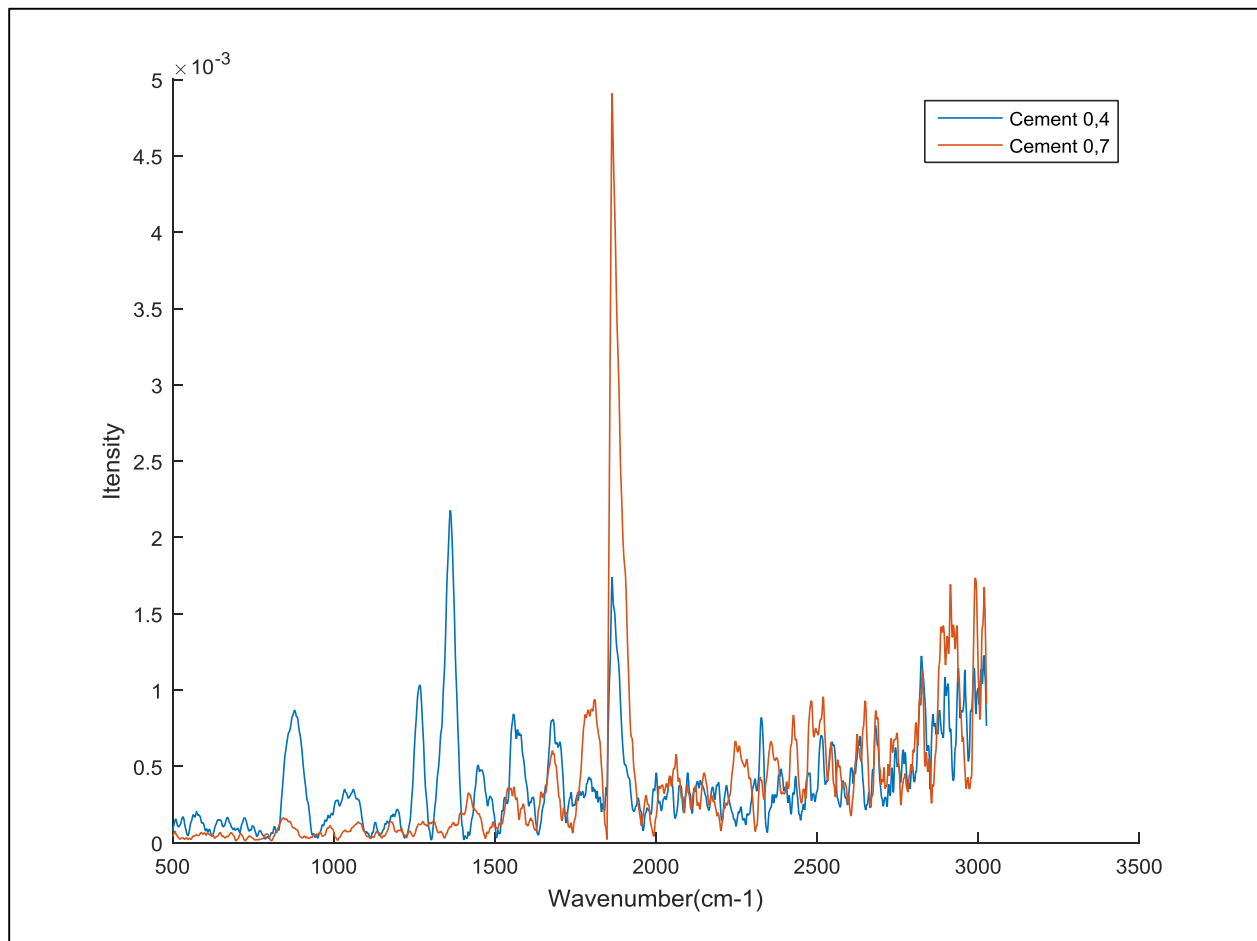


Figure 37. Comparison between slurries of cement for L/S ratios of 0,4 and 0,7

From Figure 37 it can be observed that most of the peaks for the cement with ratio 0,4 are of a higher intensity when compared to the other sample and this may be because of the less quantity of water in the sample. The reaction is occurring faster than the other and a major number of these peaks appeared after the immediate addition of water [34]. The only peak that shows a bigger intensity for the ratio of 0,7 is around 1800 cm^{-1} and in the same way it would be because the amount of water is higher and the reaction is slower.

Figure 38 shows the comparison of the slurries samples 0K64, 0K65 and 0K66, in order to observe if there is any important difference between them.

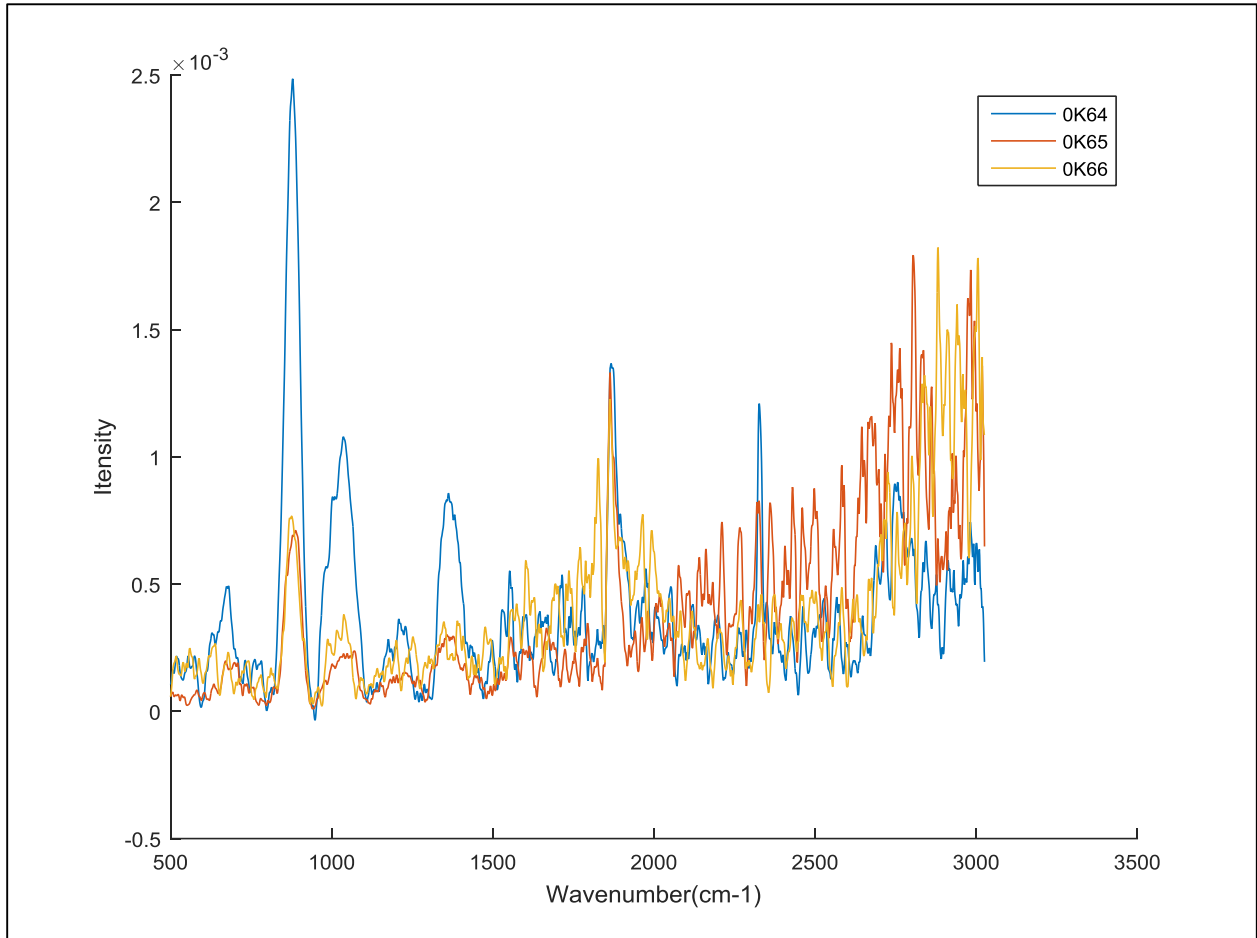


Figure 38. Comparison slurries with KOH 6M and L/S 0,4; 0,5 and 0,6

The same way with the comparison of the cement, in this case the amount of liquid shows it affects the slurries composition at the beginning of the curing and in theory will make faster the reaction. The speed of the polymerization should increase if the amount of liquids is smaller, meaning the fastest case will be for the L/S of 0,4 and the slowest will be for 0,6.

It can be see that for the case of 0,4 which is colored in blue the intensities of the peaks are higher around 650 cm^{-1} , 800 cm^{-1} , 1000 cm^{-1} and 1400 cm^{-1} . The thickness of the sample with 0,4 ratios was also the biggest and that would be because the faster curing.

Finally, the comparison between slurries is done with the samples for the two different KOH concentrations on Figure 39: 4M and 6M.

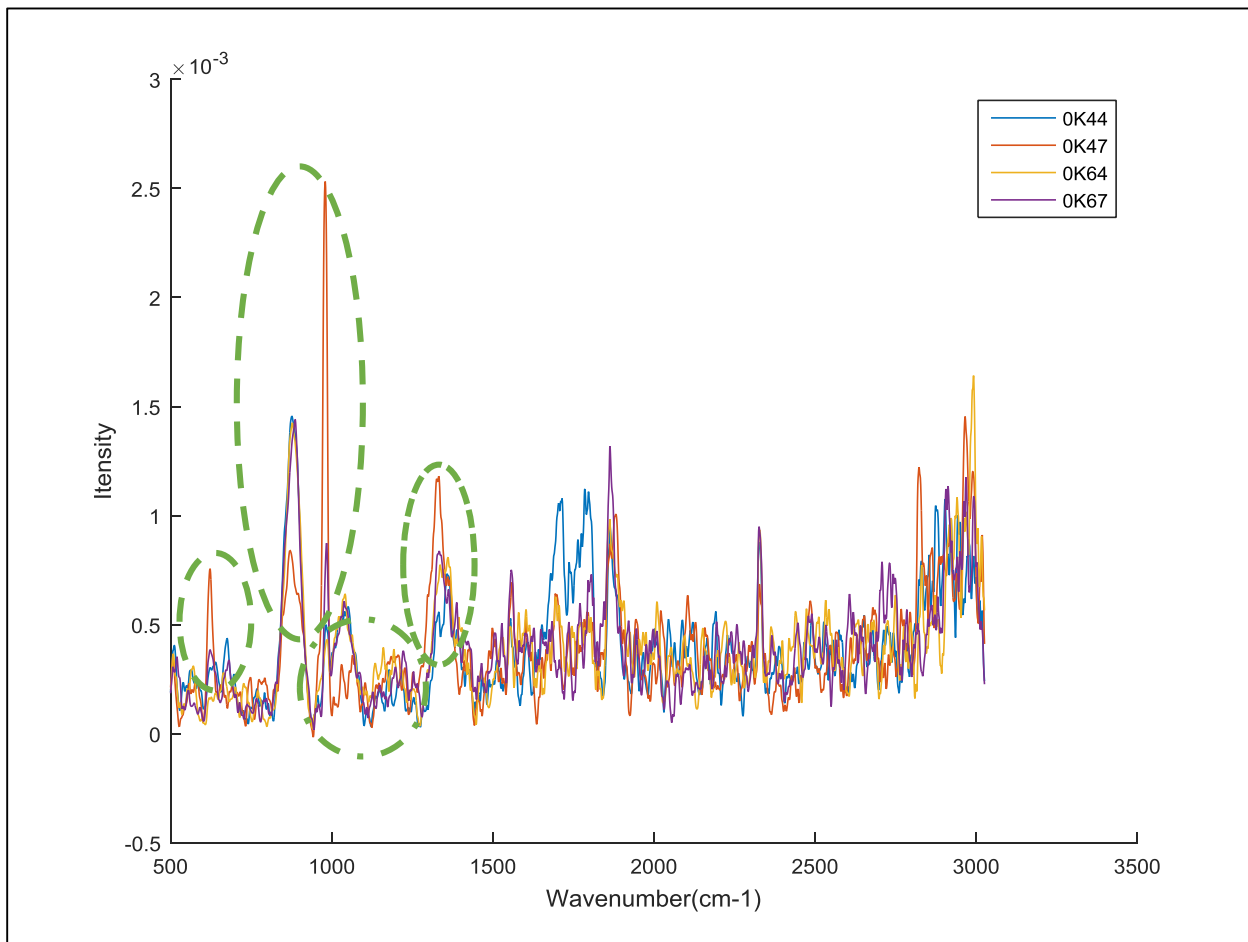


Figure 39. Comparison of all the slurries

Maybe because of the noise and the lack of repeatability, not much significant analysis could be extracted from the figure. However, it should be noted for example the cluster of peaks between 1500 and 1800 cm^{-1} . From the peaks marked with green ovals, it can be observed how the band shifts for the sample 0K47 in three locations possess the highest intensity while in two it shows to have the lowest intensity. The reason for this may possibly be that this sample has less concentration of KOH and the highest amount of water, making the reaction slower than usual. The characteristic peaks are located in 650 cm^{-1} , 850 cm^{-1} , 950 cm^{-1} , 1050 cm^{-1} and 1400 cm^{-1} .

3.5.2. FT-IR

The infrared measurements were performed using Thermo Scientific Nicolet iS 5 FT-IR Spectrometer with iD5 ATR Accessory. The experimental setup can be seen in Figure 40. The spectra taken were averaged from 16 scans with the background subtracted from them. The spectra were measured from 525 cm^{-1} to 4000 cm^{-1} .



Figure 40. FTIR-ATR used to measure cement samples

The rotatable arm on the top of the machine ensures that the sample is in contact with the diamond window and that there is no air trapped between the sample and the window. A measurement in progress is shown in Figure 41. The concrete samples had to be ground to a fine powder in order to get the best quality spectra.

Table 8. Characteristic IR bands characteristic for cements

Vibrational mode	IR Band (cm^{-1})
H-O-H deformation	3440-3460
O-H stretching	1640-1660
Ettringite Si-O stretching	1000-1200
Carbonate O-C-O vibration (out of plane)	750-1000
T-O-Si (T = Al or Si) str.	980-1040
Al-O-Si	680-730
Al-O stretching	580-620



Figure 41. IR measurement of a geopolymer sample in progress

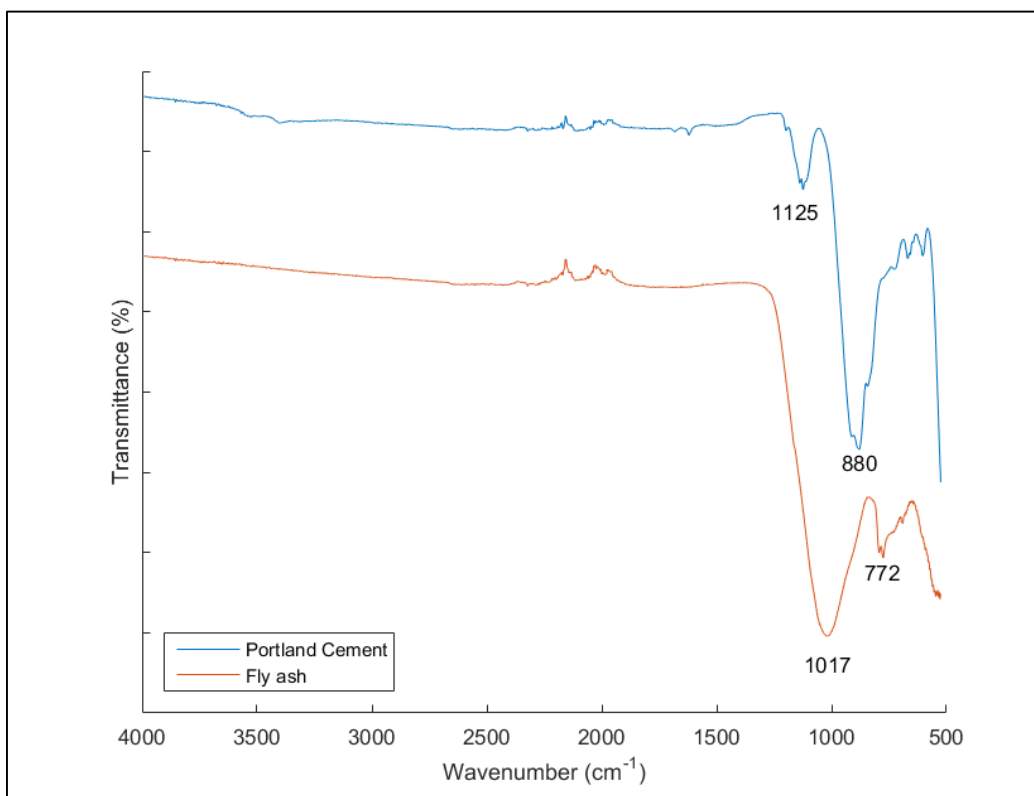


Figure 42. IR spectra of fly ash and Portland cement

Figure 42 shows the recorded IR spectra of class G Portland cement and class F fly ash received from DONG Energy A/S, Esbjergværket. Vibrations around 500 cm^{-1} also seem to be significant, these can be attributed to the in-plane bending vibration of Si-O-Si links, but unfortunately, the spectrometer could not measure below 500 cm^{-1} to conduct more studies. The

band at 880 cm^{-1} in Portland cement is attributed to out of plane vibration of CO_3^{2-} . The band appearing at 1125 cm^{-1} corresponds to the stretching vibrations of the Si-O bond of gypsum and ettringite [35]. The fly ash has two distinct peaks, the first one at 1017 cm^{-1} , which is related to T-O-Si asymmetric stretching (where T = Si or Al). The other band at 772 cm^{-1} is most likely a symmetric vibration of Al-O-Si [36].

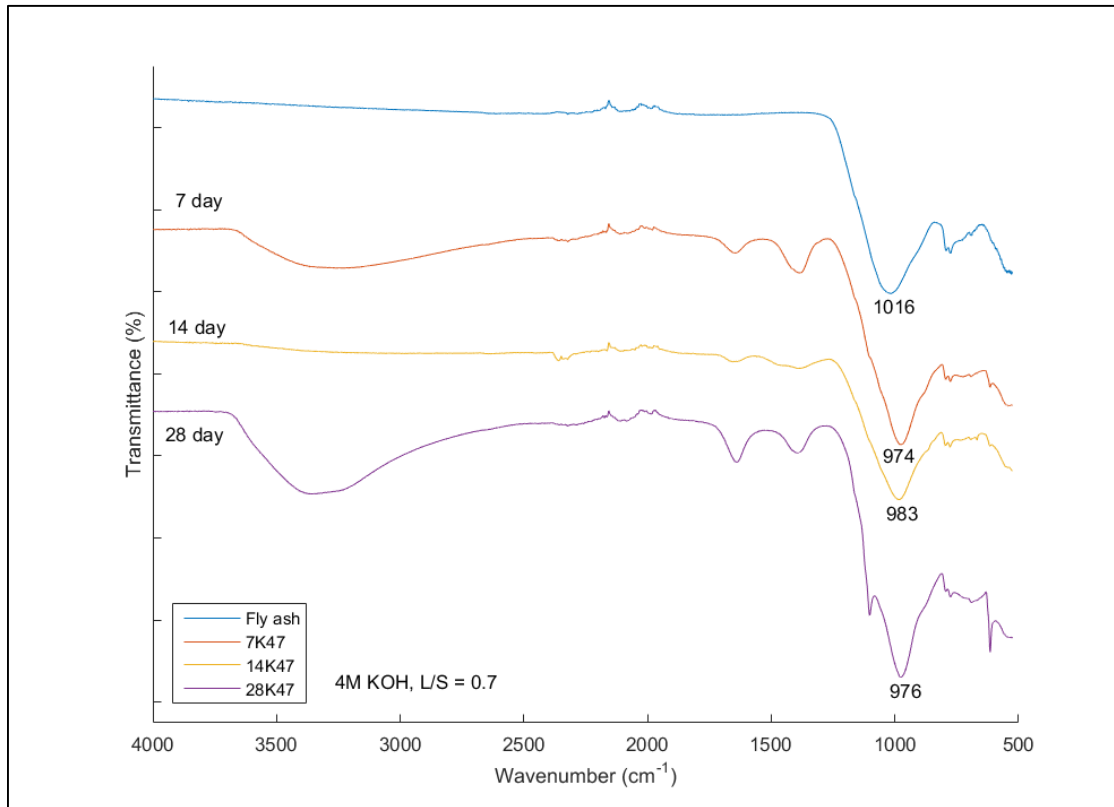


Figure 43. IR spectra of fly ash geopolymer with respect to time

The spectra shown in Figure 43 were taken from the same sample after 7, 14 and 28 days with the unreacted fly ash shown as reference. The geopolymers still have the dominant peak centered around 1000 cm^{-1} (T-O-Si stretching) but it can be observed that after seven days the peak became narrower and shifted to lower wavenumbers. This narrowing means that the material became less glassy compared to the unreacted fly ash, which is not surprising considering the activators and waterglass used in to synthesize the samples. The broad peaks in the 7- and 28-day measurements between $3700\text{--}2500\text{ cm}^{-1}$ are attributed O-H and H-O-H groups [30], which are adsorbed on the surface. Surprisingly the 14-day sample shows close to none of this band. The reason for this could be that the 14-day sample was more dried out during the measurement.

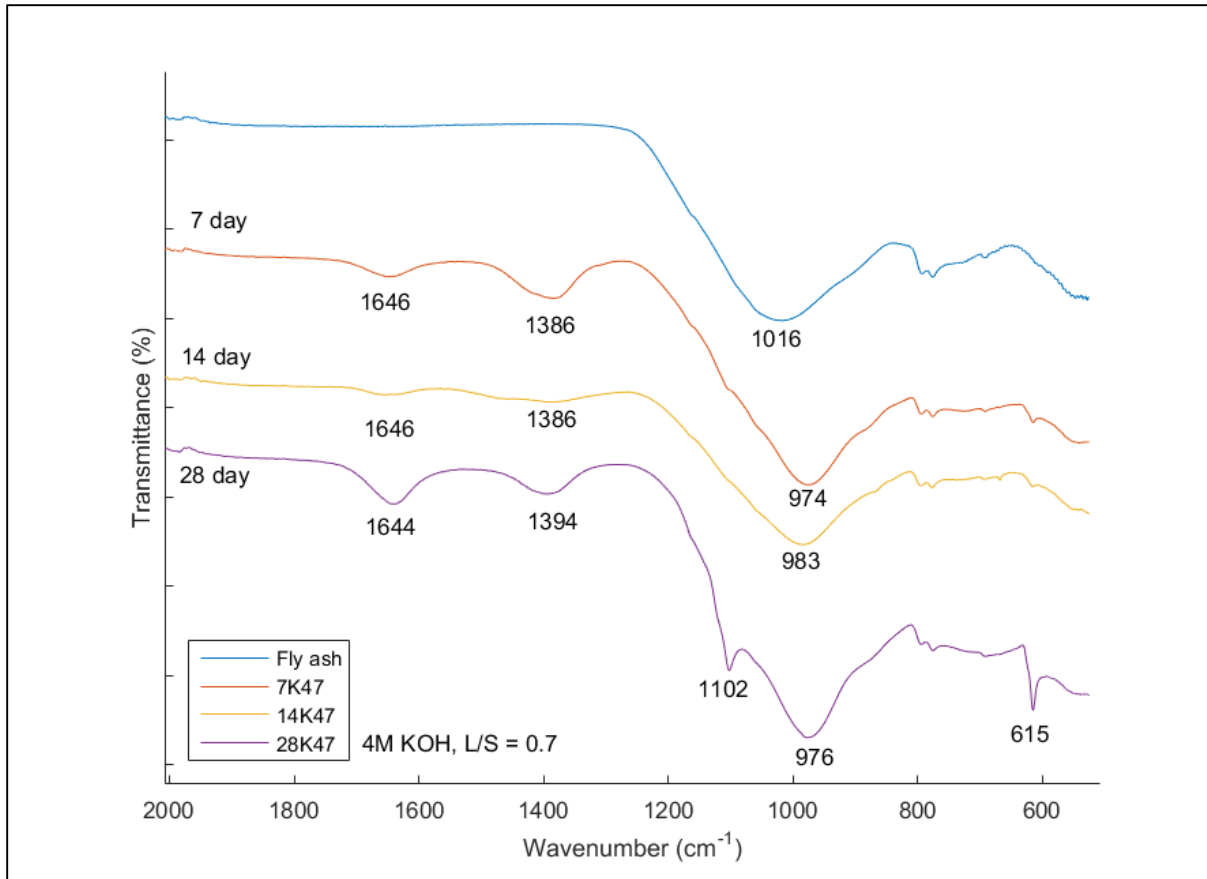


Figure 44. Fly ash geopolymer evolution of with time zoomed in

A magnified look of the same spectra as discussed before can be seen in Figure 44. The prominent peaks have the wavenumber below them at their lowest transmittance value. Compared to the unreacted fly ash, all of the samples developed peaks at $\sim 1646\text{ cm}^{-1}$ and $\sim 1390\text{ cm}^{-1}$. The band at 1645 cm^{-1} is attributed to stretching vibrations of water molecules. The other band at $\sim 1390\text{ cm}^{-1}$ is a sign of O-C-O stretching vibration from carbonate groups. Not surprisingly, the 14-day sample, which contained the least amount of adsorbed water, has an almost unnoticeable peak at 1646 cm^{-1} , but the carbonate stretching vibration that appears in the other samples is absent from the 14-day sample. A reason for this could be that the 14-day sample was more part of the bulk and less of the surface layer, which could explain why there are no carbonation bonds present. The 28-day sample also developed a small peak at 1102 cm^{-1} and at 615 cm^{-1} , which can be barely seen in the other spectra. The former peak can also be found in Portland cement and it is a fingerprint of ettringite, a calcium-aluminum-silicate mineral, which is an unexpected finding, considering the low calcium content of fly ash. It is not unreasonable however, because the small amount of sample measured could have contained local surplus of calcium ions, facilitating the crystallization of ettringite. The other band at 615 cm^{-1} is characteristic of Al-O stretching vibrations of AlO_4 groups, which can also be seen in the other geopolymer spectra although to a much lesser extent.

Figure 45 shows the IR spectra for samples prepared from Portland cement and fly ash in a 1:1 mix ratio by weight with unreacted Portland cement as a reference. The figure shows the same

trends and peaks as discussed in the last figure. There is a large and narrowing peak of T-O-Si at $\sim 950\text{ cm}^{-1}$, where T is Al or Si. The presence of water can also be detected in a broad peak from 3500 to 3000 cm^{-1} .

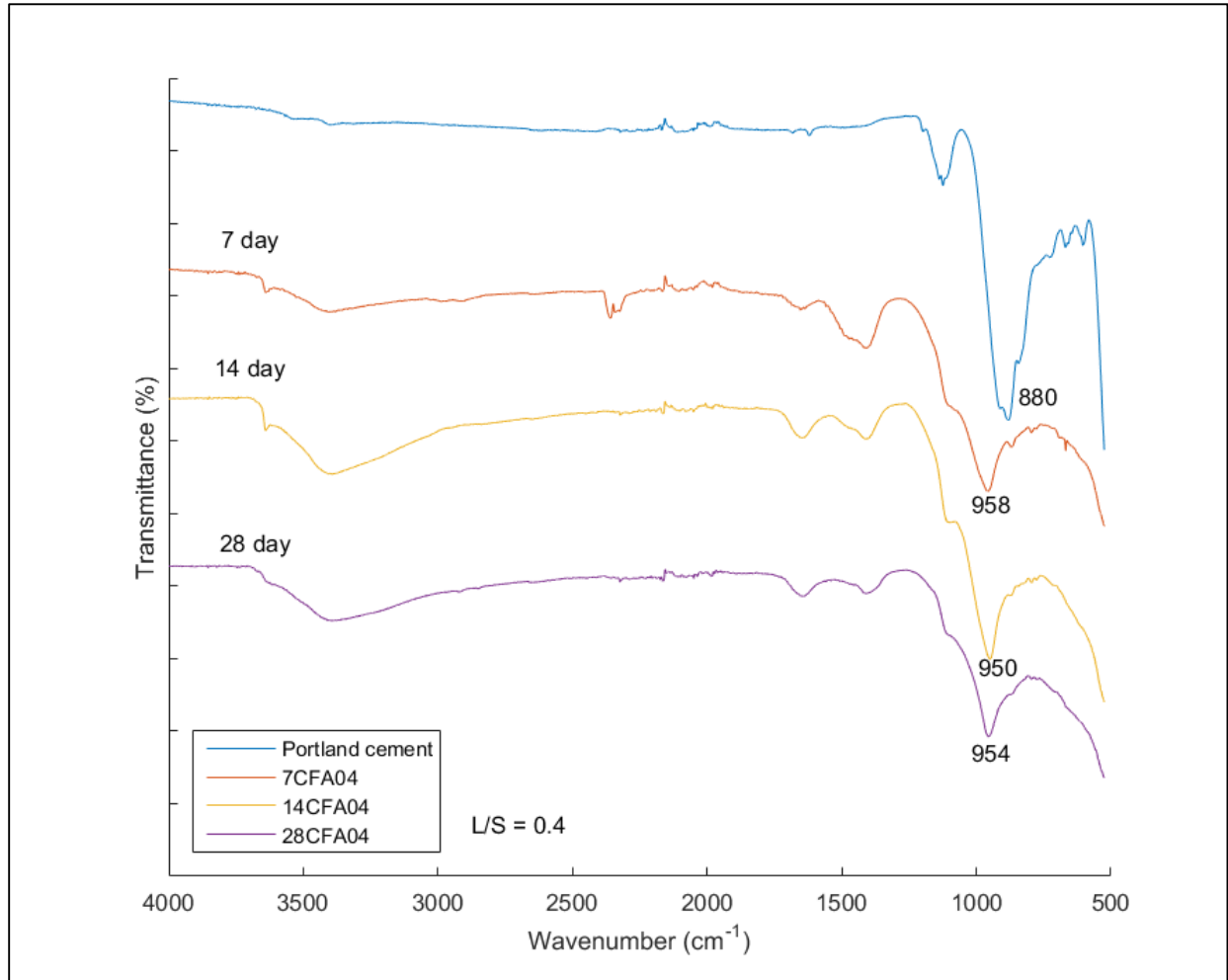


Figure 45. IR spectra of fly ash and PC mixture curing with respect to time

A closer look on the spectra is shown in Figure 46. The same peaks for carbonates and water (~ 1647 and $\sim 1410\text{ cm}^{-1}$) can be observed with no significant changes with respect to time. Some evolution of the T-O-Si peaks can be observed as a function of time, the broad peak gets narrower and sharper as time progresses. Another small shoulder peak is seen at $\sim 1100\text{ cm}^{-1}$ which is attributed to ettringite, which was already present in the Portland cement so it is worth mentioning that it is still present in the sample.

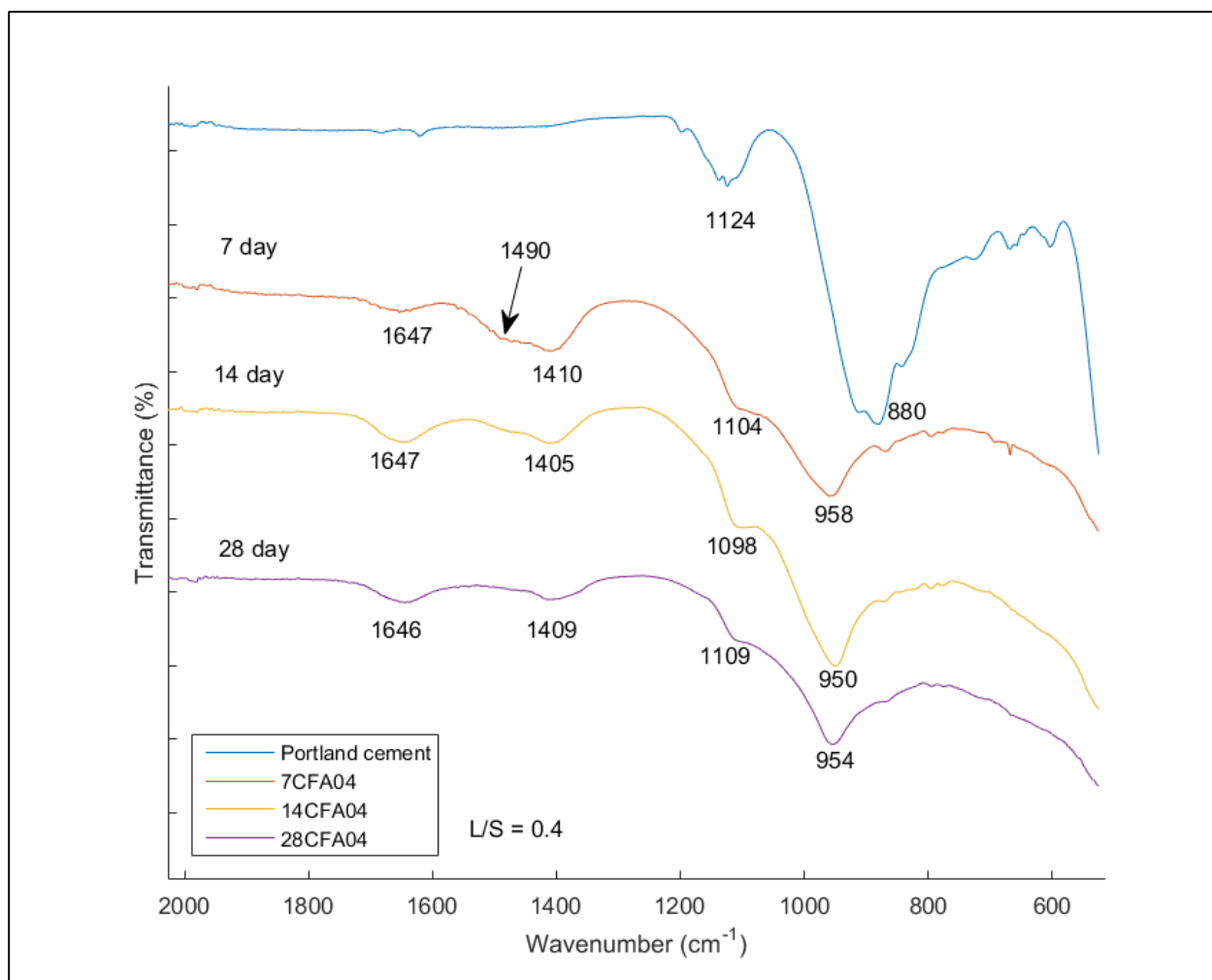


Figure 46. IR spectra of fly ash and PC mixture curing from 525-2000 cm^{-1}

The spectra shown in Figure 47 were recorded for the PC and fly ash samples with different L/S ratios that were left to cure for 7 days. The main bands are the same as in the previous cases and they look almost identical. Upon further examination, it can be observed that the shoulder, which represents ettringite at $\sim 1100 \text{ cm}^{-1}$ is more protruding in the case of larger liquid/solid ratio which means the sample with the larger initial water content has more ettringite. This can be seen in Figure 48.

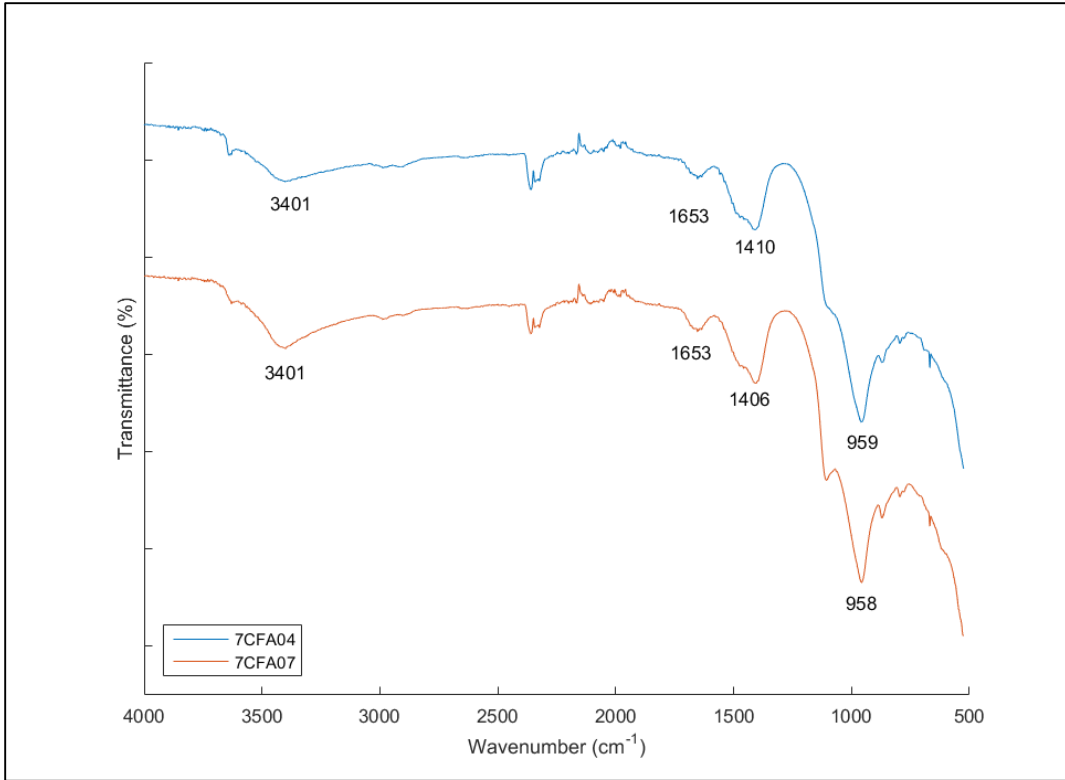


Figure 47. IR spectra of fly ash and PC blend comparison

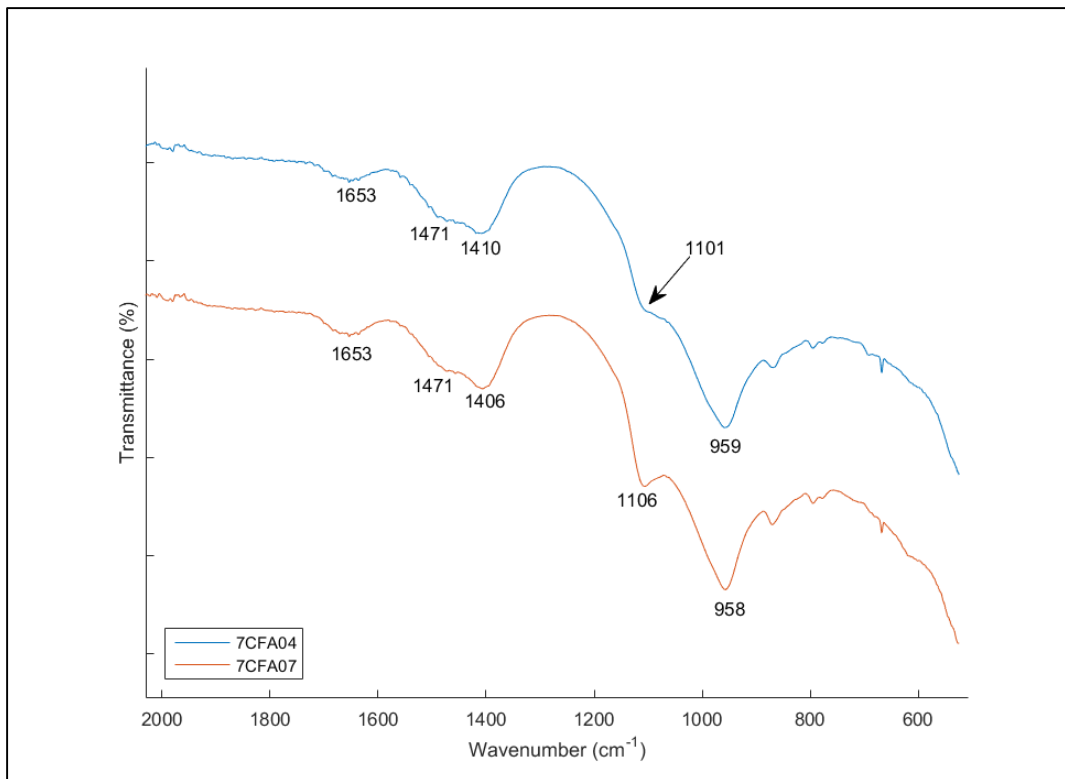


Figure 48. IR spectra of fly ash and PC blend comparison 2000-500 cm⁻¹

4. DSC

4.1. DSC theory

This method consists in measuring a sample and a reference heated at the same rate, increasing the temperature in a fixed amount, i.e. 20 °C/min, and then compare the difference of heat flow required to keep heating the samples at the same rate. If there is an endothermic process, energy will be absorbed and a difference represented as an upward peak will appear, if the process is exothermic the peak will point downward [37].

This definition is similar to the one from DTA (differential thermal analysis), but in DSC the sample and the reference are placed in different containers. On Figure 49 some of the common terms used in DSC and how are they represented in the experimental curves is shown [37]:

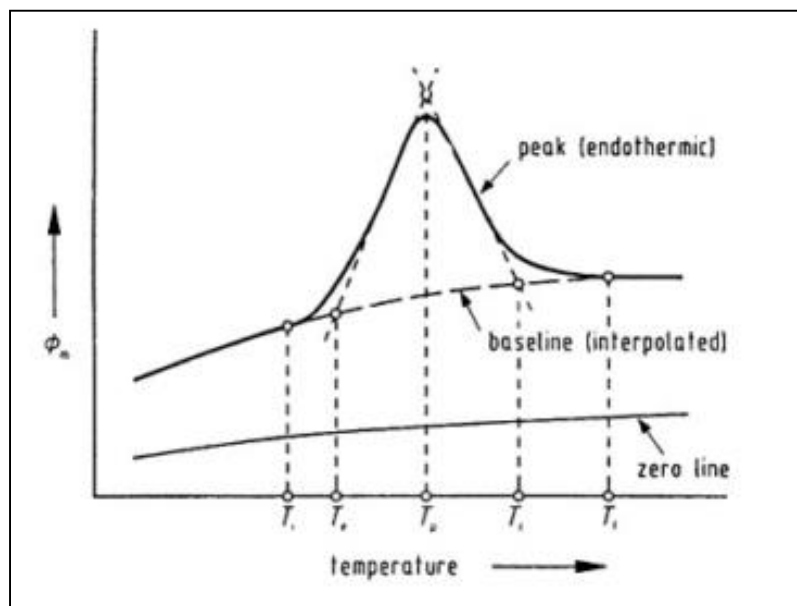


Figure 49. Usual DSC curve with an endothermic peak [37]

Where,

Zero line: is the measurement generated with no sample, meaning with the container that is called crucible.

Baseline: is the line that connects all the curves of the sample, even before and after each peak.

Peak: is the curve that appears over or below the baseline. In this case, it is an endothermic peak because it is absorbing energy.

Φ: refers to the heat flow

The remaining terms refers to the different temperatures that are present for each peak [37]:

T_i for the initial peak temperature,

T_e , for the extrapolated peak onset temperature

T_p , is the maximum temperature reach in the peak

T_c , is the extrapolated peak completion temperature

T_f , is the final peak temperature

Usually with DSC besides getting the fingerprint from a specific material, more information can be extracted like the occurrence on different events.

One of the measurements that can be obtained is the heat capacity, C_p , as this value is really important to determine other thermodynamic values like enthalpy, entropy and the free Gibbs energy [37]:

$$\Delta H = \int_{T_1}^{T_2} C_p dT \quad (5)$$

$$\Delta S = \int_{T_1}^{T_2} \frac{C_p}{T} dT \quad (6)$$

$$\Delta G = \Delta H - T\Delta S \quad (7)$$

Where,

C_p : the heat capacity at constant pressure

T_2, T_1 : temperature at the end and at the beginning, respectively

ΔH : difference on enthalpy during the process

ΔS : difference on the entropy

ΔG : defense on the free Gibbs energy

When an experiment is running, the DSC will have a baseline and all the peaks above that line will be the known as displacement or h , which in turn will be proportional to C_p and it can be calculated using the next equation [37]:

$$h = B\beta C_p \quad (8)$$

Where,

h: displacement of the DSC baseline

B: calibration factor

β : heating rate at the moment of the experiment

However, even though the process looks simple enough, it is recommended to do it with the most care in order to have precise results and good repeatability. The main task during this estimation would be to determine a good baseline for doing these calculations with the best values possible. When the DSC experiment is taking place and a peak appears, that is called a thermal event and after it occurs, the baseline will not be located at the same height before the peak if the thermal properties changed. Different types of baselines during a thermal event are shown on Figure 50.

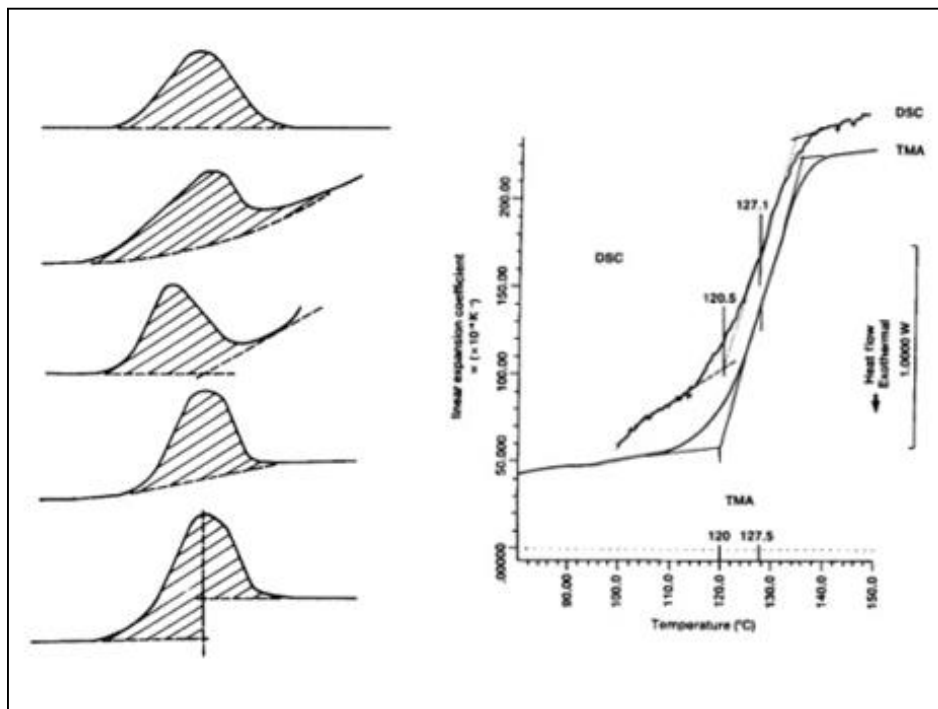


Figure 50. On the left side some of the different shapes a baseline can take and on the right side a glass transition phase [37]

The glass transition on the DSC can be detected when there is a sudden change on the baseline like the one shown on the right side of Figure 50, and it is because the heat capacity changed then the material phase suffered a transition from glassy to rubber-like and it is important to say that there is not enthalpy change during that transition because it is not thermodynamic but time dependent [37].

Another of the measuring that can be done with DSC are enthalpy changes, which is the area of the endothermic or exothermic peaks, and one of the ways to calculate that value is with the next equation:

$$\Delta H = A \frac{K}{m} \quad (9)$$

Where,

ΔH : enthalpy change

A: the area of the peak

K: calibration factor

m: mass of the sample

Usually with DSC and DTA are used to fingerprint samples, but usually can be used also to study different thermal events from the peaks as explained before, so Figure 24 shows the DSC taken from a sample of $\text{CuSO}_4 \cdot 5\text{H}_2\text{O}$ [37]:

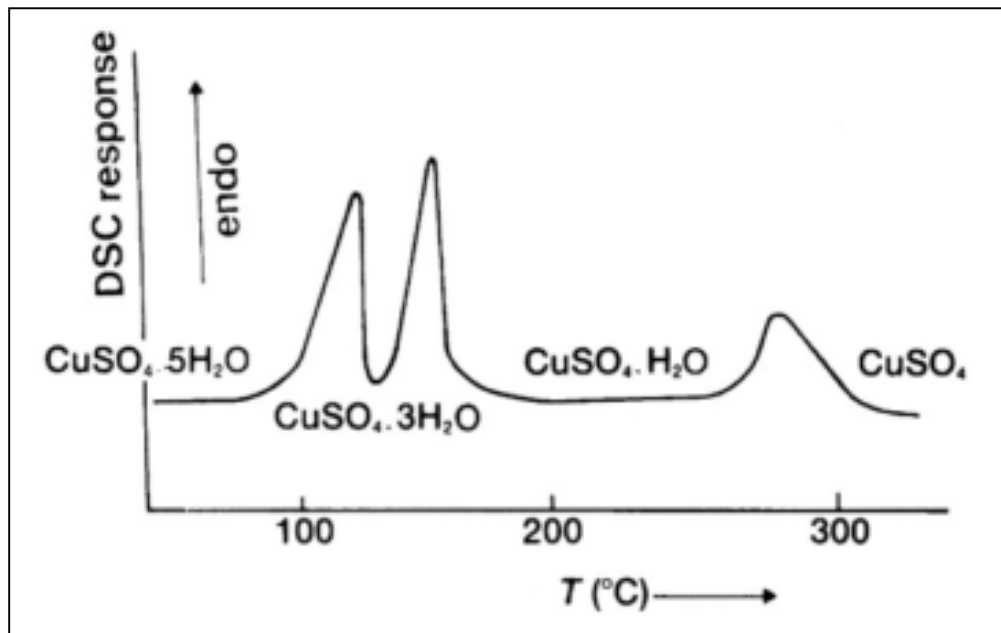


Figure 51. Typical layout of a DSC experiment [37]

From the figure, it can be observed how appear the endothermic peaks that represent the water extraction from $\text{CuSO}_4 \cdot 5\text{H}_2\text{O}$ to CuSO_4 , and these are called enthalpy of dehydration. The shape of these peaks can be used to calculate the purity of CuSO_4

Summarizing, DSC peaks and shape can be used to study different properties from polymers, as it is shown in Figure 52 for an organic polymer. A number of phase changes can be observed, starting from the glass transition, which is marked with the change of the heat capacity but with no peak showing any enthalpy.

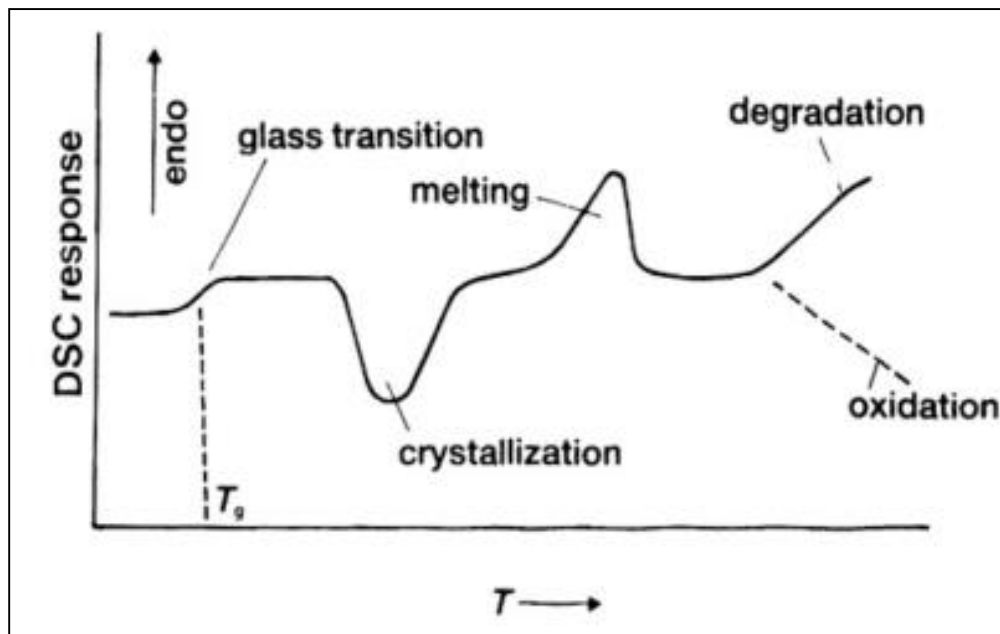


Figure 52. DSC of a typical polymer [37]

The phase change from glass to rubber, also called glass transition, is represented as a discontinuity of the original baseline because of the change from glass to rubber and the temperature at which it happens is called T_g [37].

If the temperature continues increasing the material can go back to recrystallize and this phase change will also show another peak but as an exothermic event, which will continue later on to the melting point, and the event here would be an endothermic event. If the process continues increasing the temperature the polymer may go to degradation or oxidation, depending on the atmosphere that is been used in the DSC experiment (nitrogen, air or oxygen).

4.2. What has been done

On [38] two types of samples were measured: a sample A of fly ash from China and sample B of fly ash from France. Both samples were melted using a DSC and both samples yield the typical DSC and DTA analysis that is shown in figure 33 done at a fixed heating rate of 10 °C/min from 0 C to around 1400 °C [38].

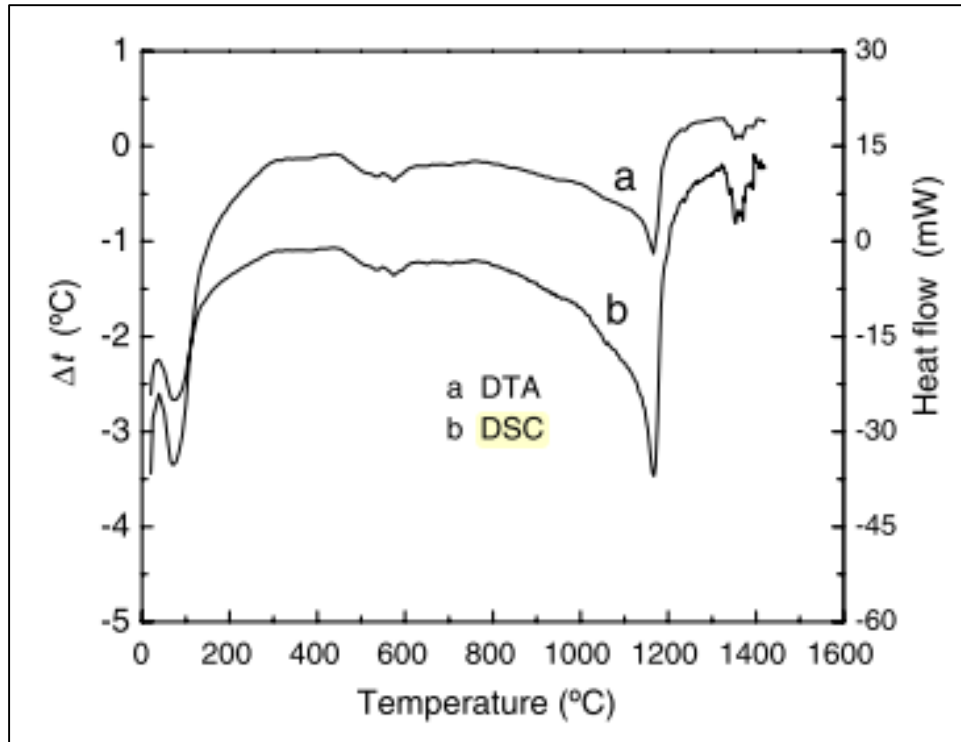


Figure 53. Typical DSC of a fly ash melting [38]

Figure 53 shows sample A in oxygen atmosphere during both of the tests and from the curve it can be observed the whole endothermic process separated in three stages:

1. The first peaks below 200 °C was assumed to be related to the evaporation of water or moisture present in the fly ash.
2. The second peak between the range of 480 to 670 °C was believed to represent the polymorphic transition
3. The thirds and last stage is related to the fusion of the fly ash, this occurrence takes place between 1101 C and 1244 °C.

From this results the author proposed the following phases that occur during the melting of fly ash using DSC and DTA studies and this is shown in Figure 54.

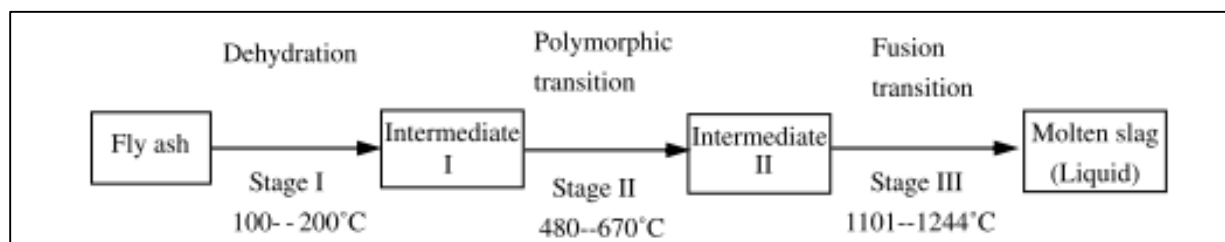


Figure 54. Schematic of the typical melting process of fly ash [38]

The whole set of samples are described on a table in the appendix and after the experiments were done, they calculate the enthalpy of the endothermic process for the different samples. With those results and using the equation explained in the theoretical part, they proceed to estimate the plot for calculate the kinetic parameters as shown in Figure 55:

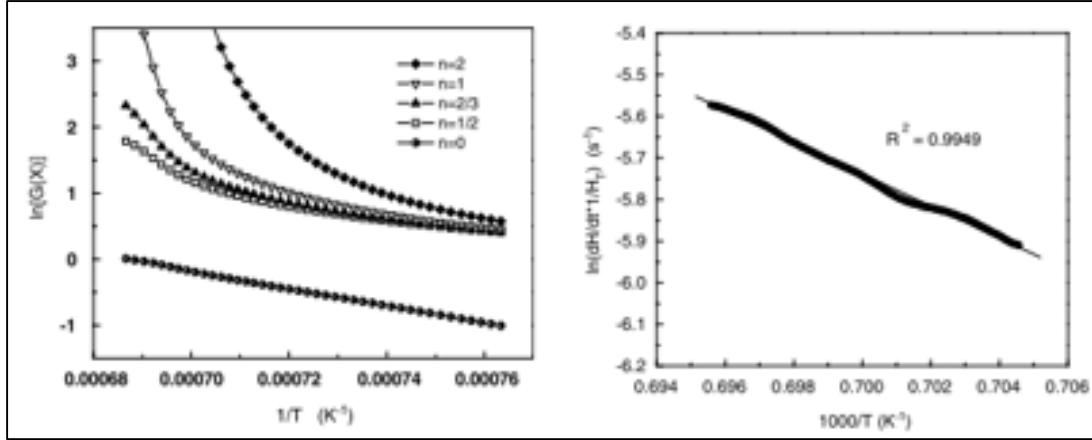


Figure 55. On the left plot for the ln G against 1/T. On the right the ln (dH) *1/H against 1/T [38]

The plot from the right side on figure 35 was done to simulate one of the forms of the Arrhenius equation.

$$\ln\left(\frac{1}{H_\tau} \frac{dH}{d\tau}\right) = \ln A - \frac{E}{RT} \quad (10)$$

Where, H: experimental enthalpy calculated using the software from the DSC.

E, A: kinetic parameters

T: temperature

R:

Table 9. Kinetic parameters of the fly ash [38]

Experimental run no.	Characteristic temperature		Kinetic parameters	
	Temperature range (°C)	Peak temperature (°C)	Activation energy E (kJ mol ⁻¹)	Pre-exp A (s ⁻¹)
1	1124.0–1184.9	1164.50	90.23	23.855
2	1130.6–1250.7	1079.76	600.85	7.83E+18
3	1127.5–1175.5	1160.07	133.29	165.12
4	1130.0–1184.5	1168.37	319.36	1.53E+09
5	1135.1–1200.4	1178.28	526.01	2.79E+16
6	1167.6–1228.2	1205.42	114.06	55.37
7	1324.5–1402.9	1266.35	68.82	2.858
8	918–975.9	952.35	138.35	2.81E+06

It is important to note that this paper took out the results from 25 to 200 °C because that was considered part of dehydration part and they didn't consider it pertinent for the calculations of the pure fly ash behavior. Another point to take into consideration is that the calorimetry machine they used could reach temperatures over 600 °C so they managed to reach the fusion stage of the fly ash.

On the study performed at [39] the DSC was performed in geopolymers created from fly ash as a binder and water and the results can be seen on Figure 56.

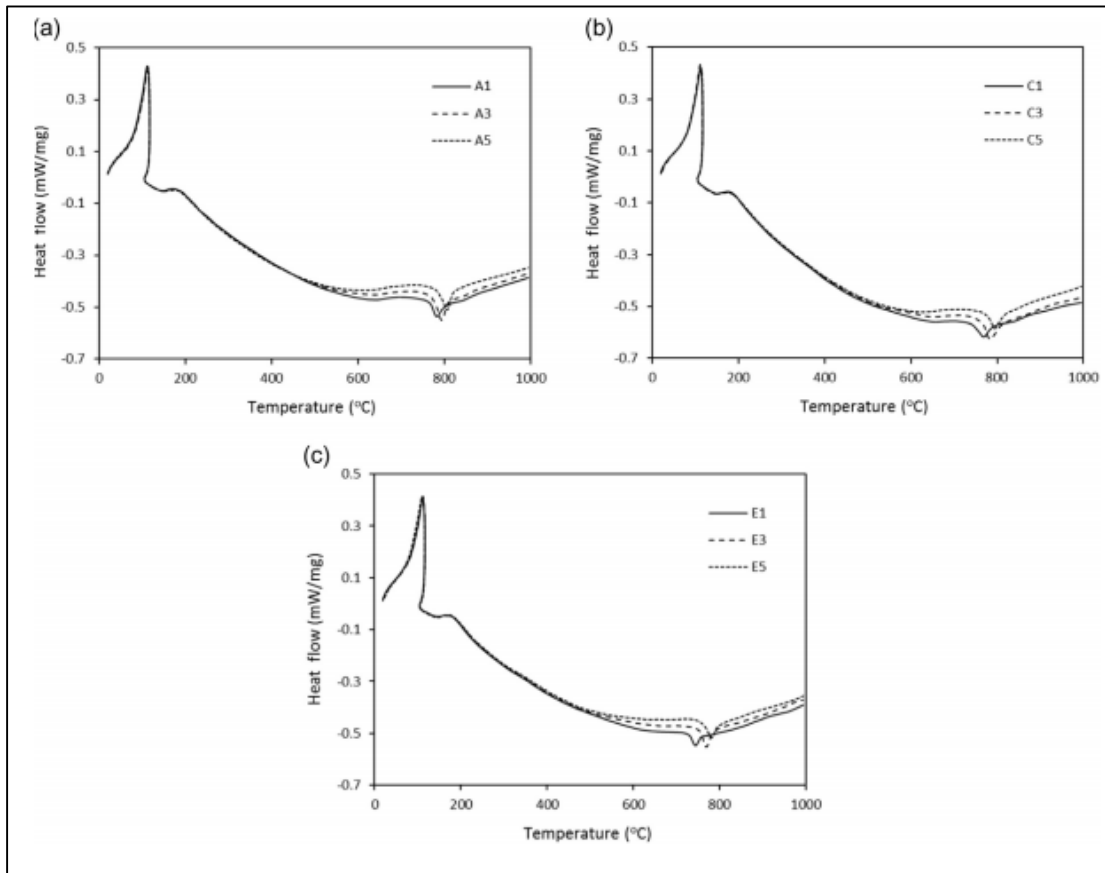


Figure 56. DSC analysis performed for three different samples of fly ash with activator moduli of 1,8 ; 1,4 and 1,0 [39]

From the plots it can be observed that in all the analysis there was a heat absorption peak around 100 °C which is associated to water evaporation, just like the case of figure 35 for the melting of pure fly ash. The peak in this case should be higher because the amount of water in these experiments is bigger; on [38] the water evaporated was the remaining moisture from the pure fly ash but in the case of [39] the water is an addition done to the sample in order to create the geopolymer.

Around 180 and 200 °C there is the appearance of a broad and small peak that is usually associated with the decomposition of hydrated gels and that gel structure experience changes that

are related to gel deterioration [39]. In all the case, no matter in what initial conditions the samples were created, the deterioration temperature appears always around the same temperature [39].

Around 800 °C, all the samples shown a peak that represents an exothermic stage and it is associated to the formation of crystals [39]. This behavior similar to the one initiated because of the loose of water in C-A-S-H type gels, followed by the destruction of the gels and appearance of crystals [39].

4.3. Results and analysis

The calorimetry tests were done using a Mettler Toledo DSC822e equipped with an autosampler with a heating rate of 20 °C/min. The samples measured are shown in the next table, just like the ones with the Raman and IR machine.

Table 10. Samples used for the DSC experiments

Sample	Alkaline solution	Concentration of alkaline solution (M)	L/S ratio	Mass alkaline solution (g)	Mass water glass (g)	Mass of solids (g)	Mass of water (g)
0K44	KOH	4	0,4	8,77	8,76	43,76	N / A
0K47	KOH	4	0,7	8,78	8,78	25,01	N / A
0K64	KOH	6	0,4	8,77	8,76	43,75	N / A
0K67	KOH	6	0,7	8,77	8,77	25,04	N / A
0CF04	KOH	4	0,4	N / A	N / A	21,88	17,50
0CF07	KOH	4	0,7	N / A	N / A	12,52	17,49
0C04	KOH	4	0,4	N / A	N / A	43,75	17,50
0C07	KOH	4	0,7	N / A	N / A	25,03	10,01

The DSC machine used can be observed on figure 58, and the model is:



Figure 57. DSC machine with autosampler used for the experiments

Figure 58 shows the press that was used to close the crucible, which are also in the figure bottom right side.



Figure 58. Press used to seal crucibles

Figure 59 shows the section where the crucible are placed.



Figure 59. Sampler plate on the DSC apparatus

The procedure for measuring the samples is taking small amounts, crush them, place the sample in small aluminum containers with a volume of 40 μl -s, which are called crucibles. The samples usually weighed between 4 and 10 mg. A container is placed on the first position that is marked as 101 and after that all the remaining crucibles measured are placed in the following positions starting from 102.

Once the samples were ready, the next step was select a program for the measuring, select the heating rate, input the mass measured for the sample and run the experiment. The heating rate selected for all the samples was of 20 $^{\circ}\text{C}/\text{min}$ and it was done between 25 $^{\circ}\text{C}$ and 550 $^{\circ}\text{C}$.

Most of the DSC plots were place in the appendix and only a few selected were chosen in order to do the comparison. Figure 60 shows the DSC taken for sample K44 for the slurry (blue line), 7 days of curing (red line) and 14 days of curing (yellow line).

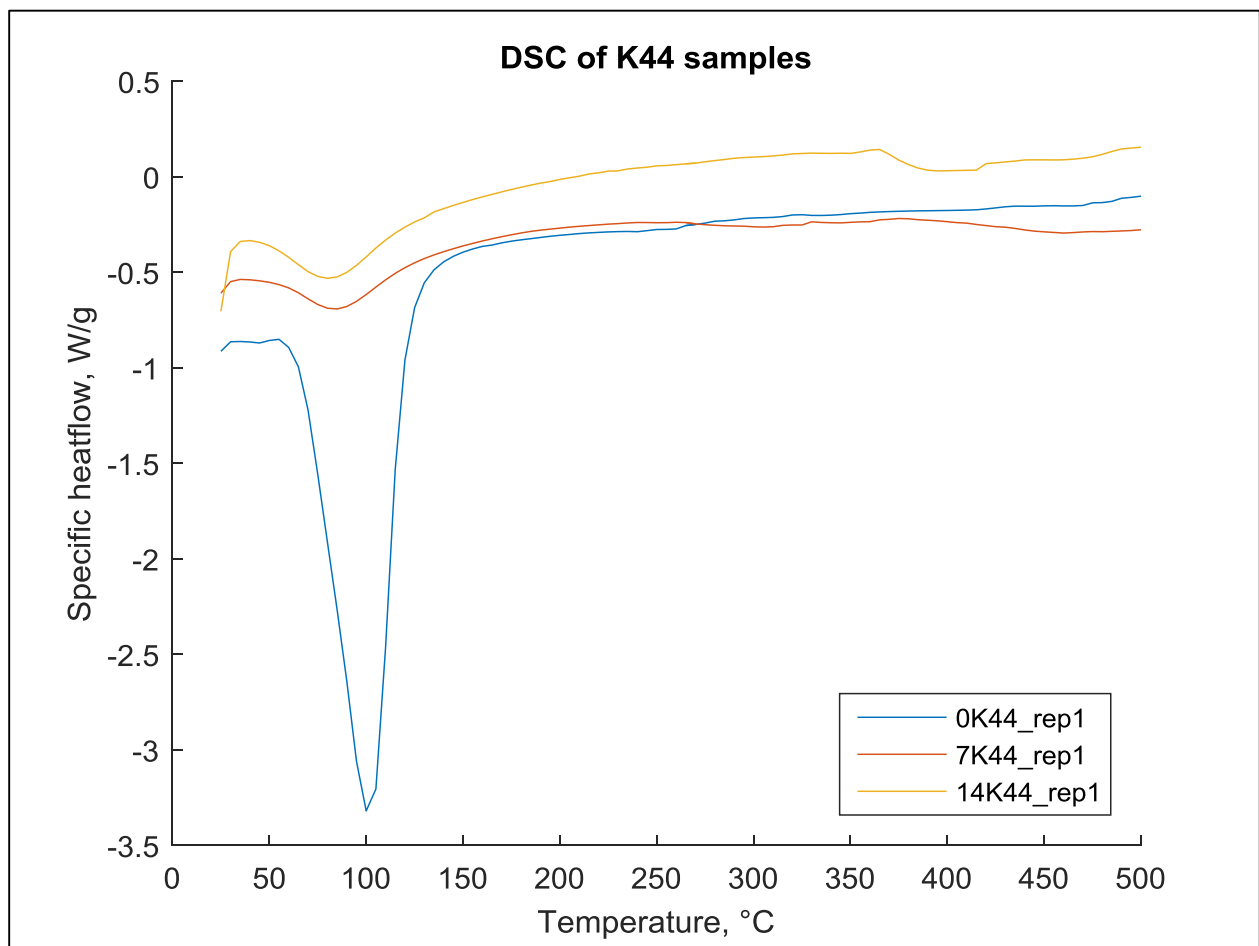


Figure 60. DSC for the sample K44.

The bigger peak is present only in the slurry line around 100 $^{\circ}\text{C}$ and it should represent the dehydration of the sample from the fresh formed mixture, so that is why the exothermic peak is bigger than the other ones for 7 and 14 days of curing.

The peak of dehydration around 100 °C can also be seen for the other lines but they are smaller because the dehydration had already taken place to a certain extent so there is less water to evaporate. Because the DSC can only go up to 550 °C, the peaks that are supposed to appear after 600 °C cannot be studied.

On Figure 61, the DSC was taken also for sample K67 and for the slurry, 7 days and 14 days of curing.

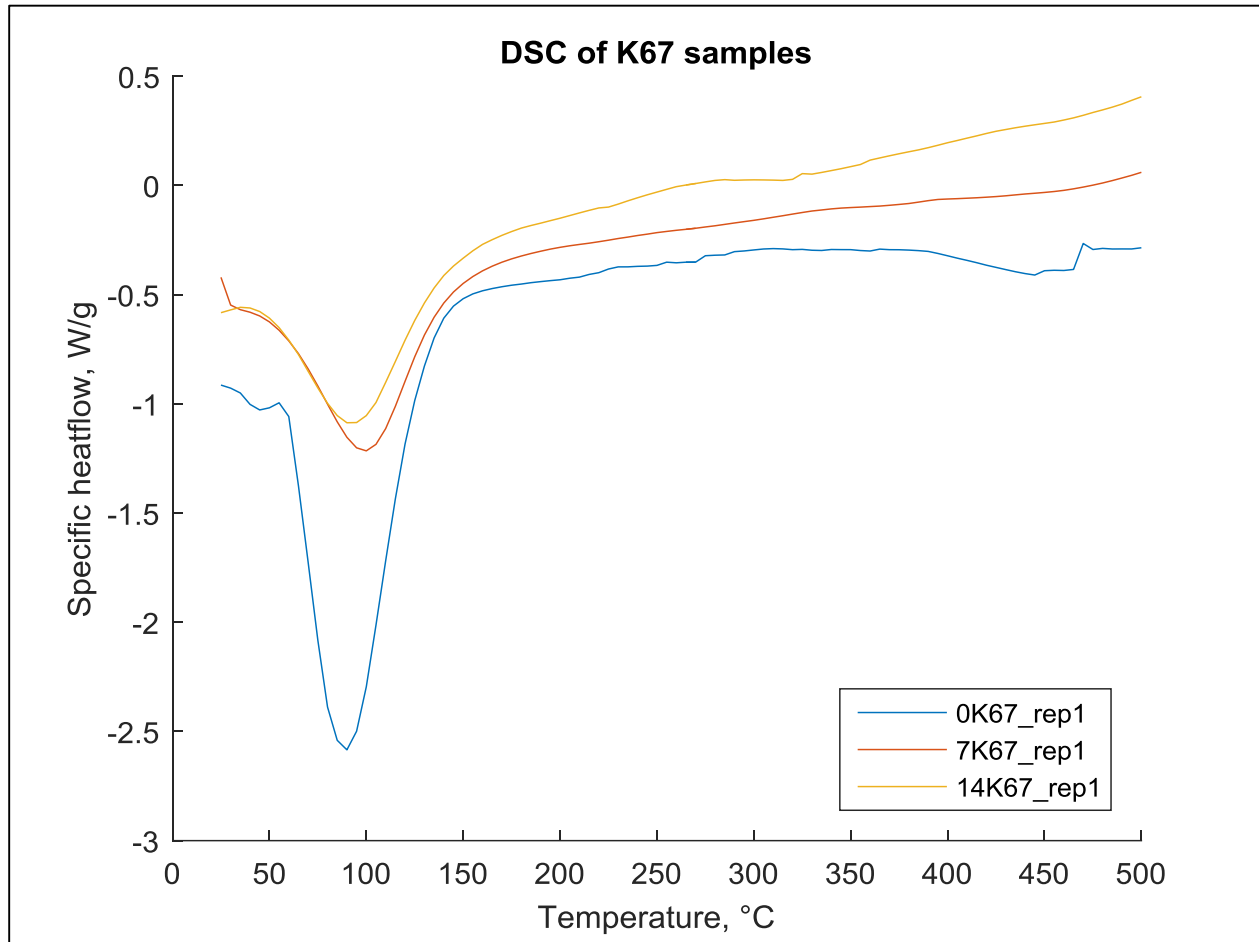


Figure 61. DSC for the sample K67.

Just like with the DSC taken for sample K44, the big peak for the slurry that represents the water evaporating is shown in the slurry line. In this plot it can be seen more clearly how the dehydration peak gets smaller while the curing takes place, meaning the water that will evaporate after 14 days was less than the evaporated at 7 days and so on.

Figure 62 that shows the DSC taken for a sample of 50% fly ash and 50% of cement, the same behavior can be observed as the previous figure.

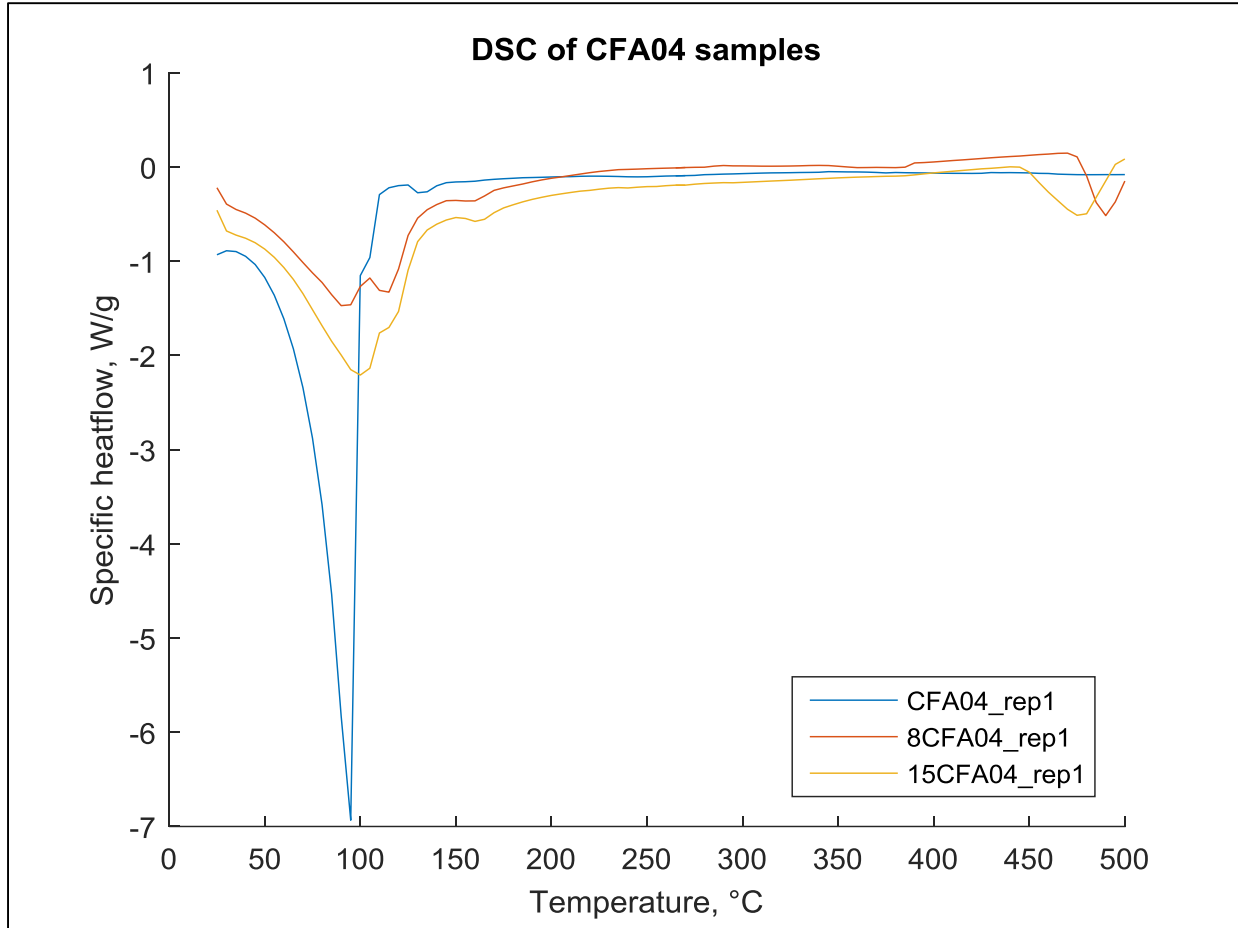


Figure 62. DSC for the sample CFA04

The problem with the results obtained from all the DSC plots was the lack of any important peak beside the endothermic one around 100 °C which represents the evaporation of water and is should not be used for the calculation of the curing. It was not possible to study the peaks that should appear at 800 °C because the machine can only reach until 550 °C.

5. XRD

5.1. Theoretical background

As explained before, depending on the range of the spectrum one wish to studied a different method for measuring would be necessary. In this case X-rays refer to the radiation located between 10⁻³ nm to 10 nm, and the zone for measuring materials is located between 0,1 and 0,2 nm, called hard x-rays [40]; the rest of the X-ray range is used for radiography, tomography, etc.

Some of the measuring that can be done using x-rays would be crystal structure, phase transition, crystalline quality, orientation and internal stress [40]. On Figure 63 a typical schematic for XRD is shown:

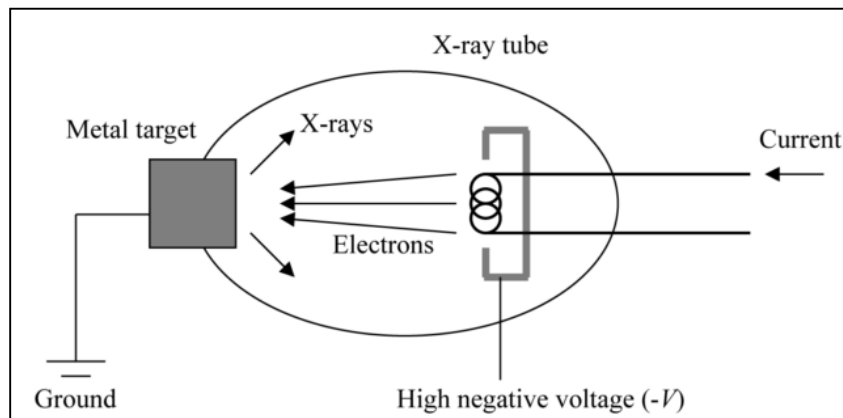


Figure 63. Theory behind an XRD machine [40]

High electrical current will accelerate electrons from the X-ray source and it will collide with the sample to analyze, which will be impact by one of the many beams that are been shot [40]. The Kinect energy of the electrons that will hit the target can be calculated with the next equation:

$$KE = \frac{1}{2}mv^2 = eV = h\frac{c}{\lambda_{min}} \quad (11)$$

Where,

m: mass of the electron

v: speed at the moment of impact

V: high voltage

c: speed light

λ_{min} : shortest wavelength

However, it is important to know that this is the energy calculated when all the energy from the electron is converted to energy from the photon, but this will not take place because the collisions the electrons will suffer generates losses [40], meaning the transferred energy will be less than $h\nu_{max}$. The parts that form part of a typical diffractometer are shown in Figure 64, which are the X-ray source, the sample holder and the detector of the refracted X-rays [40].

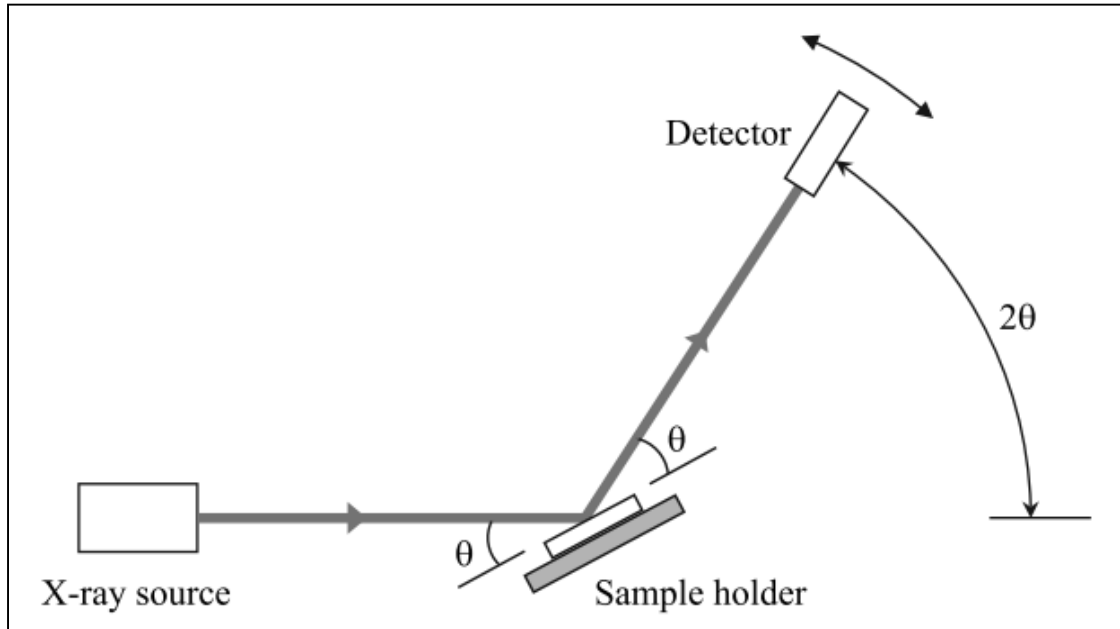


Figure 64. Typical components in a diffractometer [40]

A beam is shot from the X-ray source and this will hit the sample that is on the holder. After hitting the sample, the beam will lose a certain amount of intensity and that value will be measured by the detector. The angle from the incident beam with the holder and the diffracted beam that is going to the detector from the holder must be equal to θ and with this, the next equation known as Bragg law can be used:

$$\lambda = 2d\sin\theta \quad (12)$$

Where,

λ : wavelength

d : interplanar distance

θ : incidence angle of the beam from the X-ray source

Figure 65 shows the bremsstrahlung obtained from molybdenum where it can be seen how the more potential difference it employed, the intensity will also increase. The λ_{\min} will be decreasing in length and this value can be calculated using equation 11 [40].

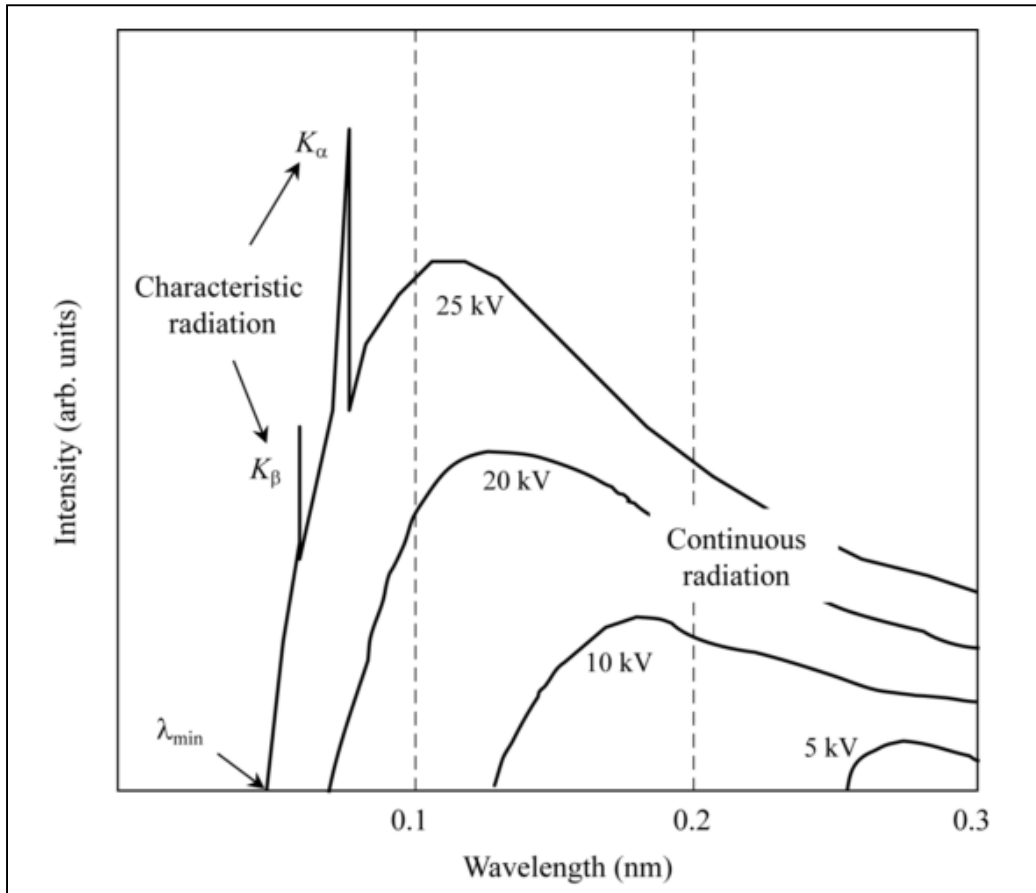


Figure 65. Typical X-ray emission from a molybdenum target [40]

From Figure 65 it can be seen there are two types of radiation. The first one is the continuous radiation, which is related to the loss of KE from the electrons. The sharp peaks (K_{α} and K_{β}) are characteristic radiation which are related to the material and appear when an electron is ejected from an inner shell of the atom that is being bombarded with the electron beam.

5.2.Literature review

Figure 66 shows the XRD pattern of class F fly ash a geopolymer made with NaOH activator and fly ash. A few sharp peaks can be seen which correspond to quartz (Q) and kaolinite (K) phases. Quartz is structured SiO_2 and Kaolinite can be represented as $\text{Al}_2\text{Si}_2\text{O}_5(\text{OH})_4$. The broadening of the spectra from $18\text{-}36^\circ 2\Theta$ is a characteristic sign of amorphous geopolymers [41], [42]. The fly ash and the geopolymer show a very similar, but quite broad peak from $8\text{-}16^\circ 2\Theta$, which indicates a low degree of geopolymerization, which is a possible explanation to the low compressive strength and stiffness of samples made from fly ash and activators (without any Portland cement).

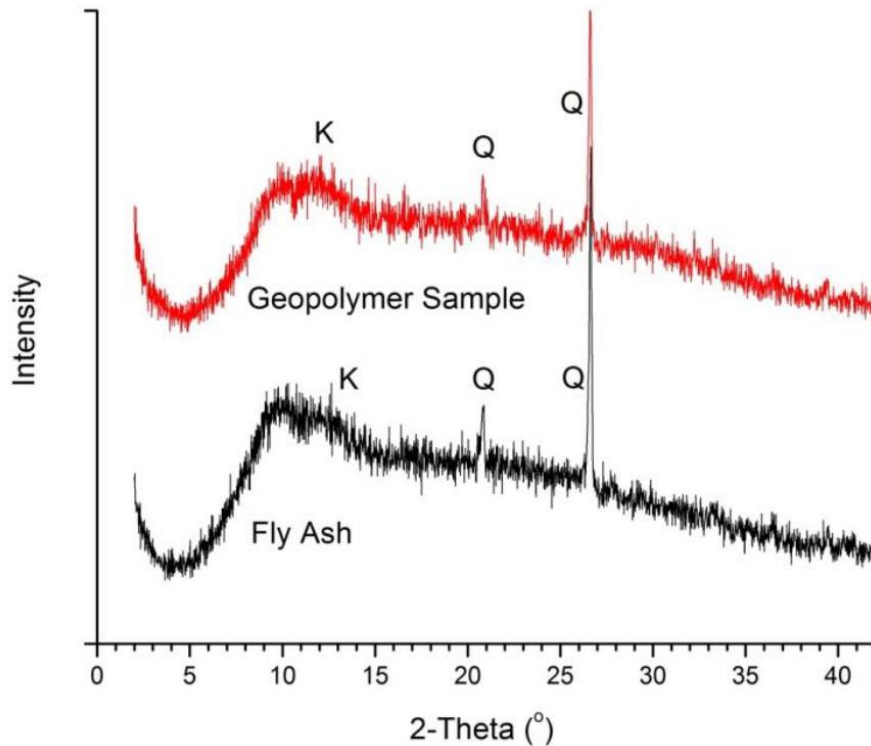


Figure 66. XRD pattern of class F fly ash and a geopolymer sample (Q = quartz, K = kaolinite) [43]

The XRD patterns for Ordinary Portland Cement (OPC) are shown in Figure 67. The cement pastes have been measured after letting them harden for 3, 28 and 180 days respectively. Compared to fly ash, OPC already has a significant amount of Ca-containing species, which are alite, belite, portlandite, calcite and CSH phases.

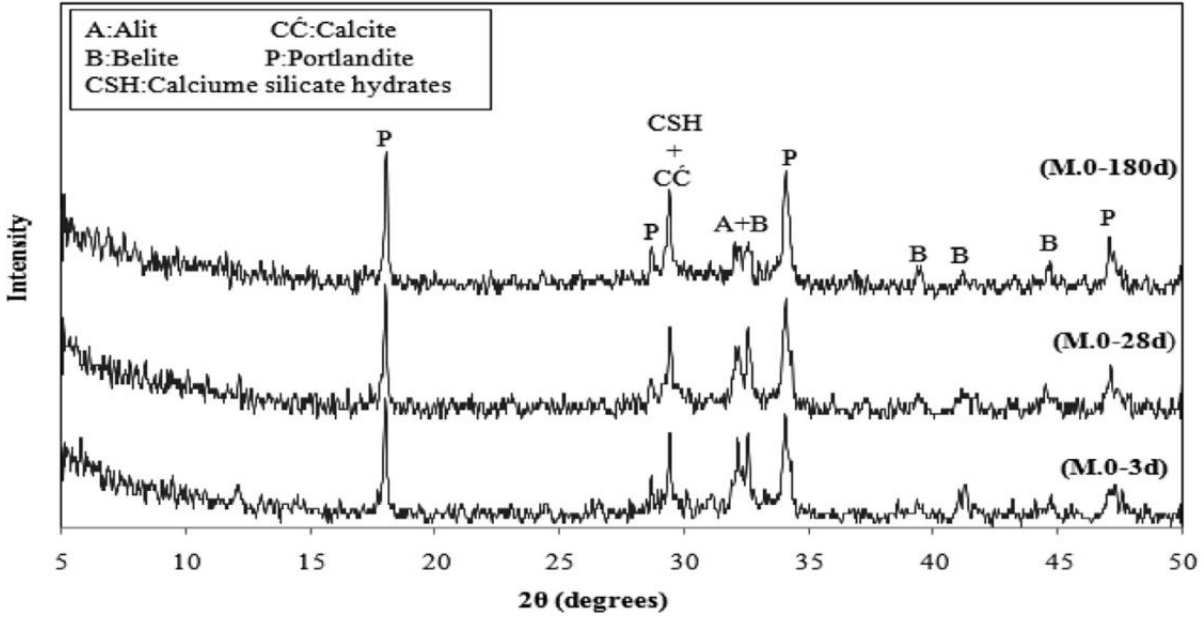


Figure 67. XRD diffractograms of Ordinary Portland Cement pastes after hydration times of 3, 28 and 180 days [44]

Figure 67 shows some typical phases, which can be found in Portland cement. The chemistry of cement is very complex in nature, which is why a shorthand form has been developed to represent chemical compounds that are often encountered. The usual abbreviations of primary components and phases are shown in Table 11 and Table 12.

Table 11. Shorthand for frequently encountered chemical formulas [12]

Chemical	Abbreviation
Al_2O_3	A
SiO_2	S
CaO	C
Fe_2O_3	F
H_2O	H
MgO	M
SO_3	\bar{S}

Table 12. Primary phases and compositions of OPC [1]

Mineral phase	Chemical name	Chemical formula	Abbreviation	Usual % of composition
Alite	Tricalcium silicate	$3 \text{ CaO} \cdot \text{SiO}_2$	C_3S	50-70 %
Belite	Dicalcium silicate	$2 \text{ CaO} \cdot \text{SiO}_2$	C_2S	15-30 %
Aluminate	Tricalcium aluminate	$3 \text{ CaO} \cdot \text{Al}_2\text{O}_3$	C_3A	5-10 %
Ferrite	Tetracalcium aluminoferrate	$4 \text{ CaO} \cdot \text{Al}_2\text{O}_3 \cdot \text{Fe}_2\text{O}_3$	C_4AF	5-15 %

5.3. Experiments and results

The XRD spectra were measured with were obtained using Co radiation ($k = 1.7889 \text{ \AA}^\circ$) with a Philips X'pert MPD reflection diffractometer.

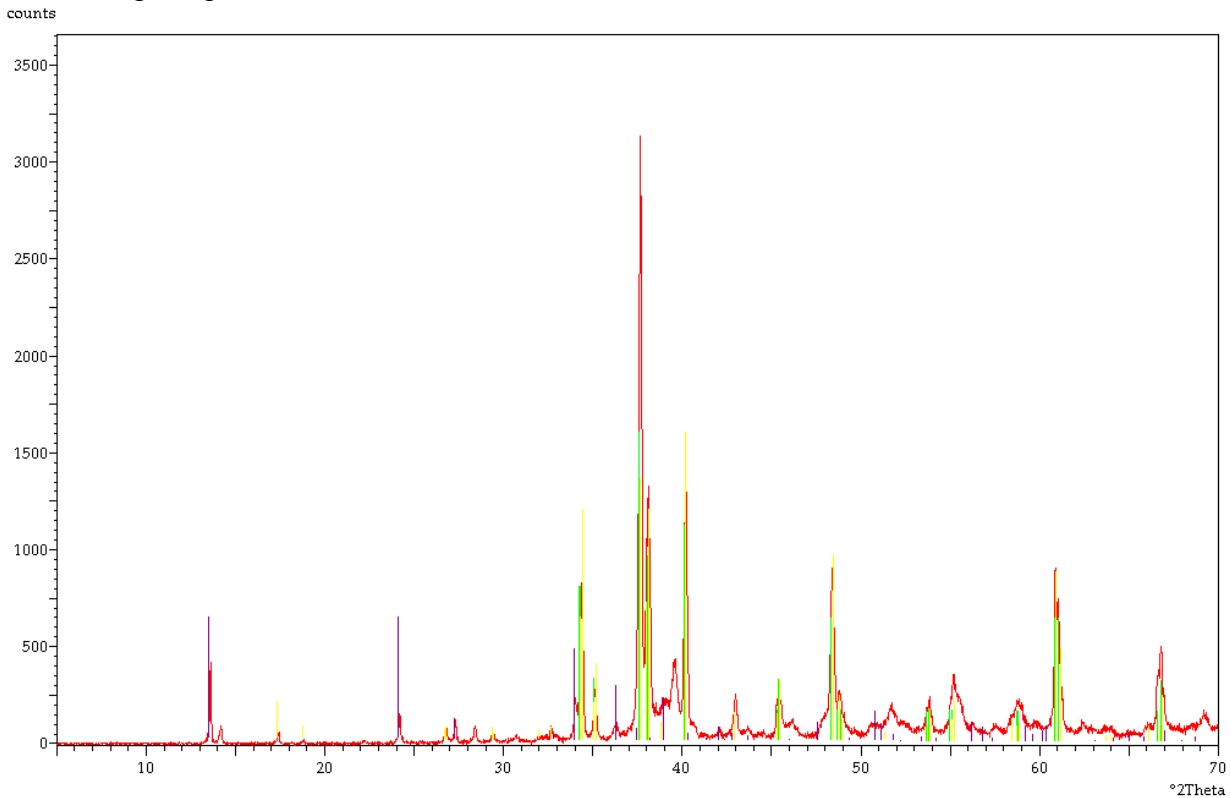


Figure 68. XRD of portland cement

The XRD pattern of unreacted Portland cement can be seen in Figure 68. The green lines on the graph represent a calcium-magnesium-aluminum-silicate complex, which according to search-match software has a formula of $\text{Ca}_{54}\text{MgAl}_2\text{Si}_{16}\text{O}_{90}$. The purple lines on the graph represent crystalline gypsum phase (G, $\text{CaSO}_4 \cdot 2 \text{H}_2\text{O}$). The yellow lines represent the Ca_3SiO_5 (C_3S) phase.

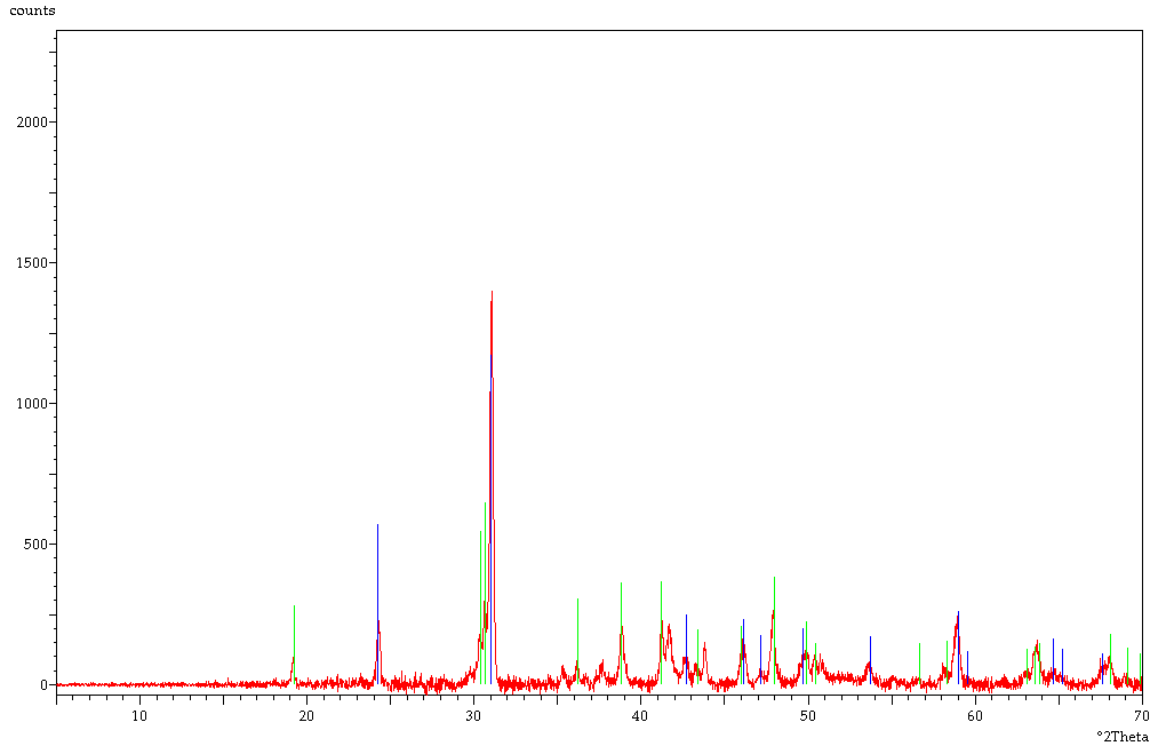


Figure 69. XRD of fly ash

Figure 69 shows the XRD pattern of class F fly ash before it was reacted. The blue lines represent quartz phases, while the green lines are identified as mullite (M, 3 Al₂O₃ 2 SiO₂). Although the phases themselves could not be identified by neither Raman- or IR-spectroscopy, the bonds appearing in mullite and quartz were found.

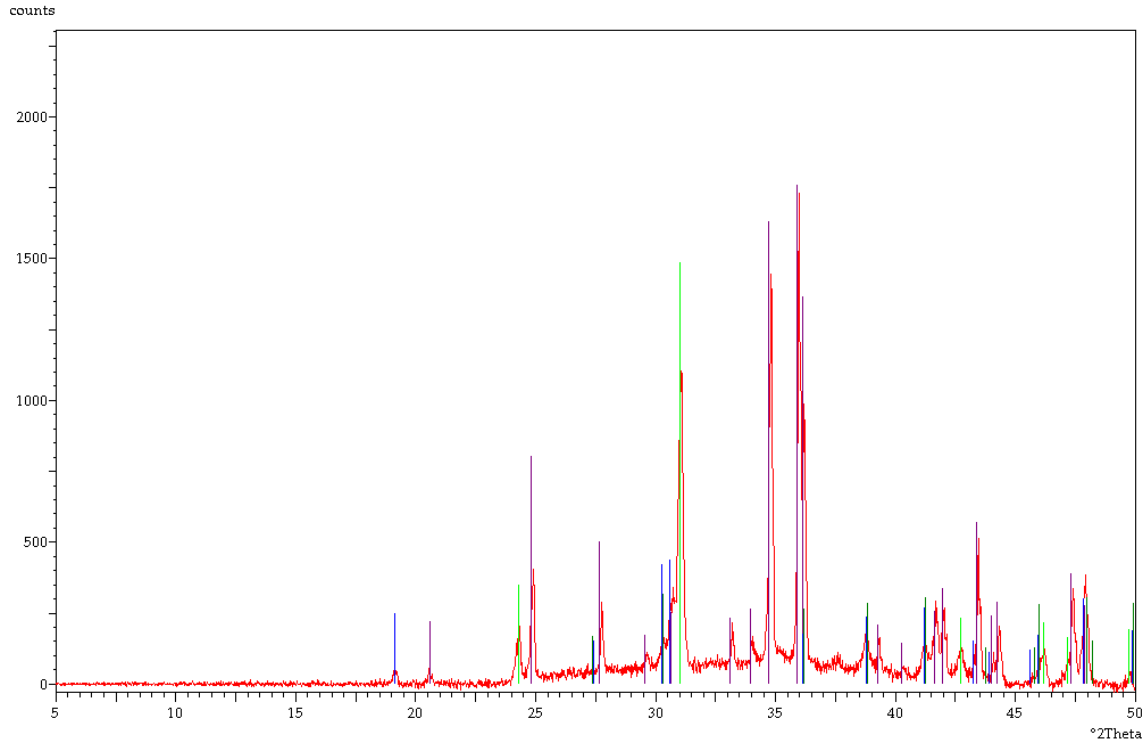


Figure 70. XRD of 4M KOH fly ash L/S=0.4

The XRD spectrum of an alkali activated fly ash sample can be seen in Figure 70. According to the database matching, the following phases can be found in the sample: arcnite (A, K_2SO_4), mullite (M) and quartz (Q), which are represented by the purple, blue and green colors respectively. Although arcnite had a high score in the identification software it is possible that it was wrong, since less than one percent of the fly used was made up from SO_3 .

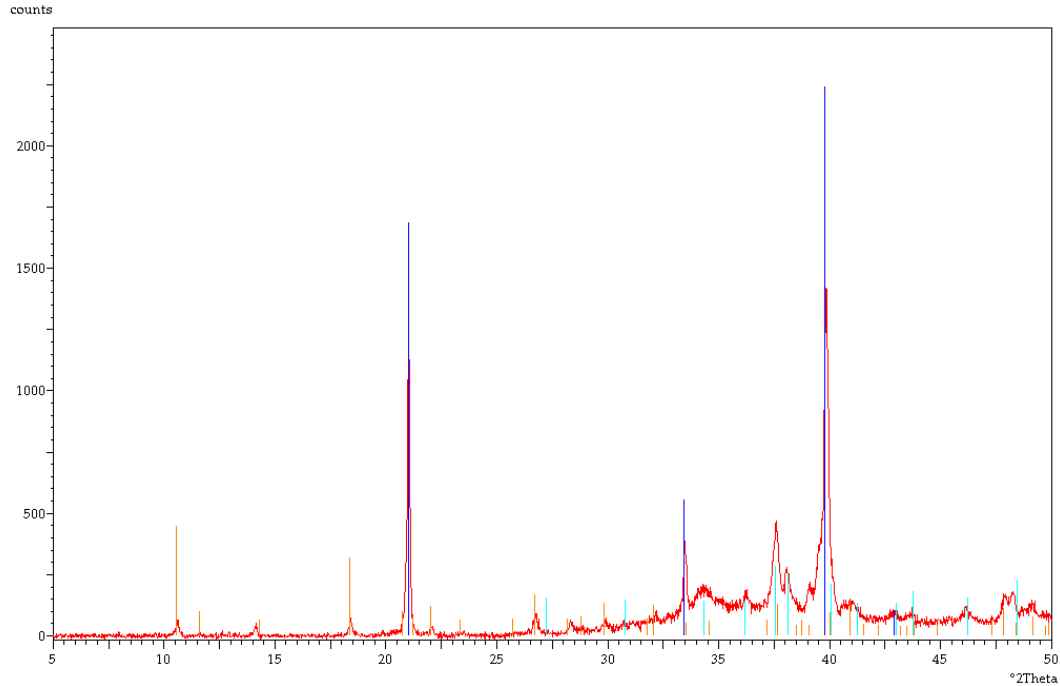


Figure 71. XRD of concrete from Portland cement after 28 days

Figure 71 shows the identified phases of a concrete sample after 28 days of curing. The phases found by the software are ettringite, Ca_2SiO_4 and portlandite (CaOH_2), represented by the orange, teal and blue colors, respectively.

Figure 72 and Figure 73 show the XRD pattern for two geopolymer samples. These samples were prepared from fly ash with a $L/S = 0.4$ and with two different concentrations of KOH activator (4M and 6M). The idea was to study if a different concentration of activator lead to a different structure of geopolymer that could be detected with via XRD. The patterns are very similar, both have the same peaks at the same positions. The blue represent quartz phases while the green lines represent mullite phases in both spectra. This was confirmed by Raman and IR measurement, since both Si-O-Si, Al-O-Si, Si-O and Al-O bonds were detected.

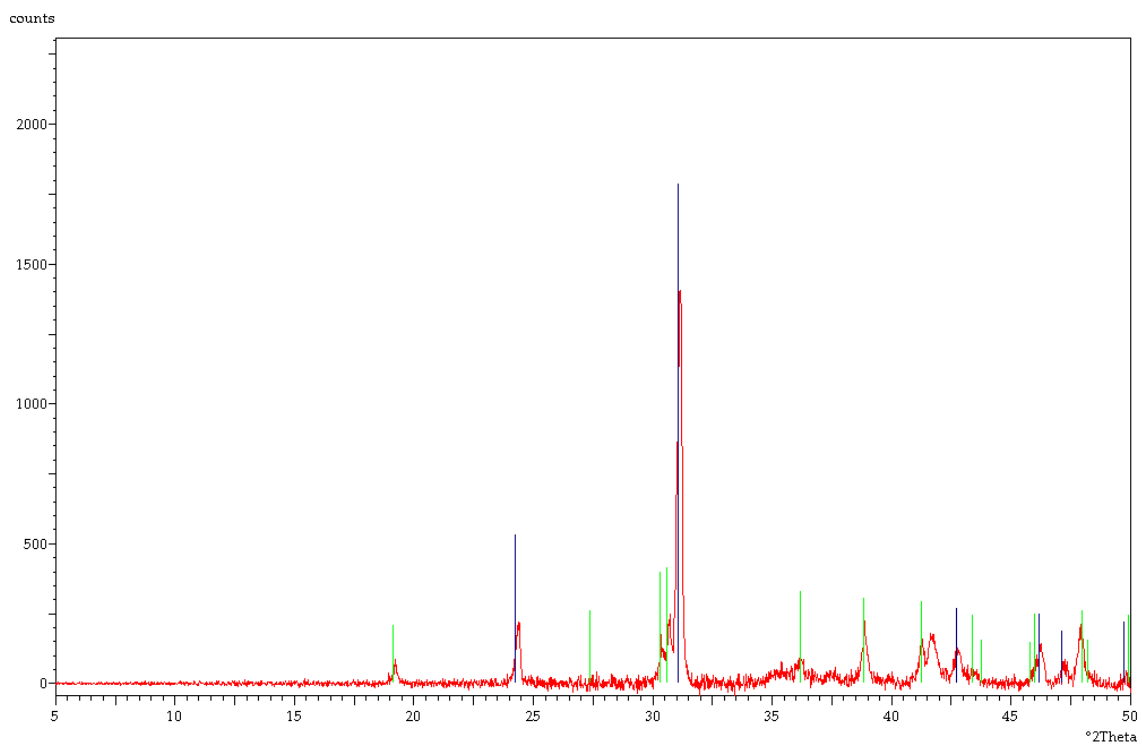


Figure 72. XRD pattern of 28K44 geopolymer sample

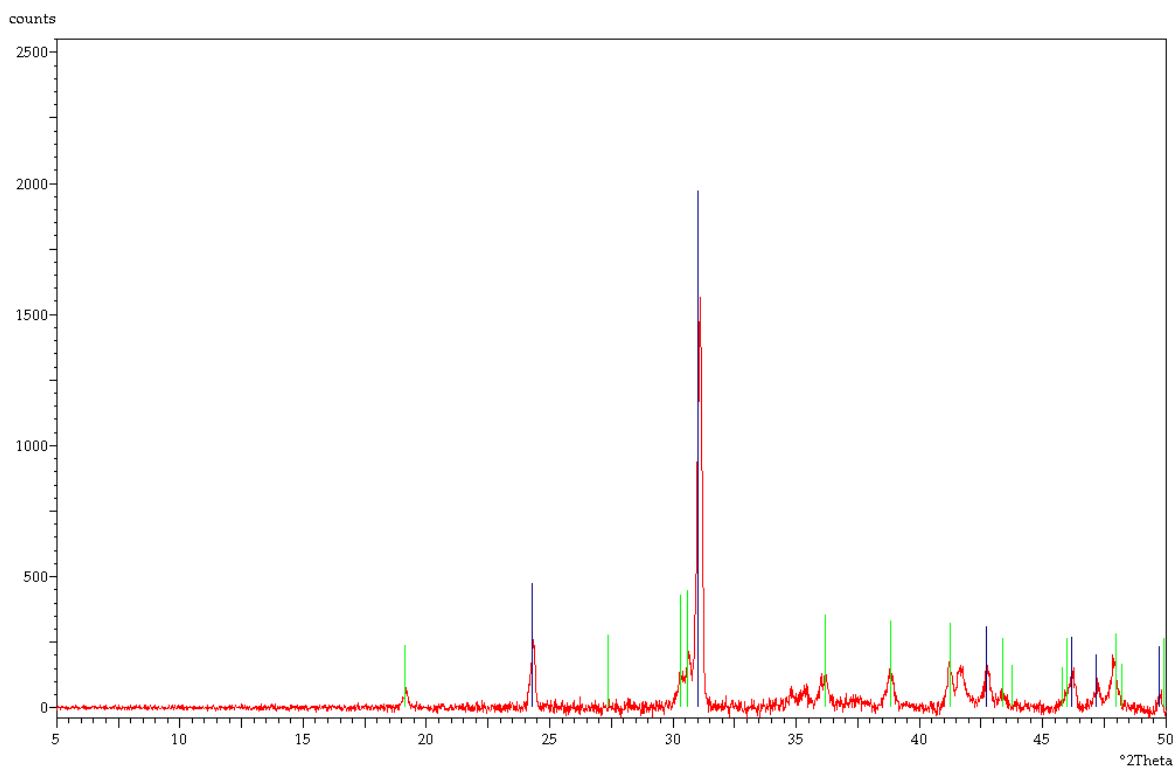


Figure 73. XRD pattern of 28K64 geopolymer sample

6. Compressive strength

6.1. Theoretical background

The compressive strength test is considered one of the more important and is also one of the most simple ones to do because basically is making cylindrical samples from the material it is needed to analyze and break them with a compressive anvil that measure the pressure impose over the samples [45].

This results is important because cements are used in situation where they need to handle compressive stresses and this can usually be used to determine the properties of the material like its durability [45]. The standard for doing this test is in ASTM C192 called “Method of making and curing concrete compression and flexure test specimens in the laboratory” and the selected shape of the sample is cylindrical and the height must be twice of the diameter.

Figure 74 shows the typical anvil used for performing the compressive strength test, the samples are placed in between and the top and bottom side are closed together slowly until the sample is crushed and in the meantime the distance that separates the heads and the force used until the moment of breaking are measured.

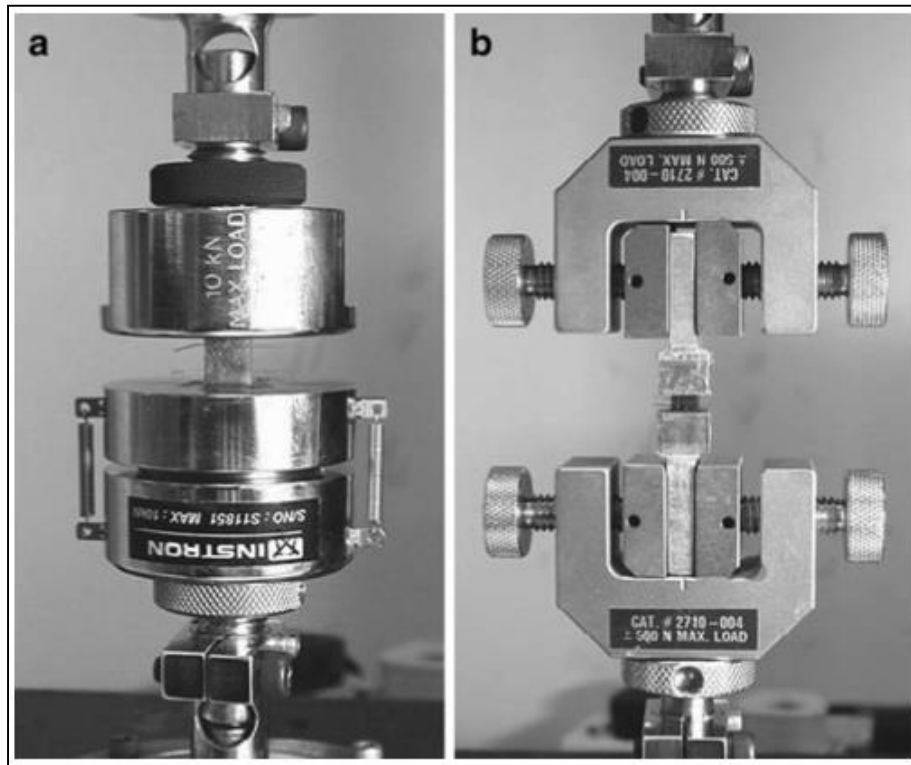


Figure 74. Compression anvils on (a) side and tensile grips on (b) [46]

6.2. What has been done before

On Figure 75 it was recorded the result on compressive strength of geopolymer made using metakaolin with different ratios of $\text{Na}_2\text{O}/\text{SiO}_2$.

It could be observed the metakaolin strength, which is associated with the binders, would increase with the concentration of Si/Al but there is a point, near 2.0 ratio that the necessary strength needed would be less but this may be attributed to sample preparation.

The same result can be seen in the left side of the figure that shows the Si MAS NMR analysis done on the same samples. The growth in height for each of the spectra is a product of the substitution of Al in the silicate network and less distribution of connectivity types Q4 [11].

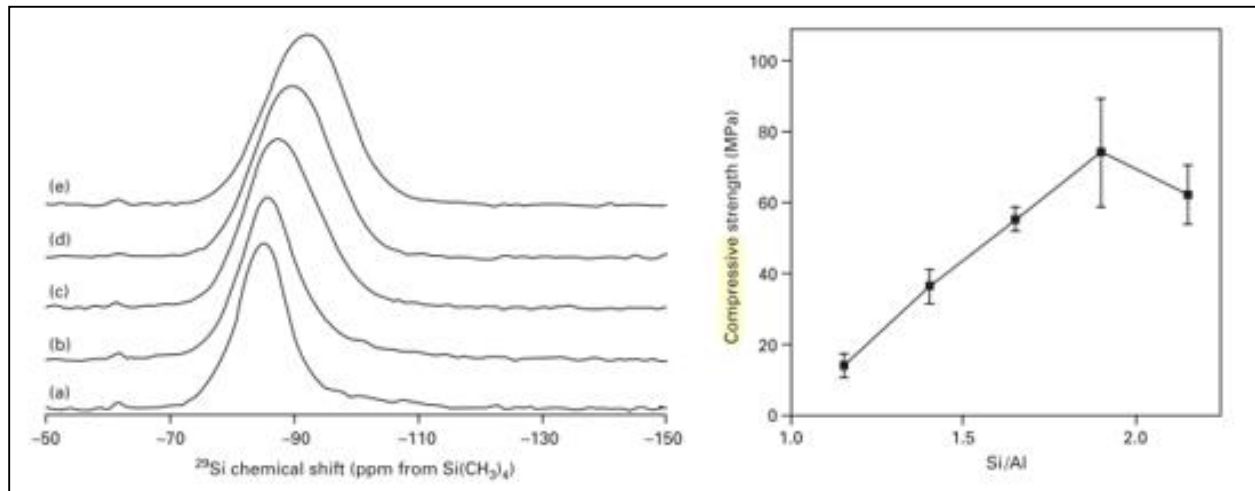


Figure 75. Compressive strength test done on geopolymers [11]

A dependence of the liquid and solids ratio has been observed when performing the compressive strength test on samples, and the results are shown in the next table.

Table 13. Compressive strength for samples with different water and ash ratios [47]

Water/ash ratio	0.2 (No. 1)	0.25(No. 2)	0.3(No. 3)	0.35(No. 4)
Compressive strength before heated (MPa)	113.8	103.5	102.2	83.4
Compressive strength after 500°C heated (MPa)	95.9	62.7	65.4	46.6
Reduction rate %	15.7%	39.4%	36.0%	44.1%

The conclusion that can be reach is that the lower the ratio, the more strength would be required in order to break the samples, as seen how the rupture point is reach at 113,8 MPa for the sample with 0,2 ratios while the one with 0,35 ratios was broken with only 83,4 MPa.

6.3. Experiments and analysis

The compressive strength tests were performed using a LLOYD LR 50K press that is shown in figure 71. The samples that were created are shown on the next table:

Table 14. Compressive strength samples

Sample	Name	Diameter (mm)	Height (mm)
1	2A 0K47	25	50
2	2A 0K44	25	50
3	2A 0K67	25	50
4	2A 0K44	25	50
5	CFA 0K47	25	50
6	CFA 0K67	25	50

The samples were removed from the plastic containers and their surface was smoothed and shaping was done on the sides of the cylinder to make it even. The sample was placed in the press and a compressive test was run, by slowly lowering the press on top of the sample and measuring the force from the point of contact until the moment of rupture where the samples are pulverized. The point of rupture was recorded and using the area of the cylinder the pressure necessary was calculated. On Figure 76 a type of wall was placed all around the sample because once the samples were broken concrete debris would be flying all around:



Figure 76. Compressive machines used for the experiments

On Figure 77, some remaining of the broken samples can be observed and also the file that was used to smooth the circles of the cylinder as much as possible.



Figure 77. Example of breakibroken samples and smoothing of the surfaces

Figure 78 shows a sample ready to be broken using the press once the edges were make more symmetrical and flat as possible.

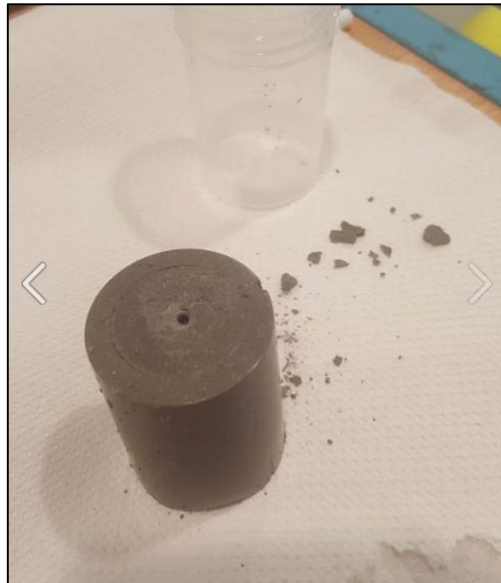


Figure 78. Example of a sample after being dried in the ovenr for 7 days

It is important to note from table 10 that 2A refers to two activators, meaning both the potassium hydroxide and the potassium silicate, the rest of the names has already been explained. This was done because more samples were created using only KOH as the activator but some of them were badly damaged after being taken out of the oven so they could not be broken.

Figure 79 shows the record of a run for the compressive strenght test for sample 0K47, which had a height of 50 mm and diameter of 25 mm. The force exerted by the press in Newtons onto the sample can be seen increasing in a relatively fixed slope until it reaches the rupture point. At

this point the sample broke, and it was recorded as rupture. The time that was necessary in order to reach the rupture point was also recorded and it is reflected in the x-axis in seconds and the load measured is on the y-axis.

Similar plots were generated for the other samples and they were placed in the appendix, it was not deemed necessary to compare them because all of them are similar. The problem with the results was the lack of repeatability of the experiment because there was insufficient material to make more sample and some of the results were not according to expectations. Nevertheless, all of them were recorded in Table 15.

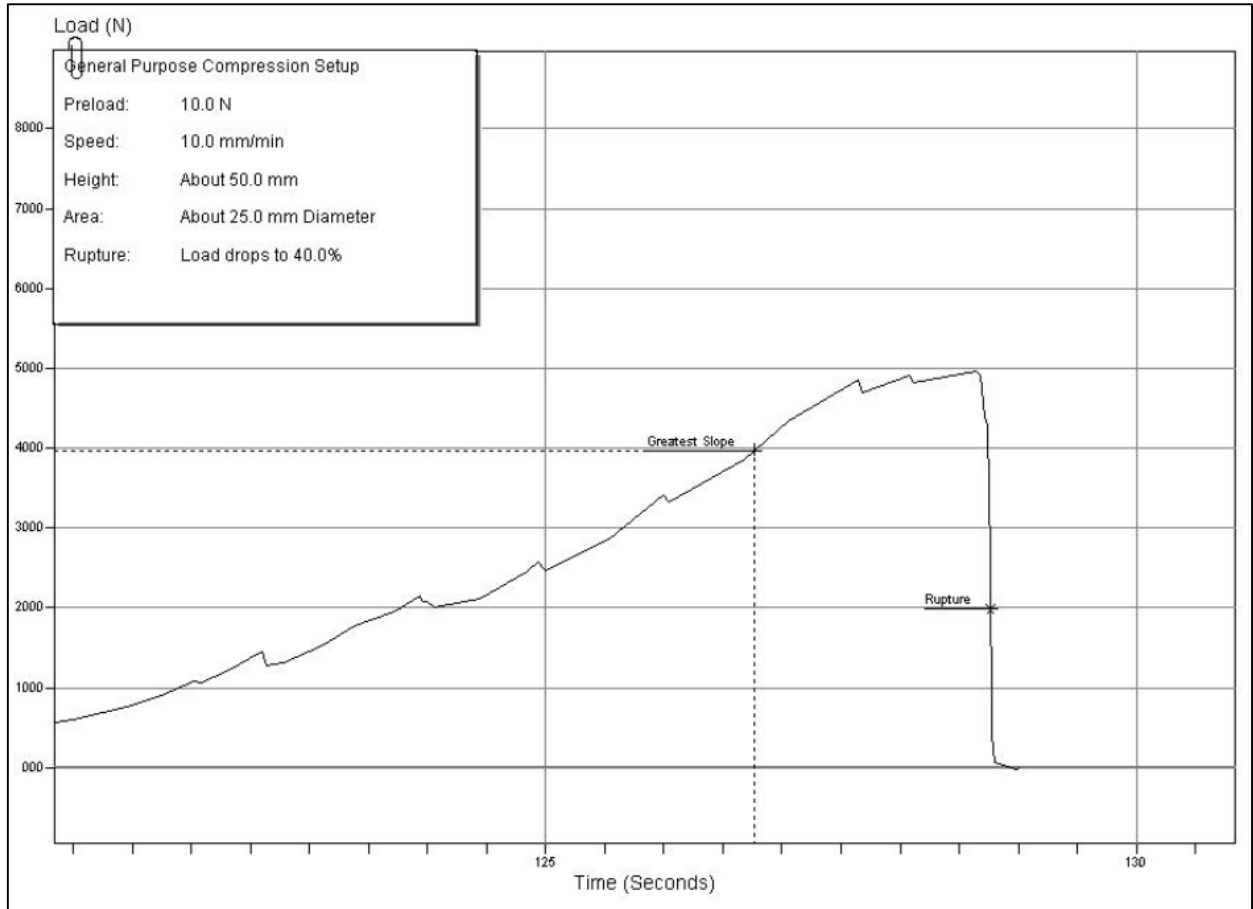


Figure 79. Compressive strength test performed in sample 0K47

Table 15. Rupture point for all the samples

Sample Name	Stress at Maximum Load (MPa)
2A 0K47	9,87
2A 0K44	12,63
2A 0K67	20,15
2A 0K64	12,05
CFA 0K47	12,68
CFA 0K67	27,70

The cement samples were mixed with both of the activators in order to compare what would the effect be by using similar conditions as the pure fly ash samples; the only difference with the cement samples was they were mixed in a 1:1 ratio with the fly ash. The results from Table 15. were place in Figure 80 to gives more graphical view for easier comparison.

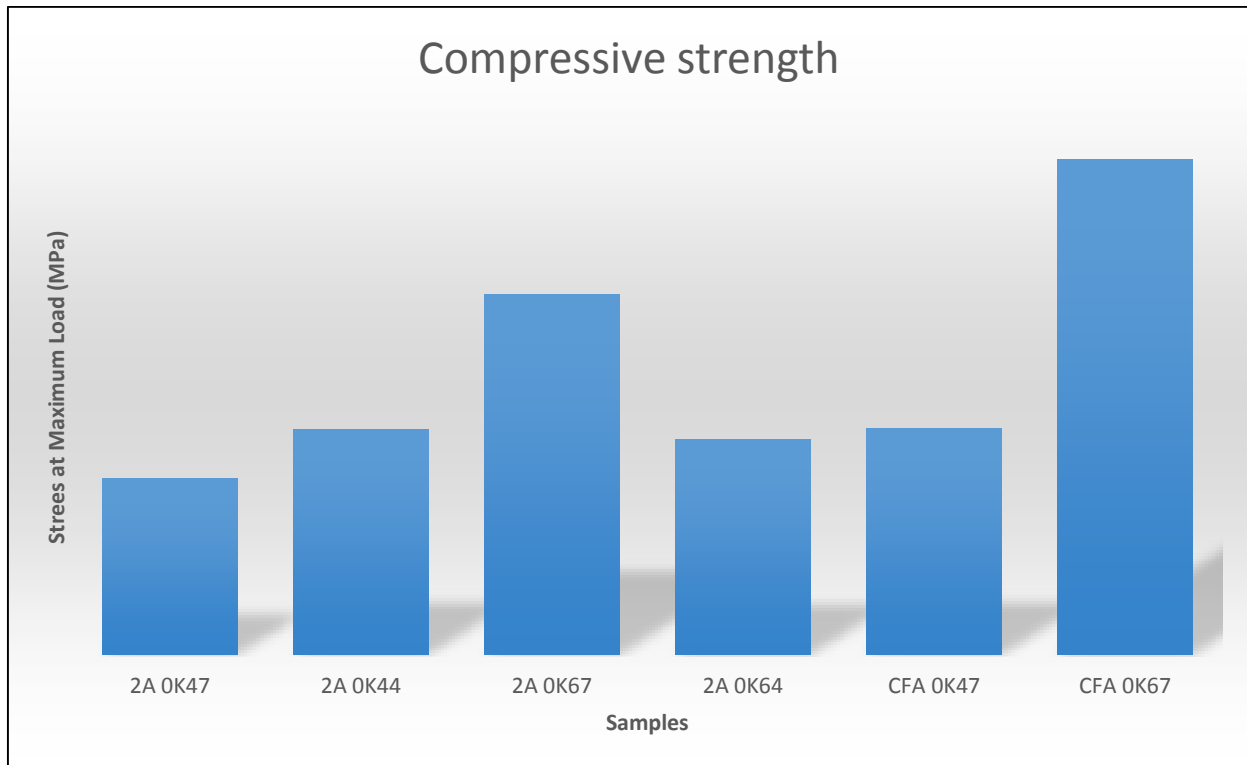


Figure 80. Compressive strenght results for the samples

A factor that could affect the results would have been the presence of too many air bubbles inside the samples, even after the use of the ultrasonic mixer; bigger bubbles were observed on the samples with the thickest consistence, meaning the ones with the lowest ratio of L/S.

However, some of the expected results can be observed like in the case of the two samples of Portland cement fly ash mixes (CFA). It is expected that the samples with a higher concentration of potassium hydroxide activator will make the reaction of the polymer go faster so the hardness

of the sample should be greater; the force for CFA 0K67 was 27,7 MPa and for CFA 0K47 was 12,68 MPa, meaning for the smallest ratio it was almost twice.

Another expected results can be observed when comparing 2A0K47 and 2A0K44, which shows 9,87 MPa for the ratio of 0,7 and 12,63 MPa for the L/S ratio of 0,4, proving that the sample with the smallest ratio was the strongest. The reason for this is that the 0,4 liquid/solid ratio has a less amount of water and this will make for a much denser and stronger geopolymeric material. The higher activator concentration and low L/S ratio could mean the polymerization reactions were faster than in the other samples.

The only results that is not consistent was the comparison of 2A0K67 and 2A0K64, which rupture point was 20, 15 and 12,05 MPa respectively. As explained before, the assumption of more pores appearing because of the bubbles generated during mixing, which may have happened to the sample 2A0K64. For this sample, the activator concentration was 6 M and the ratio of liquid solids was 0,4, which make this the sample with the fastest reactions.

Later on, using another batch of fly ash to try to recreate the results for this sample showed that it started to solidify considerably faster, as soon as it was been place in the plastic containers. This is also the reason why there were no samples for the cement and fly ash samples for the L/S ratio below 0,4 in either the 4 M and the 6 M samples. Ratios below 0,4 were too viscous to handle effectively and they also exhibited fast setting times, so they were impractical to work with.

7. Conclusions

The disappearing of Gypsum bands (670 and 1000 cm^{-1}) and the 650 cm^{-1} and of C-S-H shows the curing taking place. In the same way, the band of CH that appears at 2000 cm^{-1} also indicates the geopolymerization is taking place. The Raman bands showed a higher intensity for the samples with a lower liquid to solid ratio. This is usually related to the increase of the reaction speed the lower the water content is in the samples.

The IR measurements showed the geopolymerization taking place by the change T-Si-O peaks (T = Si or Al) located around 1000 cm^{-1} . Carbonation by the absorption of atmospheric CO_2 could also be observed by increasing peaks at $\sim 1650\text{ cm}^{-1}$. The adsorption of water from the atmosphere and possibly weakly bound water molecules could be observed at $3700\text{-}2500\text{ cm}^{-1}$. Some fly ash samples exhibited ettringite formation after 28 days of curing.

The exothermic peaks that appear around $100\text{ }^\circ\text{C}$ belong to the evaporation of water from the slurry samples. The amount of water decreased with the progressing of the curing time, which was reflected in the decrease of the evaporation peak after 14 days. The calorimetric properties between the Geopolymers made with Portland cement and the ones done with fly ash were similar between $25\text{ }^\circ\text{C}$ and $550\text{ }^\circ\text{C}$. Both type of materials show the evaporation peak and no further significant change until reaching the temperature limit.

XRD has shown gypsum and C_3S phases in unreacted Portland cement, which have also been confirmed by Raman and spectroscopy indirectly. Reacted PC has been shown to contain C_2S , ettringite and portlandite phases. For geopolymer fly ash samples, the alumino-silicate mullite phase has been identified as well as quartz phases. The corresponding Si-O, Al-O-Si and Al-O bands have all been confirmed by IR and Raman spectroscopy as well.

The strength achieved in the breaking point will be directly proportional to the concentration of the activator used. The stresses were $9,87\text{ MPa}$ and $20,17\text{ MPa}$ for samples 0K47 and 0K67 respectively, meaning an increment in stress with the increase of concentration from 4 M to 6 M. The stresses were $12,68\text{ MPa}$ and $27,7\text{ MPa}$ for samples 4M cement and 6M cement, respectively.

The lower amount of water will yield samples with higher stress because the curing reaction is faster, as observed the samples 0K47 and 0K44, where the stresses were $9,87\text{ MPa}$ (0,7 ratio of L/S). and $12,63\text{ MPa}$ (0,4 ratio of L/S) respectively.

8. Recommendations

The most important would be to request fly ash in bulk in order to ensure repeatability of all the experiments.

For the Raman experiments, the decrease of the intensity of the laser and increase in the exposure time of the samples should be a solution to counter the fluorescent behavior of the fly ash. The study of a single sample of Geopolymers over a long period of time and at regular intervals is also suggested in order to understand with more detailed how the bands are shifting. Further recommendations for the Raman apparatus would be a bigger and user-friendly black box that can hold the samples easier.

In the IR experiments, taking the slurries or samples after a day of hardening could be beneficial in order to learn more about the early stages of the geopolymerization process.

Regarding the DSC analysis, using different machine that can reach a higher temperature could be useful in locating peaks to calculate the curing time of the fly ash. The use of pressure crucibles in trying to determine exactly how much of the energy released in the 100 C peaks is part of the evaporation of water or something else.

XRD measurements could be performed between 28 days and the sample materials in order to follow any changes in the phases geopolymer samples.

Once both the DSC and Raman suggestions take place, a comparison for the bands shift of the Raman with the degree of curing calculated using DSC could be generated and in further studies the increase of the band can be used to calculate de degree of cure using Raman only.

In the compressive strength test, the use of other types of activators as well as other sizes of samples is advised in order to study the behavior of the material. Additionally, the dependence of the results with the temperature used during the curing time would be useful to study.

9. Bibliography

- [1] N. Garg, “Raman spectroscopy for characterizing and determining the pozzolanic reactivity of fly ashes,” Iowa State University, 2012.
- [2] CEMBUREAU, “Cement & Concrete: Key facts & figures.” [Online]. Available: <http://www.cembureau.be/about-cement/key-facts-figures>. [Accessed: 05-May-2016].
- [3] “BP Statistical Review of World Energy in 2014,” London, 2015.
- [4] “Danish Climate and Energy Policy.” .
- [5] “Coal Electricity Diagram.” [Online]. Available: http://www.worldcoal.org/sites/default/files/styles/feature-event-carousel/public/Coal-Electricity-Diagram_1.jpg?itok=FIJfd1UW. [Accessed: 25-May-2016].
- [6] Z. T. Yao, X. S. Ji, P. K. Sarker, J. H. Tang, L. Q. Ge, M. S. Xia, and Y. Q. Xi, “A comprehensive review on the applications of coal fly ash,” *Earth-Science Rev.*, vol. 141, pp. 105–121, 2015.
- [7] “Coal Combustion Products Production & Use Statistics.” [Online]. Available: <http://acaa.affiniscape.com/displaycommon.cfm?an=1&subarticlenbr=3>.
- [8] Y. Luna, C. Fernández-Pereira, J. F. Vale, and L. Alberca, “Waste Stabilization/Solidification (S/S) of EAF dust using fly ash-based geopolymers. Influence of carbonation on the stabilized solids,” in *World of Coal Ash (WOCA) Conference, 2009*, vol. 2, no. 1, pp. 1–13.
- [9] J. P. Capp and L. M. Adams, “Reclamation of Coal Mine Wastes and Strip Spoil with Fly Ash,” pp. 26–37.
- [10] O. Kayali, “Fly ash lightweight aggregates in high performance concrete,” *Constr. Build. Mater.*, vol. 22, no. 12, pp. 2393–2399, 2008.
- [11] J. Provis and J. van Deventer, *Geopolymers: Structure, processing, properties and industrial applications*, 1st ed. Cambridge: CRC, 2009.
- [12] S. H. Kosmatka and M. L. Wilson, *Design and Control of Concrete Mixtures*, 15th ed. Skokie, Illinois, USA: Portland Cement Association, 2011.
- [13] H.-P. Boehm, “The Chemistry of Silica. Solubility, Polymerization, Colloid and Surface Properties, and Biochemistry. Von R. K. Iler. John Wiley and Sons, Chichester 1979. XXIV, 886 S.,” *Angew. Chemie*, vol. 92, no. 4, pp. 328–328, Apr. 1980.
- [14] Z. H. Zhang, H. J. Zhu, C. H. Zhou, and H. Wang, “Geopolymer from kaolin in China: An overview,” *Appl. Clay Sci.*, vol. 119, pp. 31–41, 2016.

- [15] P. Duxson, A. Fernández-Jiménez, J. L. Provis, G. C. Lukey, A. Palomo, and J. S. J. van Deventer, "Geopolymer technology: The current state of the art," *J. Mater. Sci.*, vol. 42, no. 9, pp. 2917–2933, 2007.
- [16] F. J. M. Rivera, "STRENGTH AND DURABILITY OF FLY ASH-BASED FIBER-REINFORCED GEOPOLYMER CONCRETE IN A SIMULATED MARINE ENVIRONMENT," Florida Atlantic University, 2013.
- [17] R. J. Detwiler, "The Role of Fly Ash Composition in Reducing Alkali-Silica Reaction," no. 2092, pp. 1–33, 1997.
- [18] "Why Alkali-Activated Materials are NOT Geopolymers? – Geopolymer Institute." [Online]. Available: <http://www.geopolymer.org/faq/alkali-activated-materials-geopolymers/>. [Accessed: 07-May-2016].
- [19] A. Palomo and A. Fernández-Jiménez, "Alkaline Activation, Procedure for Transforming Fly Ash into New Materials. Part 1: Applications," *Proc. World Coal Ash (...)*, pp. 1–14, 2011.
- [20] H. L. Chang, C. M. Chun, I. A. Aksay, and W. H. Shih, "Conversion of fly ash into mesoporous aluminosilicate," *Ind. Eng. Chem. Res.*, vol. 38, pp. 973–977, 1999.
- [21] E. Smith and G. Dent, *Modern Raman Spectroscopy - A Practical Approach*. Chichester: John Wiley & Sons, Ltd., 2005.
- [22] P. J. Larkin, *IR and Raman Spectroscopy - Principles and Spectral Interpretation*. Elsevier Inc., 2011.
- [23] J. R. Ferraro, K. Nakamoto, and C. W. Brown, *Introductory Raman Spectroscopy*. Elsevier Ltd, 2003.
- [24] J. Bensted, "Uses of Raman Spectroscopy in Cement Chemistry," *J. Am. Ceram. Soc.*, vol. 59, no. 3, pp. 140–143, 1976.
- [25] M. Conjeaud and H. Boyer, "Some possibilities of Raman microprobe in cement chemistry," *Cem. Concr. Res.*, vol. 10, no. 1, pp. 61–70, 1980.
- [26] D. Bonen, T. J. Johnson, and S. L. Sarkar, "Characterization of principal clinker minerals by FT-Raman microspectroscopy," *Cem. Concr. Res.*, vol. 24, no. 5, pp. 959–965, 1994.
- [27] C. D. Dyer, P. J. Hendra, and W. Forsling, "The Raman spectroscopy of cement minerals under 1064 nm excitation," *Spectrochim. Acta Part A Mol. Spectrosc.*, vol. 49, no. 5–6, pp. 715–722, 1993.
- [28] M. Tarrida, M. Madon, B. Le Rolland, and P. Colombet, "An in-situ Raman spectroscopy study of the hydration of tricalcium silicate," *Adv. Cem. Based Mater.*, vol. 2, no. 1, pp. 15–20, 1995.

- [29] N. Garg, K. Wang, and S. W. Martin, “A Raman spectroscopic study of the evolution of sulfates and hydroxides in cement-fly ash pastes,” *Cem. Concr. Res.*, vol. 53, pp. 91–103, 2013.
- [30] R. Onori, “Alkaline activation of incinerator bottom ash for use in structural applications.,” p. Roma, 2011.
- [31] “University of Minnesota’s Mineral Pages: Calcite.” [Online]. Available: <https://www.esci.umn.edu/courses/1001/minerals/calcite.shtml>. [Accessed: 04-Jun-2016].
- [32] C. A. Rees, J. L. Provis, G. C. Lukey, and J. S. J. Van Deventer, “In situ ATR-FTIR study of the early stages of fly ash geopolymer gel formation,” *Langmuir*, vol. 23, no. 17, pp. 9076–9082, 2007.
- [33] F. Liu and Z. Sun, “Chemical mapping of cement pastes by using confocal Raman spectroscopy,” *Front. Struct. Civ. Eng.*, vol. 10, no. 2, pp. 168–173, 2016.
- [34] R. Ylmén and U. Jäglid, “Carbonation of Portland Cement Studied by Diffuse Reflection Fourier Transform Infrared Spectroscopy,” *Int. J. Concr. Struct. Mater.*, vol. 7, no. 2, pp. 119–125, 2013.
- [35] H. Biricik and N. Sarier, “Comparative Study of the Characteristics of Nano Silica-, Silica Fume - and Fly Ash - Incorporated Cement Mortars,” *Mater. Res.*, vol. 17, no. 3, pp. 570–582, 2014.
- [36] H. M. Khater and H. A. A. el Gawaad, “Characterization of alkali activated geopolymer mortar doped with MWCNT,” *Constr. Build. Mater.*, vol. 102, pp. 329–337, 2016.
- [37] E. M. Brown, *Introduction to Thermal Analysis*, vol. 1. Dordrecht: Kluwer Academic Publishers, 2004.
- [38] R. Li, L. Wang, T. Yang, and B. Raninger, “Investigation of MSWI fly ash melting characteristic by DSC-DTA,” *Waste Manag.*, vol. 27, no. 10, pp. 1383–1392, 2007.
- [39] X. Gao, Q. L. Yu, and H. J. H. Brouwers, “Reaction kinetics, gel character and strength of ambient temperature cured alkali activated slag-fly ash blends,” *Constr. Build. Mater.*, vol. 80, pp. 105–115, 2015.
- [40] M. Lee, *X-ray Diffraction for Materials Research*. Oakville, Canada: Apple Academic Press, 2016.
- [41] Z. Li and S. Liu, “Influence of Slag as Additive on Compressive Strength of Fly Ash-Based Geopolymer,” *J. Mater. Civ. Eng.*, vol. 19, no. 6, pp. 470–474, 2007.
- [42] X. Guo, H. Shi, and W. A. Dick, “Compressive strength and microstructural characteristics of class C fly ash geopolymer,” *Cem. Concr. Compos.*, vol. 32, no. 2, pp. 142–147, 2010.

- [43] F. Fan, “Mechanical and Thermal Properties of Fly ash-based Geopolymer Cement,” *MSc Thesis*, no. May, 2015.
- [44] S. A. Abo-El-Enein, G. El-kady, T. M. El-Sokkary, and M. Gharieb, “Physico-mechanical properties of composite cement pastes containing silica fume and fly ash,” *HBRC J.*, vol. 11, no. 1, pp. 7–15, 2015.
- [45] M. D. a. Thomas and J. Skalny, “Significance of Tests and Properties of Concrete and Concrete-Making Materials, STP 169D,” *Annu. B. ASTM Stand.*, 2007.
- [46] S. Ji, X. Fan, D. Roberts, a. Hartov, and K. Paulsen, *Tracking Cortical Surface Deformation Using Stereovision*. 2013.
- [47] F. Fan, “Mechanical and Thermal Properties of Fly ash-based Geopolymer Cement,” Louisiana State University, 2015.

10. Appendix

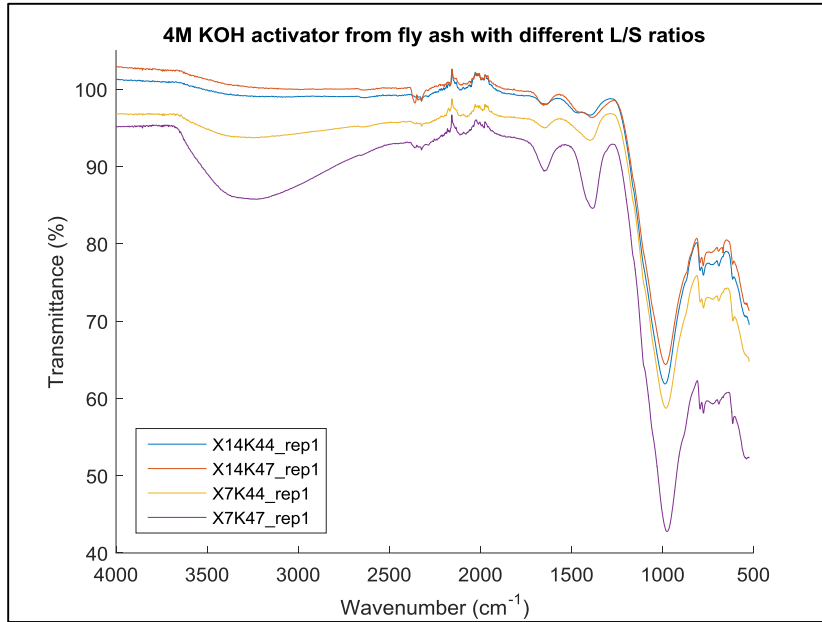


Figure 81. FT-IR of K4 samples at ratios 0,4; 0,5; 0,6 and 0,7

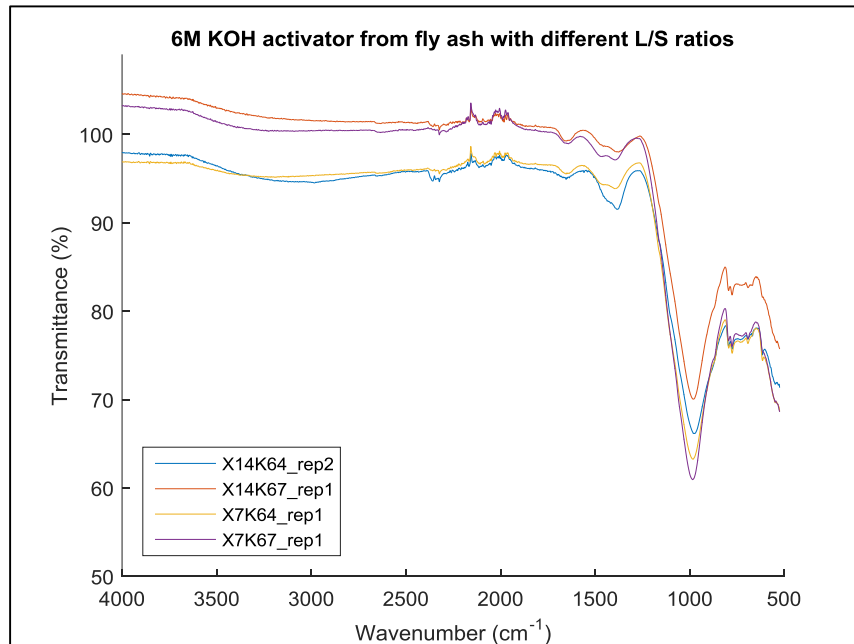


Figure 82. FT-IR of K6 samples at ratios

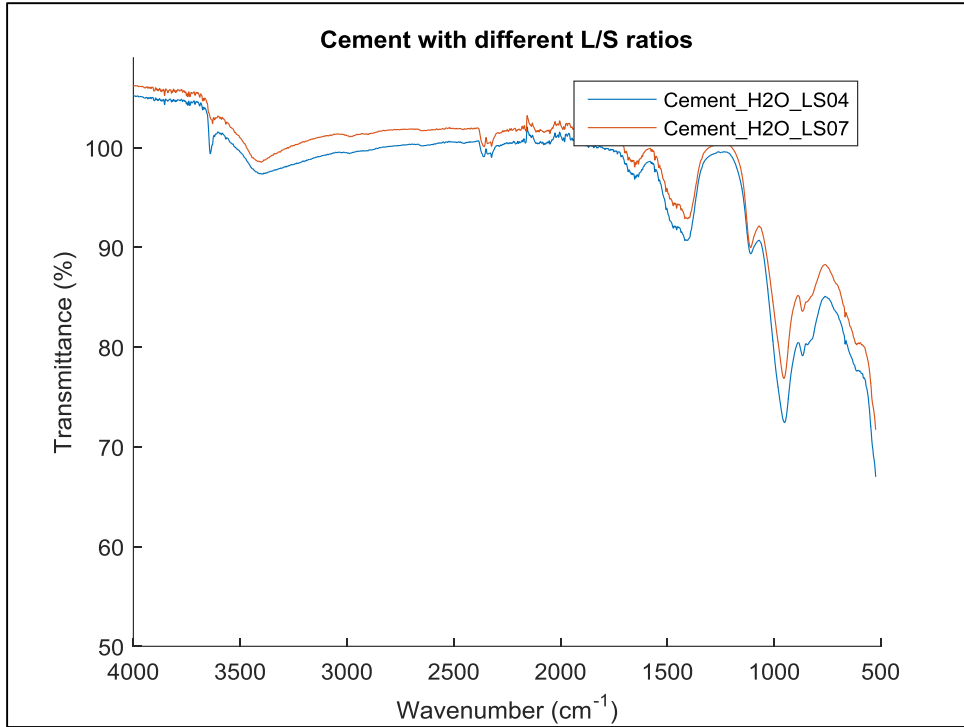


Figure 83. FT-IR of cement samples for ratios 0,4 and 0,7

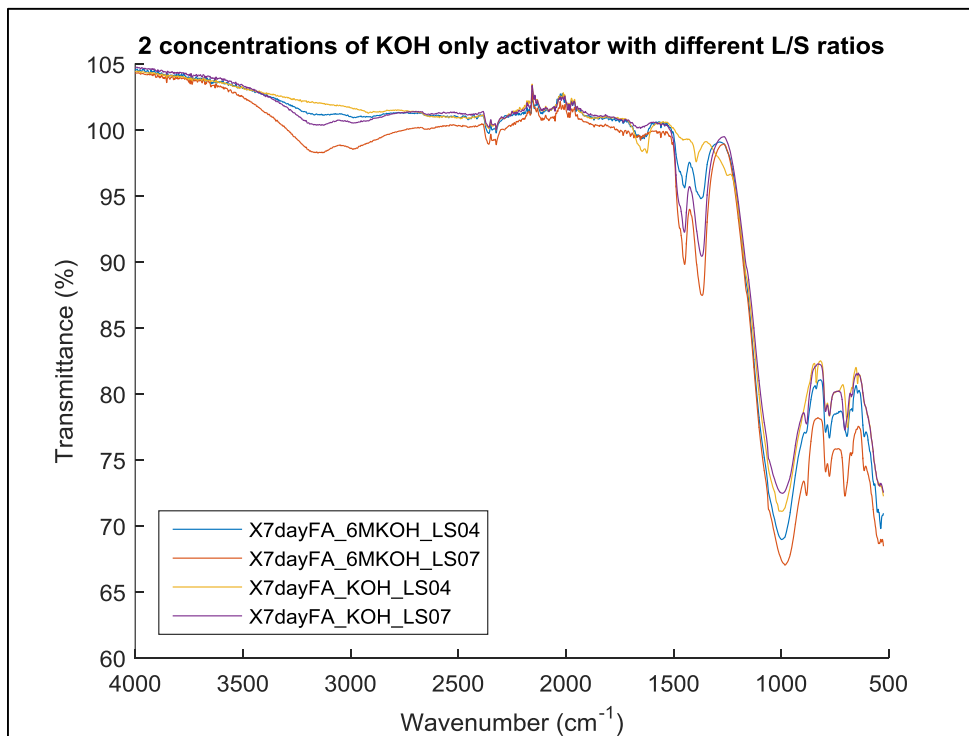


Figure 84. FT-IR of all the samples atfter 7 days of curing

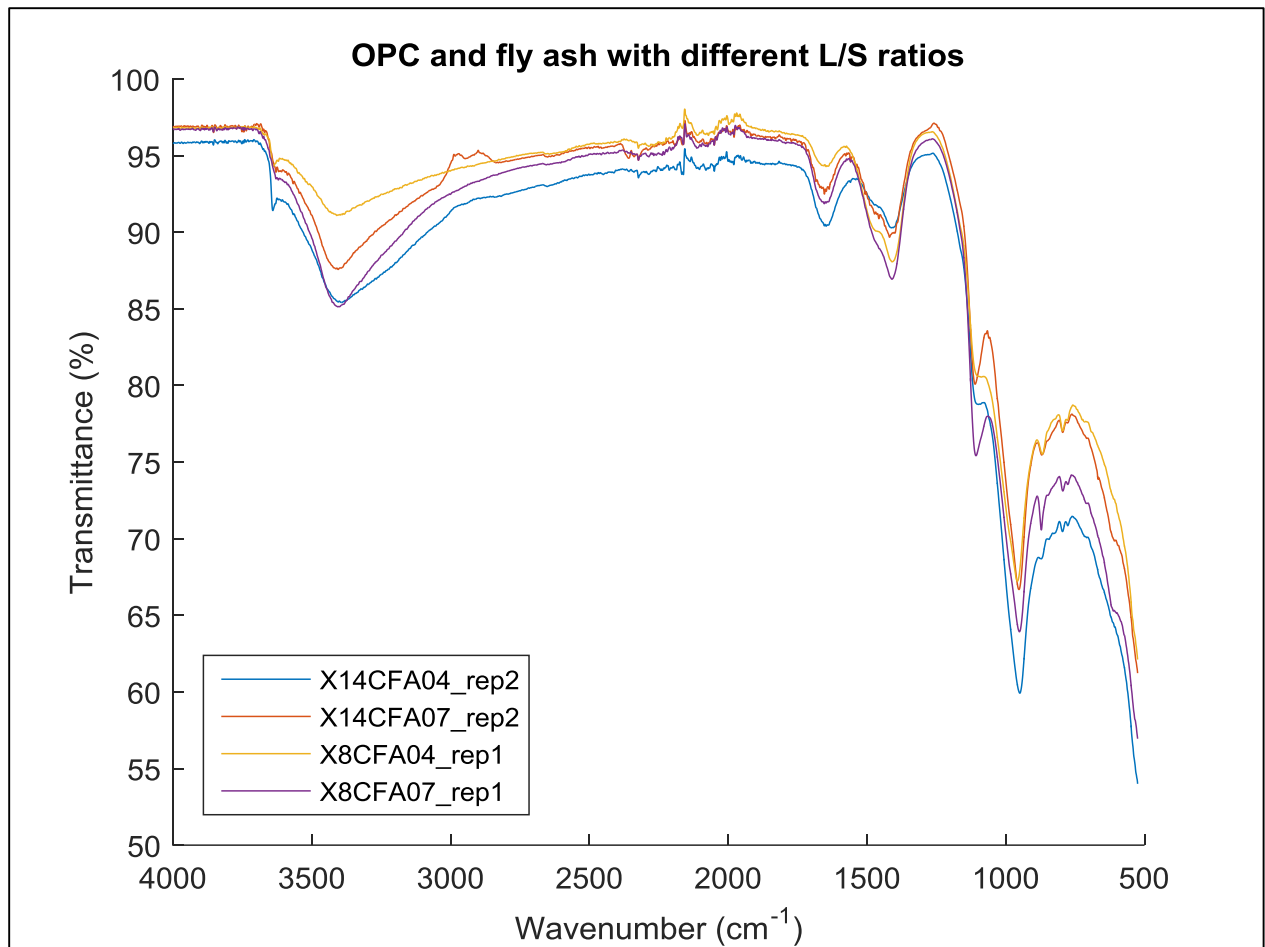


Figure 85 Comparison of the FT-IR for cement samples with 0,4 and 0,7 L/S after 8 and 14 days of curing

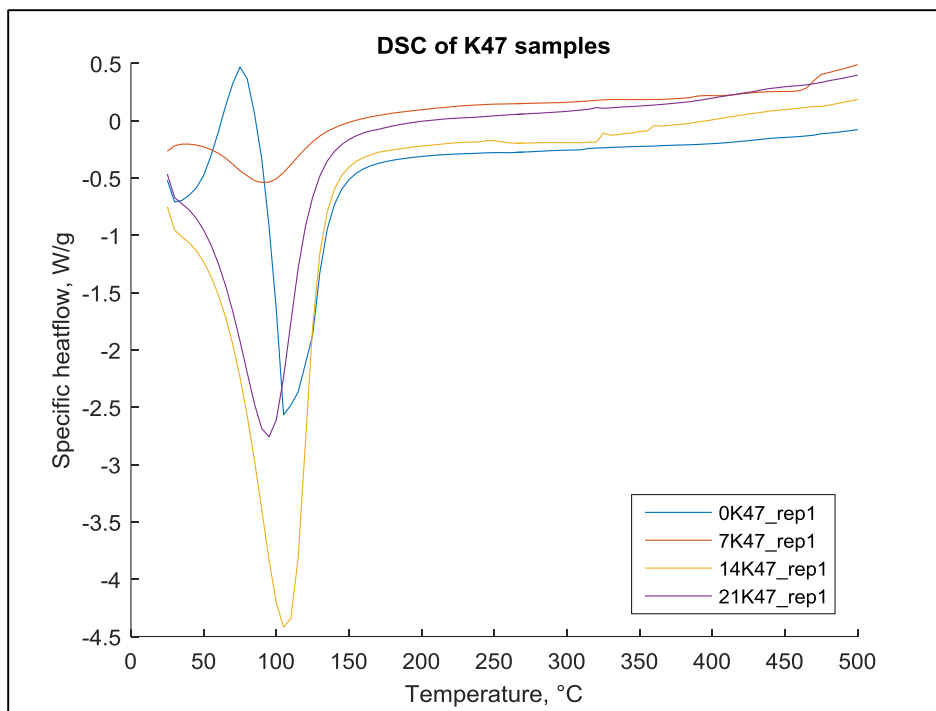


Figure 86. DSC for K47 in slurry and after 7, 14 and 21 days

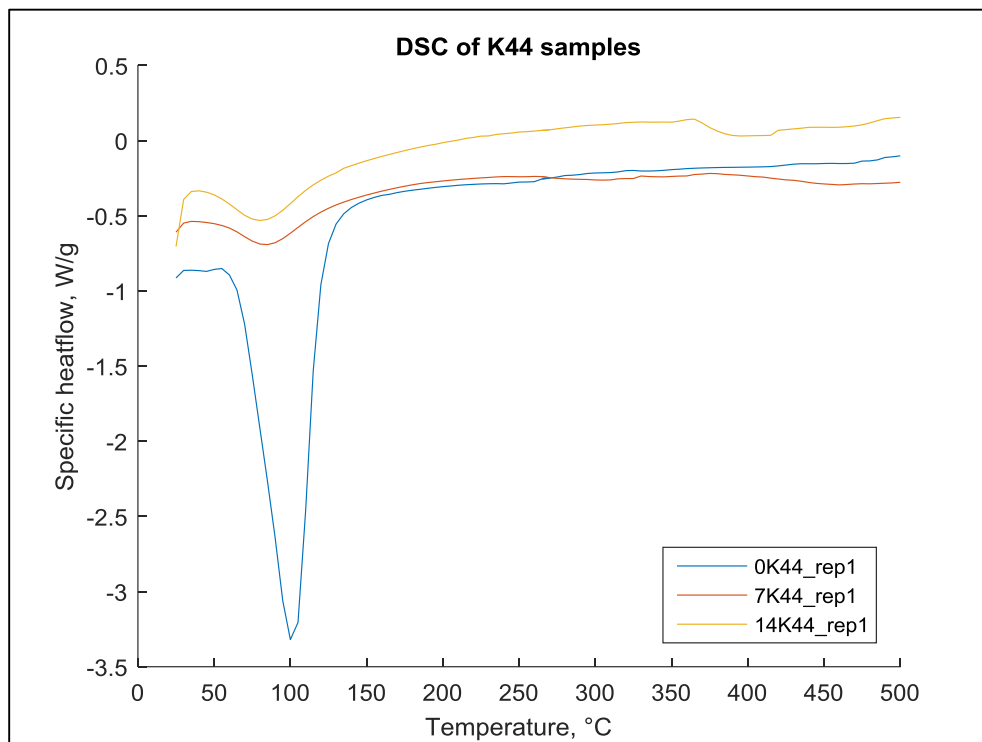


Figure 87. DSC for K44 in slurry and after 7 and 14 days

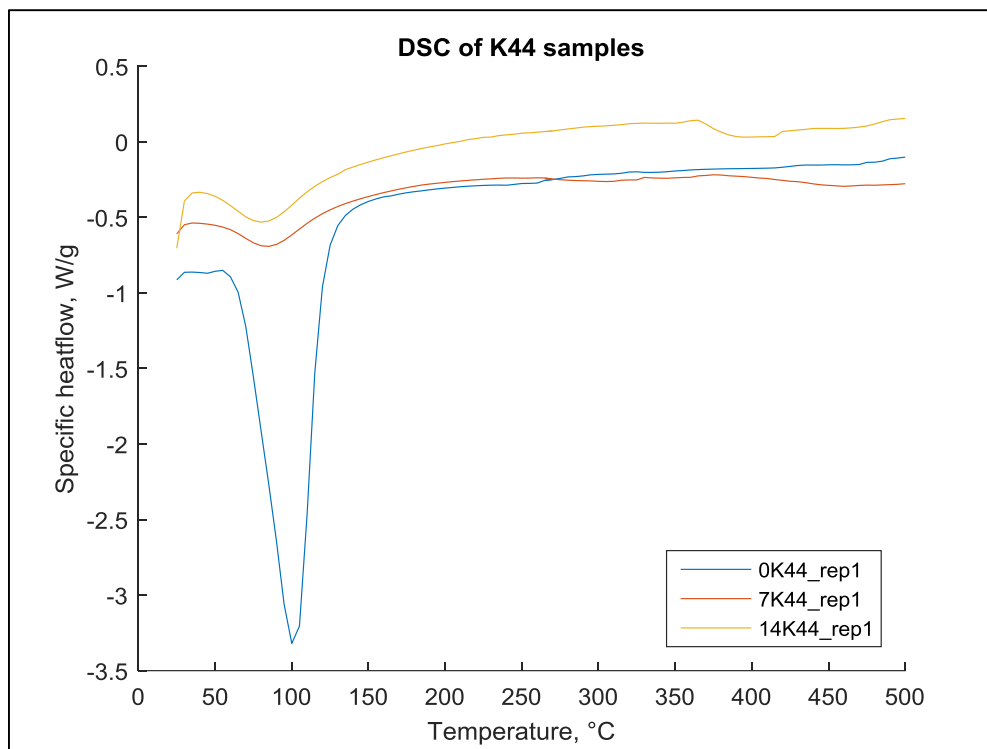


Figure 88. DSC for K67 in slurry and after 7 and 14 days

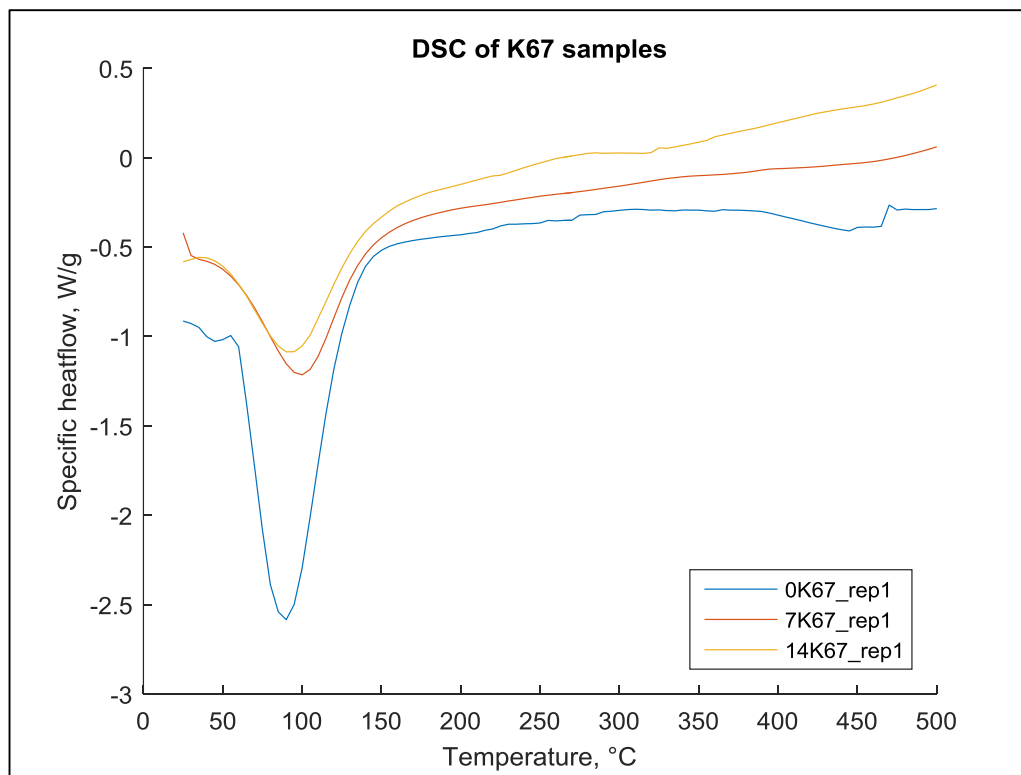


Figure 89. DSC for K67 in slurry and after 7 and 14 days

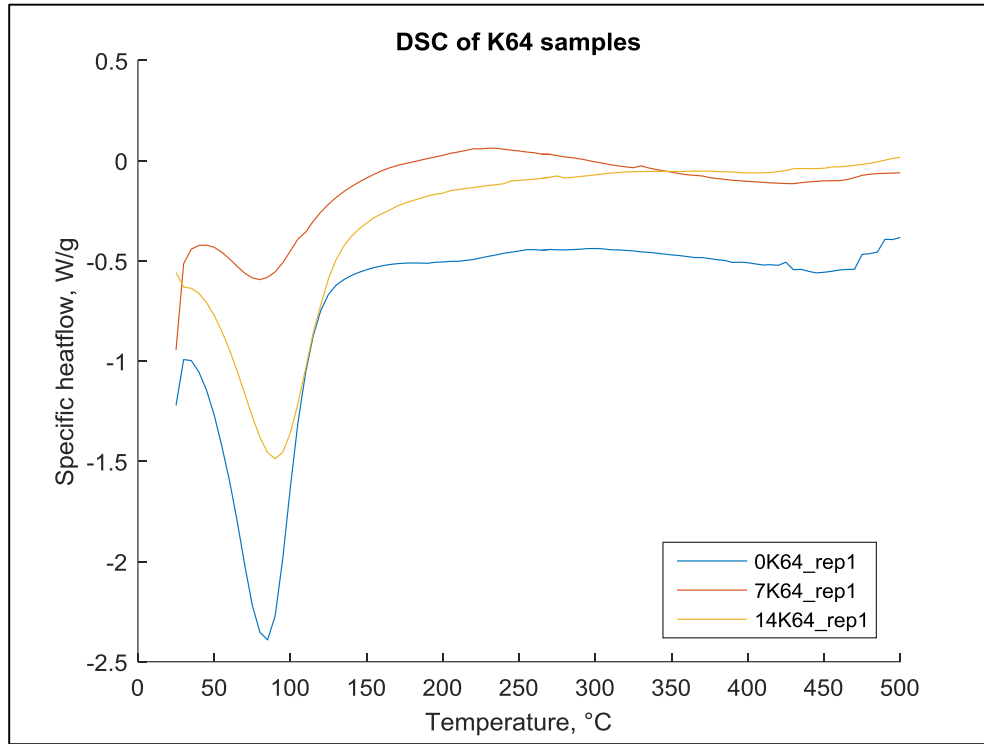


Figure 90 DSC for K64 with 0,4 ratio of L/S in slurry and after 7 and 14 days.

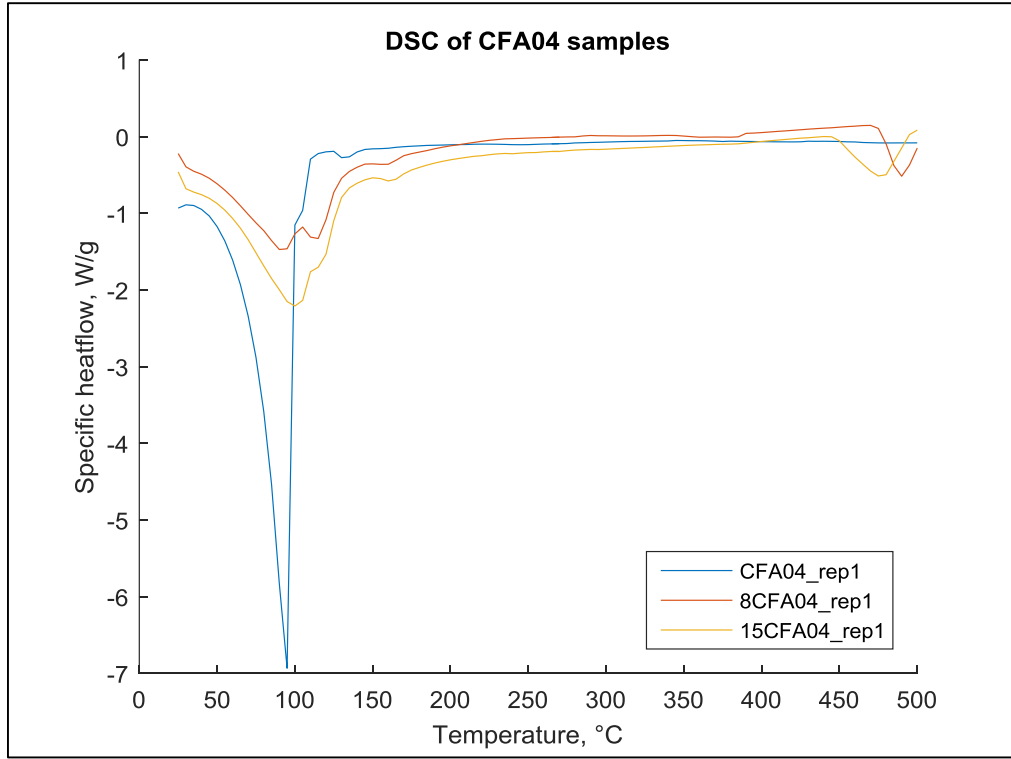


Figure 91 DSC for a cement sample iwth 0,4 ratio of L/S as slurry and after 8 and 15 days.

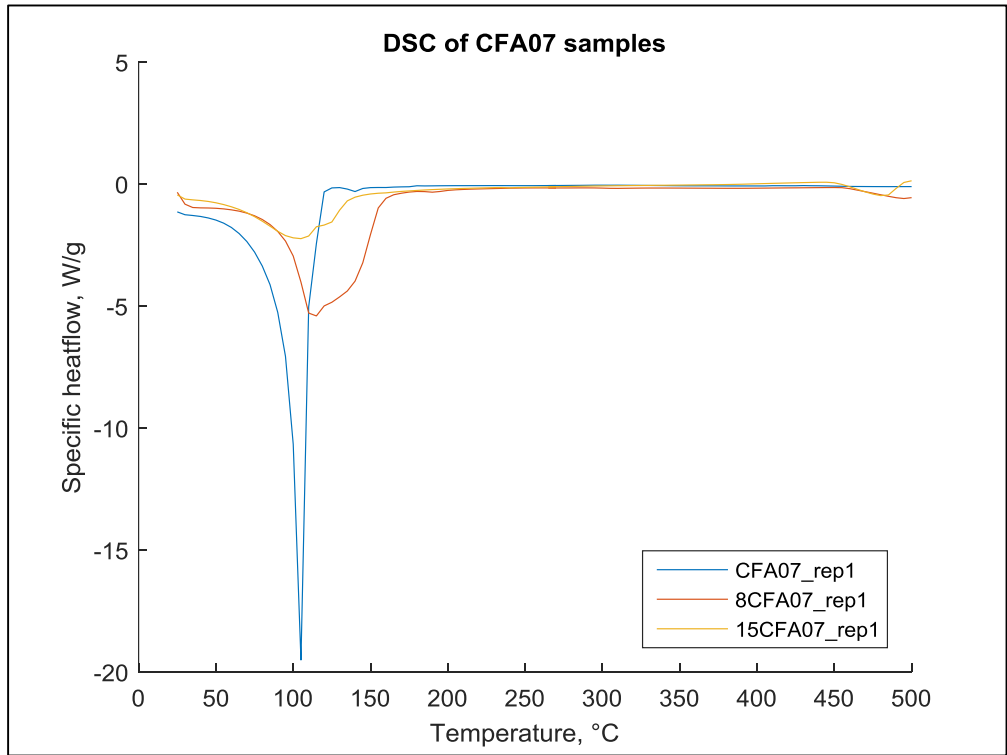


Figure 92. DSC for a cement sample iwth 0,7 ratio of L/S.

MATLAB codes

1. Transform the SPC files into matrixes:

```
clear
clc
filename = 'Experiment 2016-05-21 12-33 K64';

d = tgspread([filename '.spc']);
wavelength = d.X';
spectra = d.Y';

save(filename, 'spectra', 'wavelength')
```

2. Preprocessing Savgol method:

```
function out = savgol(values, dorder, width, porder)
    out = zeros(size(values));

    for i = 1:size(values, 1)
        v = values(i, :);
        w = (width - 1)/2;
        f = pinv(pt(-w:w, 0:porder))';

        x = v;
        y = f(dorder + 1, end:-1:1);
        v = conv(x, y, 'full');
        out(i, :) = v((w + 1) : (numel(v) - w));
    end

    function t = pt(x, y)
        [xx, yy] = meshgrid(x, y');
        t = xx .^ yy;
    end
end

end
```

3. Preprocessing alsbasecorr method:

```
function pspectra = alsbasecorr(spectra, smoothness, penalty)
%ALSBASECORR fits baseline of a spectrum with asymmetric least squares
%
% Arguments:
% -----
% SPECTRA - a row-vector or a matrix with spectra
% SMOOTHNESS - smoothness parameter (default 10^3)
% PENALTY - penalty parameter (from 0 to 1, default 0.02)
%
% Returns:
% -----
% PSPECTRA - a row-vector or a matrix with corrected spectra
%
% Example:
% -----
% sp_new = alsbasecorr(sp, 1000, 0.2);
%
% References:
% -----
% [1] P. Eilers, H. Boelens, Baseline Correction with Asymmetric Least
Squares Smoothing, 2005
%

[nr, nc] = size(spectra);

if nargin < 3
    penalty = 0.02;
end

if nargin < 2
    smoothness = 10^3;
end

pspectra = zeros(size(spectra));
for i = 1:nr
    s = spectra(i, :)' ;
    m = length(s);

    D = diff(speye(m), 2);
    w = ones(m, 1);

    for it = 1:20
        W = spdiags(w, 0, m, m);
        C = chol(W + smoothness * D' * D);
        baseline = C \ (C' \ (w .* s));
        w = penalty * (s > baseline) + (1 - penalty) * (s < baseline);
    end

    pspectra(i, :) = s - baseline;
end
end
```

4. Generation of Raman spectra sample code:

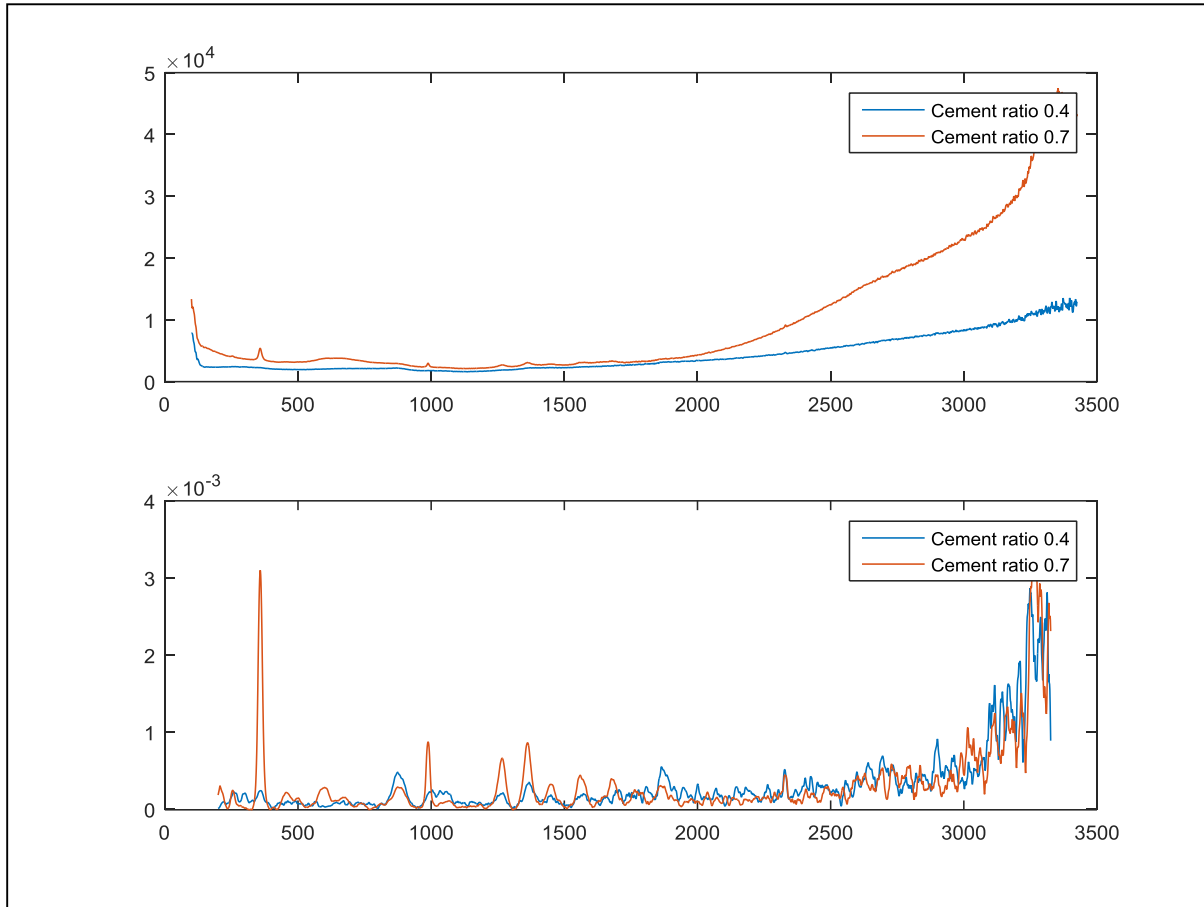


Figure 93 Cement samples with ratios 0.4 and 0.7 after 28 days of curing at room temperature

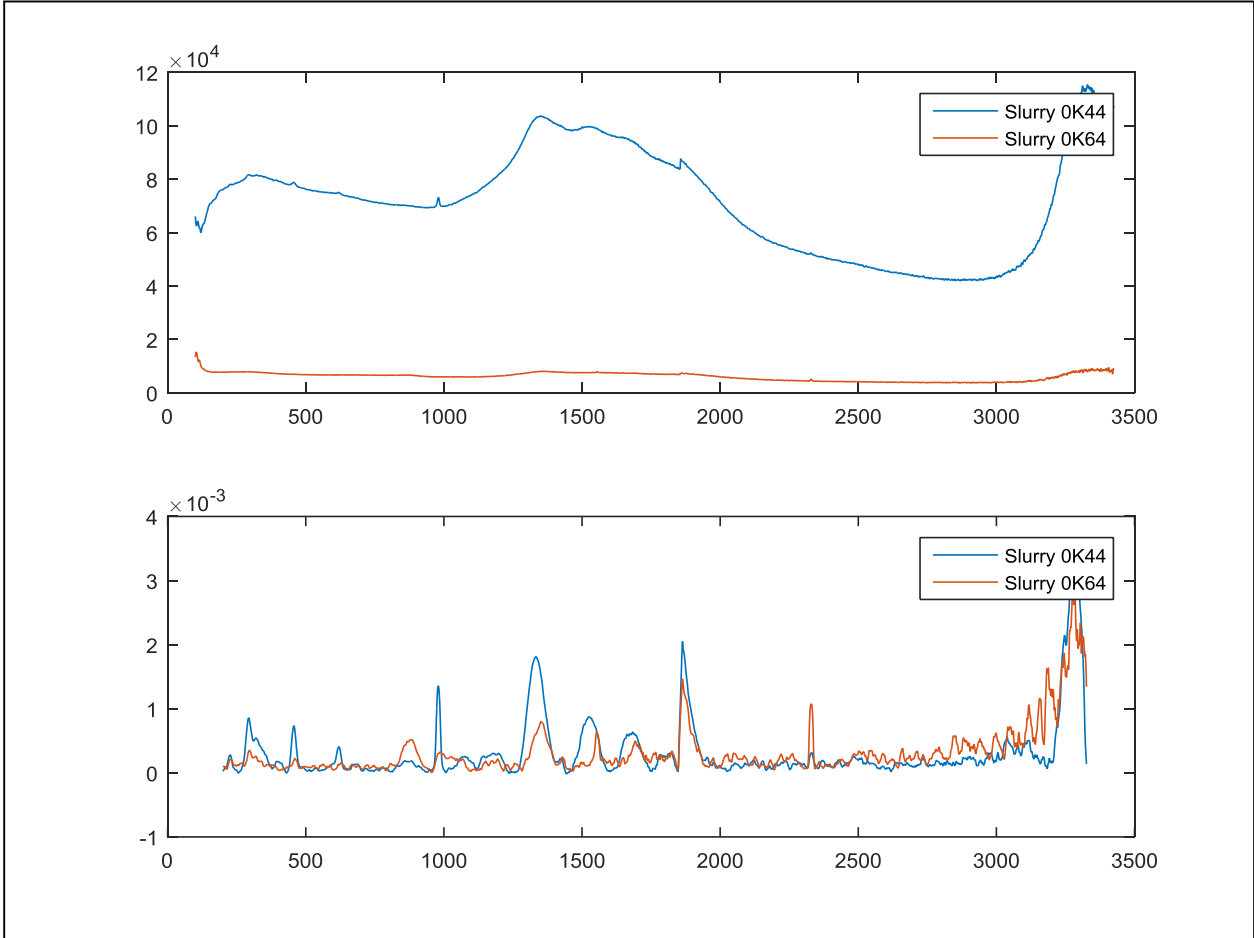
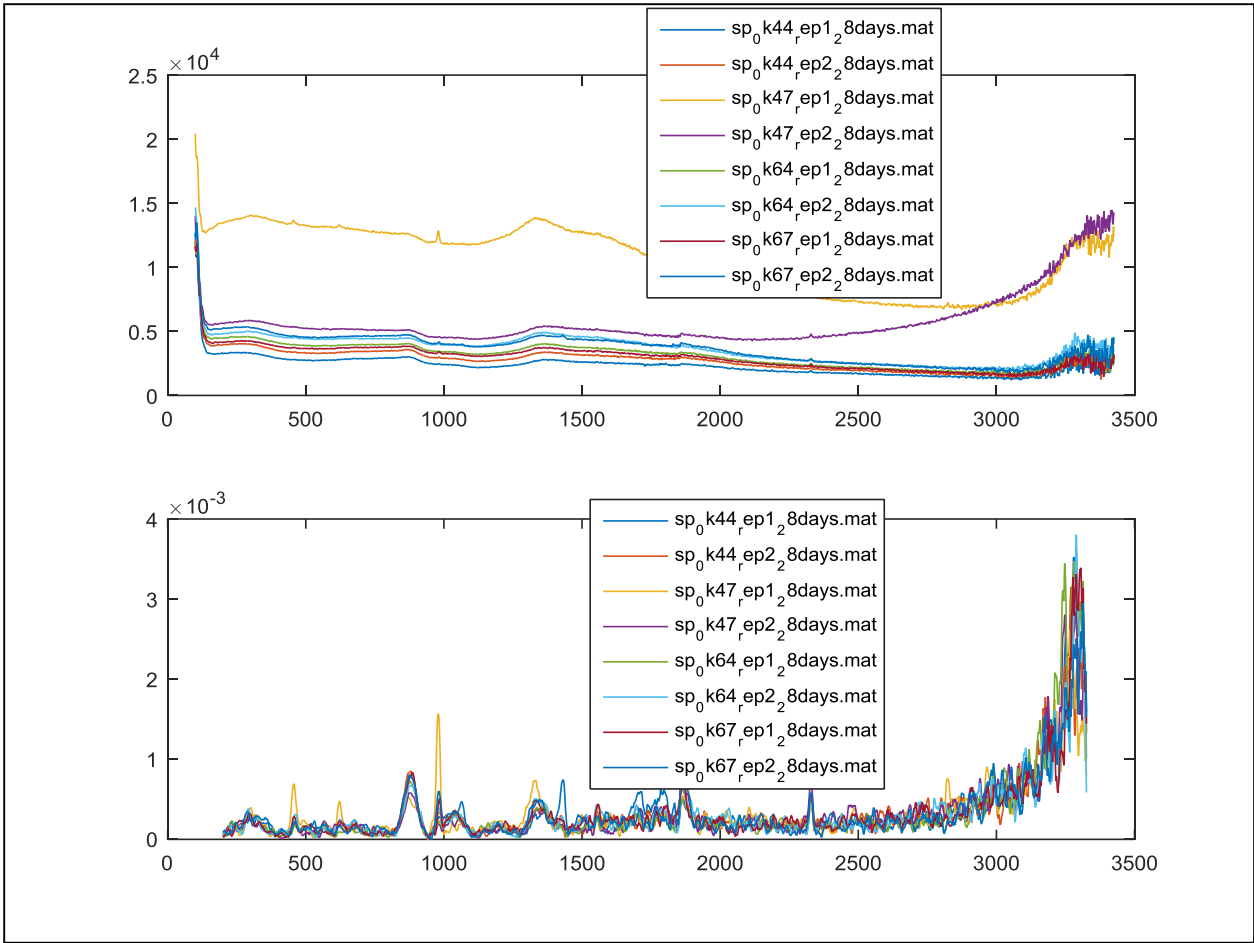


Figure 94. Spectra for slurry samples 0K44 and 0K64



Geopolymer samples created for the study in the reference [30]

Name	Sample code	Mixture components					Final values		
		BA (g)	MK (g)	Na silicate sol. (ml)	NaOH sol. (M) (ml)	S/L ratio (g/ml)	Si/Al (mol/mol)	NaOH (M)	
A	S-2.29-6	15.8	4.2	3	15	2	4	2.29	6
B	S-1.69-6	11.7	8.3	3	15	2	4	1.69	6
C	S-1.28-6	4.6	15.4	3.5	14.5	2.5	3.3	1.28	6
D	S-2.29-9	16.2	3.8	2	15	3	4	2.29	9
E	S-1.69-9	12.3	7.7	2	15	3	4	1.69	9
F	S-1.28-9	5.7	14.3	2.5	15.5	3.5	3.3	1.28	9
G	S-2.29-12	16.7	3.3	1	15	4	4	2.29	12
H	S-1.69-12	13	7	1	15	4	4	1.69	12
I	S-1.28-12	7.2	12.8	1	14.5	5	3.3	1.28	12
J	S-2.29-5	16	4	2.5	10	2.5	4	2.29	5
L	S-1.69-5	12	8	2.5	10	2.5	4	1.69	5
M	S-1.28-5	5.2	14.8	3	10	3	3.3	1.28	5
O	S-2.29-7.5	16	4	2.5	15	2.5	4	2.29	7.5
P	S-1.69-7.5	12	8	2.5	15	2.5	4	1.69	7.5
Q	S-1.28-7.5	5.2	14.8	3	15	3	3.3	1.28	7.5

Figure 95. Compositions of bottom ash based geopolymers with NaOH and sodium silicate as activators.

Thermal analysis results of fly ash melting experiment												
Experimental run no.	Ash no.	CaO addition (%)	Sample weight (mg)	Atmosphere	Heating rate (°C min ⁻¹)	Polymorphic transition			Fusion transition			Total heat required (kJ kg ⁻¹)
						Temperature range (°C)	Peak temperature (°C)	Latent heat (kJ kg ⁻¹)	Temperature range (°C)	Peak temperature (°C)	Latent heat (kJ kg ⁻¹)	
1	A	0	21.6	N ₂	10	498.8–602.4	581.3	21.86	1124.0–1184.9	1164.5	656.86	1800.55
2	A	0	17.2	N ₂	20	668.8–756.7	731.0	29.69	1130.6–1250.7	1169.8	667.13	1646.21
3	A	0	20.5	O ₂	5	–	–	–	1127.5–1175.5	1160.1	700.79	1437.90
4	A	0	22.0	O ₂	10	482.4–630.1	593.2	17.89	1130.0–1184.5	1168.4	638.28	1837.69
5	A	0	21.7	O ₂	20	492.5–589.4	548.2	25.44	1135.1–1200.4	1178.3	623.97	1794.01
6	A	10	19.3	O ₂	10	366.1–407.7	395.4	16.95	1167.6–1228.2	1205.4	422.55	1718.28
7	A	20	19.8	O ₂	10	365.5–416.1	399.8	45.03	1324.5–1402.9	1266.3	422.10	1439.67
8	B	0	16.4	N ₂	10	475.5–554.3	542.2	54.62	918.0–975.9	952.4	245.62	1398.15

Figure 96. Samples and experimental enthalpies for the reference [38]

Compressive strength plots

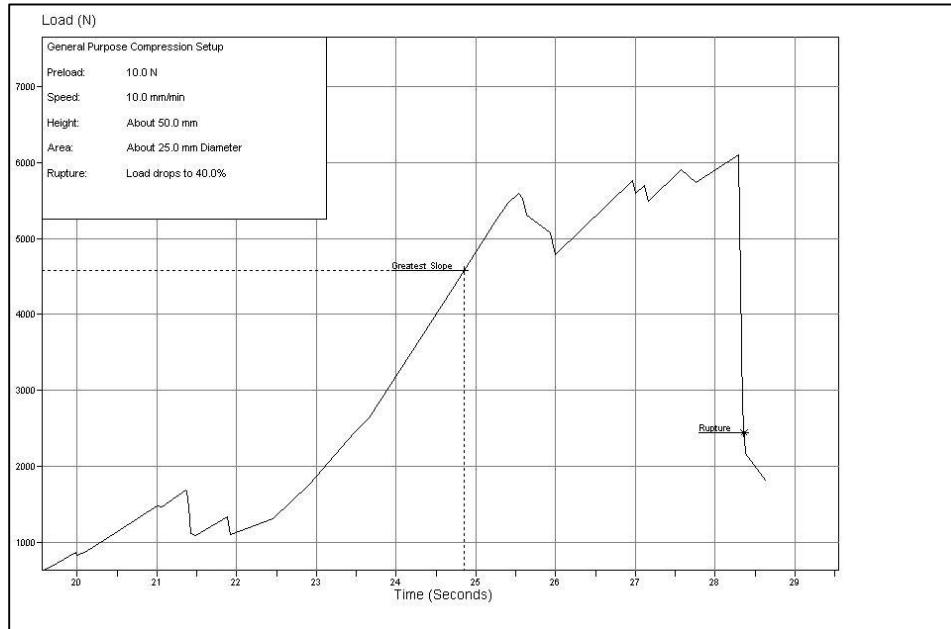


Figure 97. Compressive strength for K44

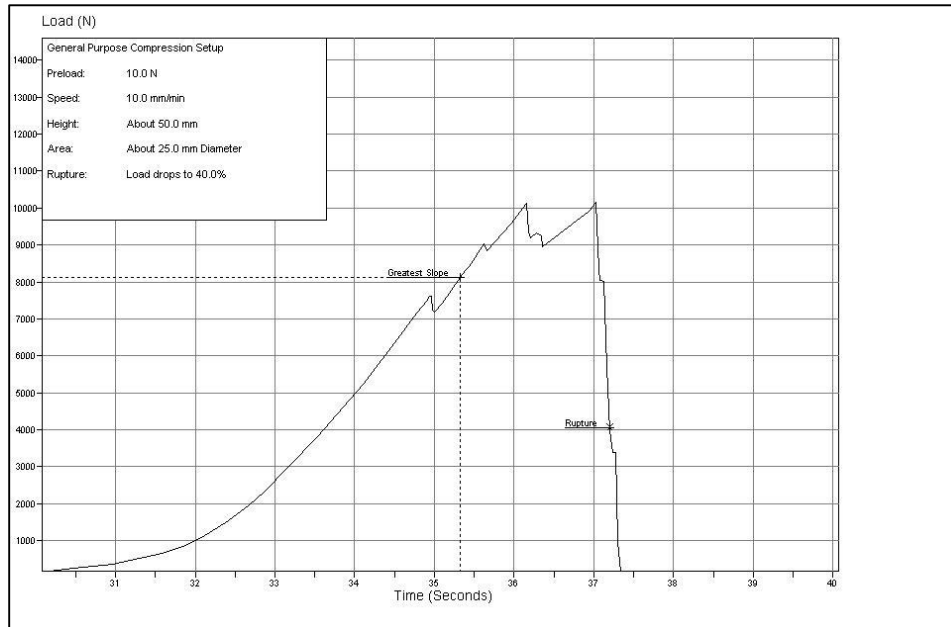


Figure 98. Compressive strength for K67

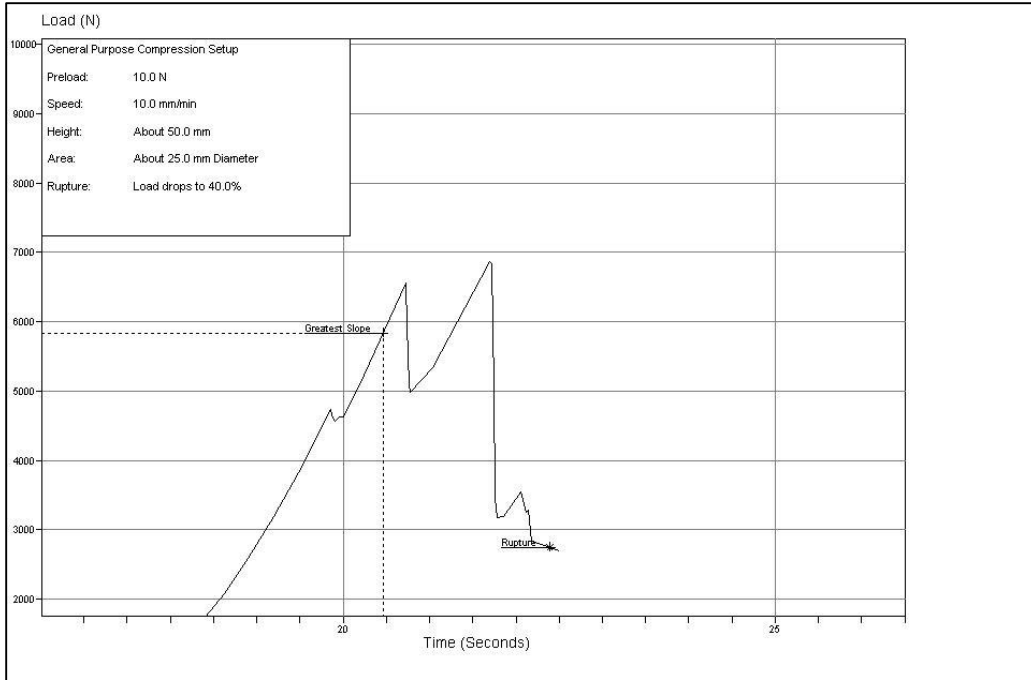


Figure 99. Compressive strength for K64

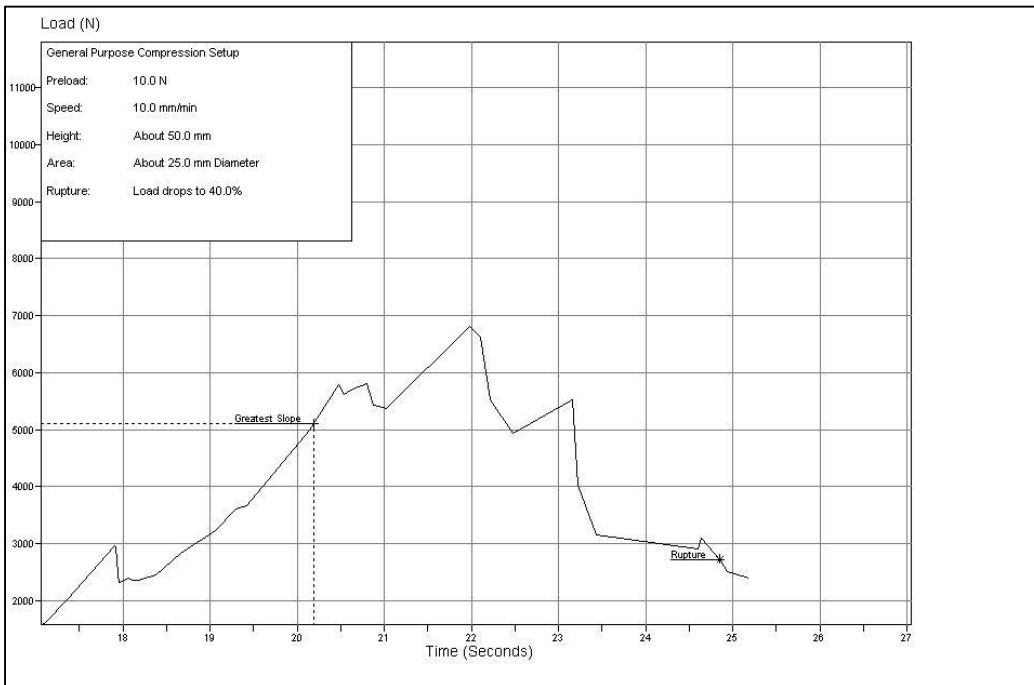


Figure 100. Compressive strength forment with ratio 0,7 and 4 M

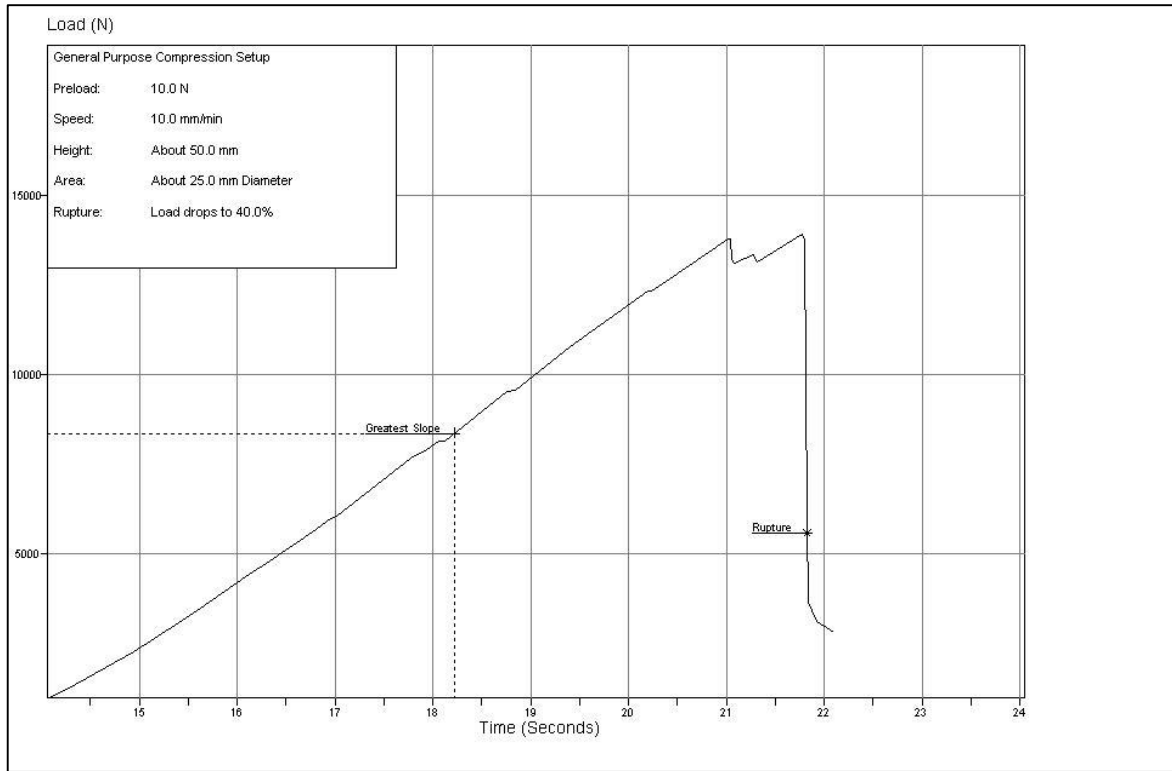


Figure 101. Compressive strength forcement with ratio 0,7 and 6 M